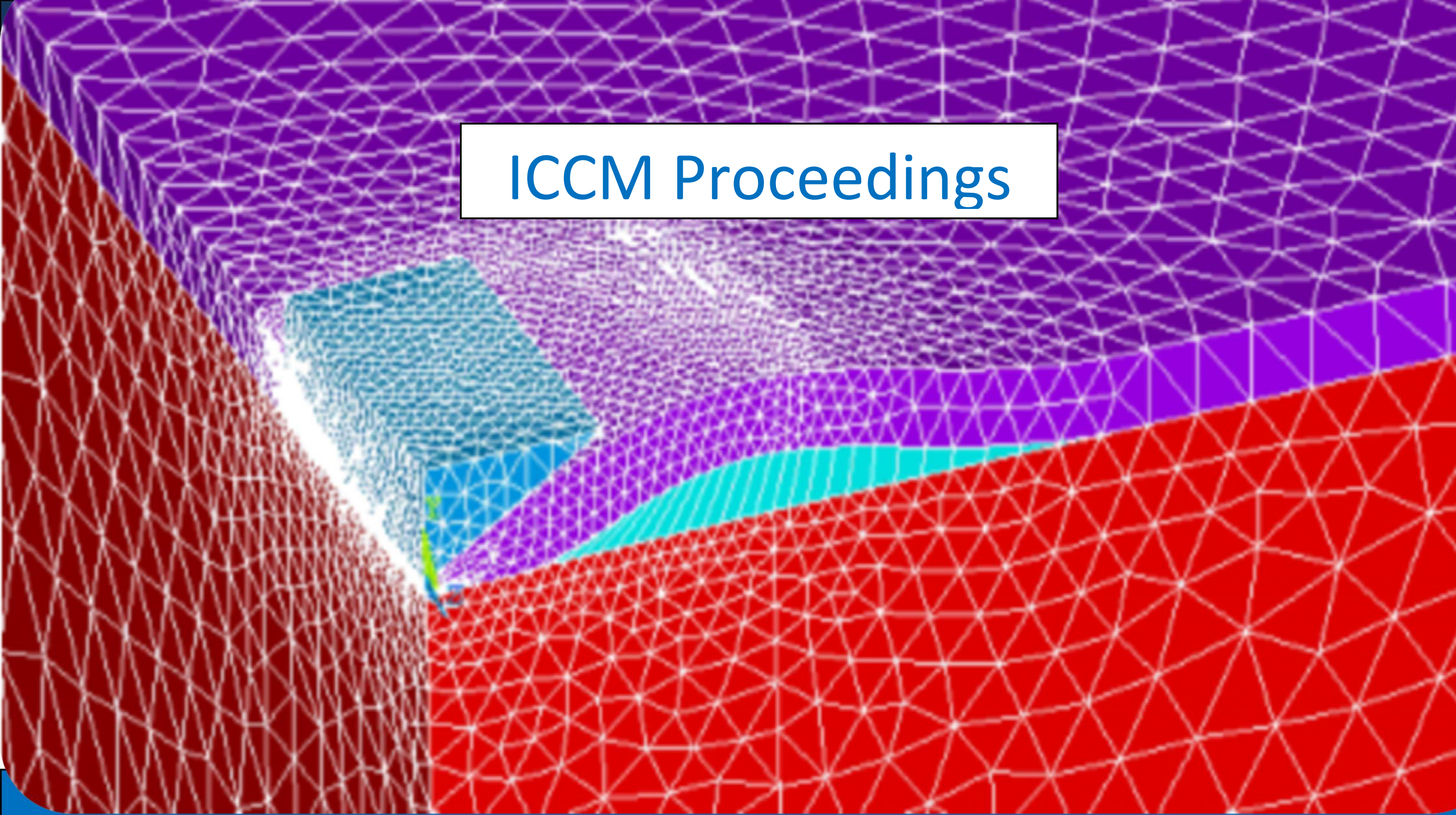

ICCM Proceedings

Proceedings of the International Conference on Computational Methods

(Vol. 13, 2026)

17th ICCM, 16th-19th August 2026

Editors: **Y. Cengiz Toklu, Guirong Liu**

ScienTech Publisher

ISSN 2374-3948 (online)

ICCM2026

Proceedings of the International Conference on
Computational Methods (Vol. 13, 2026)
17th ICCM, 16th-19th August 2026, Virtual Conference

Edited by
Guirong Liu
University of Cincinnati, USA

Yusuf Cengiz Toklu
Istanbul Aydin University, Türkiye

Proceedings of the International Conference on Computational Methods, Vol.13, 2026
This volume contains full papers accepted by the 17th ICCM, 16th-19th August, 2026.
First Edition, August 2026
International Standard Serial Number: ISSN 2374-3948 (online)
Papers in this Proceedings may be identically cited in the following manner: Author names, *Paper title, Proceedings at the 17th ICCM2026, 16th-19th August 2026, online*, Eds: Guirong Liu, Yusuf Cengiz Toklu, ScienTech Publisher.
Note: The papers/data included in this volume are directly from the authors. The editors are not responsible of the inaccuracy, error, etc. Please discuss with the authors directly, if you have any questions.
Published by
Scientech Publisher LLC, USA
https://www.sci-en-tech.com/

WELCOME MESSAGE

Dear Distinguished Guests, Speakers, and Participants,

On behalf of the Organizing Committee, it is my distinct honor and privilege to welcome you to the **17th International Conference on Computational Methods (ICCM2026)**, taking place online as a virtual conference from **August 16th to 19th, 2026**.

ICCM continues its proud tradition as a premier global forum for academics, researchers, and industry professionals to share cutting-edge research, numerical innovations, and practical applications across computational engineering and the sciences.

We had initially planned to gather in person in the magnificent city of Istanbul, hosted by our sponsor, **Istanbul Aydin University, Faculty of Engineering**. However, due to ongoing regional conflicts and unrest surrounding Türkiye, the committee decided to convert ICCM2026 into a fully virtual event. Although Türkiye itself remains entirely uninvolved in these surrounding conflicts, the broader geopolitical circumstances introduced significant travel challenges and safety considerations for our international attendees. Our top priority remains the convenience, safety, and inclusive participation of our global community.

While we are unable to meet physically in Istanbul this year, the virtual format allows us to connect seamlessly across time zones without geographical barriers. We are confident that this online gathering will foster the same spirit of rigorous scientific debate, knowledge exchange, and international collaboration that ICCM has championed for years.

We express our sincere gratitude to our sponsor, **Istanbul Aydin University, Faculty of Engineering**, for their steadfast support during this transition. Special recognition and heartfelt thanks go to our Honorary Chairman, Professor G.R. Liu (University of Cincinnati, USA), whose vision and guidance continue to inspire the ICCM community. We also thank all session chairs, reviewers, track organizers, and participants for their dedicated contributions and flexibility.

Over the coming days, I encourage you to actively engage in the technical sessions, join the digital Q&A discussions, and connect with colleagues old and new.

Thank you for your participation and support. I wish you all a successful, inspiring, and rewarding conference.

Professor Cengiz Toklu
Conference Chairman
Istanbul Aydin University
Türkiye

ORGANIZATION COMMITTEES

Conference Chairman
Cengiz Toklu, Istanbul Aydin University, Türkiye

Honorary Chairman
Guirong Liu, University of Cincinnati, United States

Local Committee
A. Metin Ger, Ph.D, Professor, Istanbul Aydin University, Co-Chair
Pınar Yildirim, Ph.D, Istanbul Aydin University
Beste Kocak Dinc, Ph.D, Istanbul Aydin University
Yusuf Kaya, Research Assistant, Beykent University

International Scientific Advisory Committee
Philipp Birken (Sweden)
Jeng-Tzong Chen (Taiwan)
Lei Chen (USA)
Shaohua Chen (China)
Zhen Chen (USA)
Fangsen Cui (Singapore)
Raj Das (Australia)
Xiangwei Dong (China)
Dianlei Feng (China)
Zhuojia Fu (China)
XiaoWei Gao (China)
Ahmet Metin Ger (Türkiye)
Hauke Gravenkamp (Germany)
Yuantong Gu (Australia)
Chenfeng Li (UK)
Eric Li (UK)
Hua Li (Singapore)
Wei Li (China)
Jabareen Mahmood (Israel)
Roberto Montemanni (Italy)
Sundararajan Natarajan (India)
Yufeng Nie (China)
Sinan Melih Nigdeli (Türkiye)
Hiroshi Okada (Japan)
Yuki Onishi (Japan)
Fatih Mehmet Özkal (Türkiye)
Takahiro Saitoh (Japan)
Luming Shen (Australia)
Yuichi Tadano (Japan)
Ken-ichi Tsubota (Japan)
Decheng Wan (China)
Lifeng Wang (China)
Wenquan Wang (China)
Yue-Sheng Wang (China)
Zhihai Xiang (China)
Judy Yang (Taiwan)
Hongling Ye (China)
Jingjie Yeo (USA)
Haifei Zhan (Australia)
Aman Zhang (China)
Chuanzeng Zhang (Germany)
Guiyong Zhang (China)
Lihai Zhang (Australia)
Xiong Zhang (China)
Zhe Zhang (China)
Kun Zhou (Singapore)
Zhuo Zhuang (China)

TABLE OF CONTENTS

A Unified Mobile System for AI-Assisted Vehicle Inspection Booking and Compliance Management in the UK

Thomas Pearson[1], and †*Sokyna Alqatawnah[1]

[1]Department of Science and Digital, School of Computing, Bradford College, UK.

*Presenting author: s.alqatawnah@bradfordcollege.ac.uk

†Corresponding author: s.alqatawnah@bradfordcollege.ac.uk

Abstract

Annual Ministry of Transport (MOT) inspections are a legal requirement for vehicles over three years old in the United Kingdom. Despite this, existing digital services supporting MOT compliance and booking remain fragmented, offering limited functionality in terms of comparison, personalisation, and user engagement. This paper presents MOT+, an Android-based mobile application designed to unify MOT booking, automated reminders, and garage comparison within a single platform. The system integrates AI-driven chatbot support, location-based garage search, real-time MOT reminders with calendar synchronisation, and gamification features aimed at improving user motivation and engagement.

A mixed-methods evaluation was conducted. Quantitative findings indicate high perceived usefulness of the chatbot (M = 4.2/5) and strong appreciation for automated MOT reminders (M = 4.5/5), while gamification demonstrated a moderate positive effect on booking motivation (M = 3.9/5). Qualitative feedback highlighted improved clarity of MOT-related information and reduced reliance on complex government websites.

The results align with the Technology Acceptance Model and Self-Determination Theory, suggesting that perceived ease of use, usefulness, and intrinsic motivation are key drivers of adoption in AI-enabled public service applications. This study contributes practical insights into the design of unified MOT platforms and extends existing work on chatbot integration and gamification in mobile public services.

Keywords: MOT booking, chatbot adoption, gamification, mobile applications, Technology Acceptance Model, user engagement.

Introduction

In the United Kingdom, vehicles over three years old are legally required to undergo an annual Ministry of Transport (MOT) inspection to ensure roadworthiness and environmental compliance [1]. Failure to maintain a valid MOT certificate can result in fines, penalty points, and invalid insurance. Despite the importance of compliance, existing digital services supporting MOT information and booking remain fragmented across government platforms and private providers.

The official GOV.UK MOT service provides authoritative information and reminder functionality; however, its information-dense presentation and formal structure may reduce accessibility for non-expert users. Prior research indicates that perceived ease of use plays a critical role in digital service adoption, particularly in regulatory contexts [2][3]. Commercial platforms such as Kwik Fit offer online booking capabilities but are restricted to affiliated garages, limiting user choice and price comparison [4].

Recent advances in mobile computing and artificial intelligence offer opportunities to improve compliance-related services through conversational interfaces, automation, and user-centred design. Studies have shown that AI-driven chatbots can enhance accessibility and reduce user effort in complex service environments [5][6]. Similarly, gamification techniques have demonstrated positive effects on motivation and recurrent usage in mobile applications [7][8].

This paper introduces MOT+, a unified mobile system designed to address usability, accessibility, and engagement gaps in existing MOT services. The contributions of this paper are threefold:

1. The design and implementation of a unified mobile system integrating MOT booking, reminders, and AI assistance.
2. The application of gamification and conversational AI within a vehicle compliance context.
3. An exploratory evaluation grounded in established technology acceptance and motivational theories.

Related Work

Government-led digital services prioritise accuracy and regulatory compliance; however, usability challenges are common due to complex navigation and formal presentation styles. Prior work highlights that such characteristics can negatively affect user engagement and adoption [2][3]. While GOV.UK provides reliable MOT data and reminders, its limited interactivity and lack of booking comparison reduce consumer choice [1]. Commercial services such as Kwik Fit improve convenience through online booking but restrict service options to internal networks [4].

AI chatbots are increasingly adopted in public-facing and regulated service domains. Research demonstrates that chatbots improve accessibility, reduce cognitive load, and enhance service understanding when aligned with authoritative data sources [5]. Trustworthiness and reliability are particularly important in public sector applications, where errors can have legal or safety implications [6].

Gamification strategies such as points, rewards, and progress indicators have been shown to positively influence user engagement and repeat usage across mobile platforms [7][8]. Self-Determination Theory explains these effects by emphasising autonomy, competence, and relatedness as drivers of intrinsic motivation [9].

Theoretical Framework

The Technology Acceptance Model (TAM) proposes that perceived usefulness and perceived ease of use are the primary determinants of technology adoption [2]. In MOT+, simplified navigation, booking automation, and chatbot guidance directly target these constructs.

The Unified Theory of Acceptance and Use of Technology (UTAUT) extends TAM by incorporating social influence and facilitating conditions as predictors of behavioural intention [3]. MOT+ addresses facilitating conditions through integrated reminders, garage comparison, and unified booking workflows.

Gamification features in MOT+ are grounded in Self-Determination Theory, which posits that sustained engagement emerges when systems support autonomy, competence, and relatedness [9]. Loyalty points and progress tracking in MOT+ aim to reinforce these motivational dimensions.

Methodology

A mixed-methods research design was employed to support both system development and evaluation. Mixed-methods approaches are particularly suitable for exploratory system studies where user perception and behavioural intent must be captured alongside functional performance.

Quantitative data were collected via structured questionnaires using five-point Likert scales to measure perceived usefulness, ease of use, and engagement in line with prior TAM-based studies [2]. Qualitative feedback was gathered through open-ended responses to capture user perceptions of clarity, usability, and trust, consistent with chatbot evaluation practices in complex service environments [5].

Ethical approval was obtained prior to data collection. All participant data were anonymised and handled in accordance with GDPR principles [1].

System Architecture and Design

This section describes the design and implementation of the MOT+ mobile system. Figure 1 illustrates the system architecture.

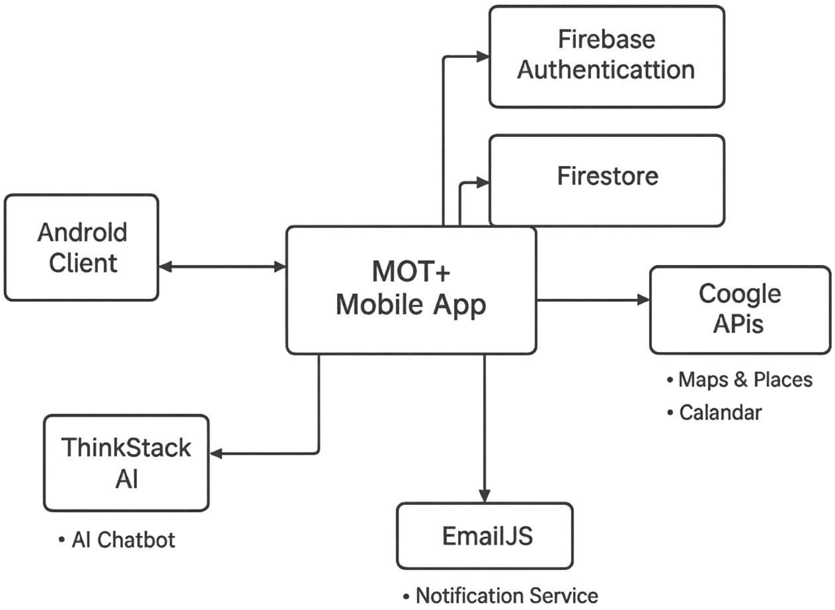

Figure 1. System architecture of the MOT+ mobile application

The Android client interacts with the core MOT+ mobile application, which orchestrates user authentication, booking management, and service integration. Firebase Authentication is used to manage secure user access, while Firestore stores user profiles, booking records, MOT dates, and gamification data. External services are integrated through APIs, including Google Maps and Places for location-based garage search, Google Calendar for automated MOT reminders, ThinkStack AI for chatbot functionality, and EmailJS for notification delivery. This modular architecture enables scalability while maintaining a clear separation between client-side logic, backend services, and third-party integrations.

Building on the architecture shown in Figure 1, MOT+ was developed as an Android application using Kotlin and Firebase services. Firebase Authentication and Firestore support secure user management and booking storage, while Google Maps and Places APIs enable location-based garage search and comparison [10]. Automated MOT reminders are integrated with Google Calendar to enhance compliance through timely notifications, reflecting prior findings on the effectiveness of real-time alerts [11][12]. EmailJS is used to deliver booking confirmations and alerts [13]. The AI chatbot is implemented using ThinkStack AI and embedded via WebView [14]. The chatbot is trained on certified government MOT data to ensure reliability and trustworthiness, aligning with best practices for public sector AI systems [9].

Results and Discussion

System-level testing confirmed that booking flows, authentication, garage search, and payment processes performed reliably under expected usage scenarios. In addition, user acceptance testing indicated strong satisfaction with chatbot clarity and reminder functionality.

Quantitative results demonstrate high perceived usefulness of the chatbot and reminder features, supporting TAM predictions that perceived ease of use and usefulness positively influence user acceptance [2]. The moderate impact of gamification on booking motivation aligns with prior findings suggesting that gamification enhances engagement but is most effective when combined with meaningful incentives [7][8]. Descriptive statistics (mean and standard deviation) indicated positive user perceptions across key dimensions, as summarised in Table 1. All evaluation measures were assessed using a five-point Likert scale (1 = strongly disagree, 5 = strongly agree).

Qualitative feedback indicates that users valued reduced reliance on complex government websites, consistent with research demonstrating the effectiveness of conversational interfaces in simplifying regulated services [5]. Trust and payment security concerns raised by participants further reinforce the importance of transparency and regulatory compliance in AI-enabled public systems [6]. Moreover, participants consistently reported that the interface was intuitive and easy to navigate, supporting the system's design emphasis on simplicity and perceived ease of use.

Table 1. Descriptive statistics for user evaluation measures.

Measure	Mean	SD
Chatbot improved understanding of MOT info	4.2	0.6
Chatbot was easy to use	4.0	0.8
Gamification increased motivation to book	3.9	0.7
MOT reminders were useful	4.5	0.5
Overall satisfaction with MOT+	4.3	0.6

While the proposed system is specific to the UK MOT context, the findings suggest that AI-assisted support, automated reminders, and gamification can be effective design strategies for improving user engagement in compliance-driven digital services.

Conclusion and Future Work

This paper presented MOT+, a unified mobile system designed to support AI-assisted vehicle inspection booking and compliance management in the UK. By integrating conversational AI, automated reminders, and gamification features, MOT+ addresses key usability and engagement gaps in existing MOT services. Evaluation results support established technology adoption and motivational theories, demonstrating the potential of user-centred AI design in regulatory and compliance-driven domains.

Future work will focus on cross-platform deployment, enhanced payment security through PCI-DSS-compliant solutions, longitudinal user studies to assess sustained engagement, and expanded chatbot functionality to support broader vehicle maintenance guidance.

References

[1] GOV.UK, 2025. Getting an MOT. Available at: https://www.gov.uk/getting-an-mot [Accessed 9 July 2025].

[2] Davis, F.D., 1989. Perceived usefulness, perceived ease of use, and user acceptance of information technology. MIS Quarterly, 13(3), pp.319–340.

[3] Venkatesh, V., Morris, M.G., Davis, G.B. and Davis, F.D., 2003. User acceptance of information technology: Toward a unified view. MIS Quarterly, 27(3), pp.425–478.

[4] Kwik Fit, 2025. Book your MOT test. Available at: https://www.kwik-fit.com/mot [Accessed 8 July 2025].

[5] Xu, L., Sanders, L., Li, K. and Chow, J.C., 2021. Chatbot for health care and oncology applications using artificial intelligence and machine learning: Systematic review. JMIR Cancer, 7(4), p.e27850. Available at: https://cancer.jmir.org/2021/4/e27850/.

[6] Wirtz, B.W., Weyerer, J.C. and Geyer, C., 2019. Artificial intelligence and the public sector—applications and challenges. International Journal of Public Administration, 42(7), pp.596–615.

[7] Hamari, J., Koivisto, J. and Sarsa, H., 2019. Does gamification work? – A literature review of empirical studies. International Journal of Human–Computer Studies, 107, pp.157–178.

[8] Cheng, V., Dunn, A., Eysenbach, G. and Torous, J., 2019. Gamification in apps and technologies for improving mental health and well-being: Systematic review. JMIR Mental Health, 6(6), p.e13717. Available at: https://mental.jmir.org/2019/6/e13717.

[9] Deci, E.L. and Ryan, R.M., 1985. Intrinsic Motivation and Self-Determination in Human Behavior. New York: Springer.

[10] Google Cloud, 2025. Maps and Places API. Available at: https://developers.google.com/maps.

[11] Subramaniam, S et al. (2007) Real time mailbox alert system via SMS or email. 2007 Asia-Pacific Conference on Applied Electromagnetics [Online]. Melaka, Malaysia. Available from: https://www.researchgate.net/publication/4364443_Real_time_mailbox_alert_system_via_SMS_or_email.

[12] Park, S. and Kim, J., 2020. Personalized mobile transport applications and their impact on user satisfaction. International Journal of Human–Computer Interaction, 36(4), pp.315–327.

[13] EmailJS, 2025. Send emails directly from JavaScript. Available at: https://www.emailjs.com .

[14] ThinkStack AI, 2025. Smart AI chatbot integrations. Available at: https://www.thinkstack.ai.

A comparison between FEM and FEMEM in solving structural problems

Yusuf Cengiz Toklu[1], and *Yusuf Kaya[2]

[1]Department of Civil Engineering, Istanbul Aydın University, Türkiye
[2] Department of Civil Engineering, Istanbul Beykent University, Türkiye
*Presenting and Corresponding author: yusufkaya@beykent.edu.tr

Abstract

While the conventional displacement-based Finite Element Method (FEM) is the cornerstone of structural analysis, it encounters fundamental mathematical limitations when dealing with unconstrained (free-free) or under-constrained systems. In such cases, even if the external loading is self-equilibrated and the total moment is zero, the global stiffness matrix ([K]) becomes singular. This singularity prevents the attainment of a unique displacement solution, as the system remains indeterminate due to undefined rigid body motions. Consequently, while internal forces may be computable, the absolute displacement field remains non-unique, requiring an additional selection criterion to identify a physically meaningful representative solution.

This study proposes the Finite Element Method with Energy Minimization (FEMEM) as a robust alternative to overcome these algebraic constraints. The primary argument of this paper is that FEMEM resolves the solution-space ambiguity inherent in classical FEM by employing an energy-based selection principle. Unlike the traditional approach, which yields a singular algebraic system, FEMEM formulates the problem as the minimization of the total potential energy functional (Π).

The findings demonstrate that FEMEM successfully identifies a stable and unique displacement solution without the need for artificial reference constraints. Furthermore, numerical applications reveal that FEMEM, through its inherent geometric nonlinearity, successfully captures non-unique equilibrium states and snap-through mechanisms (kinematic inversions) in unconstrained structures under severe loading—phenomena that classical linear FEM fails to detect. By navigating the energy landscape to select the most suitable global or local representative solution, FEMEM proves to be a superior framework for analyzing structures where conventional boundary conditions are absent or ill-defined, such as orbiting space trusses or floating structures. This work highlights the potential of energy-based methods to extend the boundaries of traditional computational mechanics.

Keywords: FEM, FEMEM, energy minimization, truss systems, singular stiffness matrix.

Introduction

The conventional displacement-based Finite Element Method (FEM) is one of the most widely used computational tools and constitutes a cornerstone of structural analysis [1][2]. However, the method encounters fundamental mathematical limitations when applied to unsupported (free-free) or insufficiently constrained systems, such as space trusses and floating structures. In such unconstrained systems, the global stiffness matrix, ([K]), becomes singular because of the presence of undefined rigid-body modes, even when the applied external loads are self-equilibrated and the resultant moment is zero [3].

This singularity renders the system mathematically indeterminate and prevents the determination of a unique displacement solution. Consequently, although the element internal forces of a free-free system may be determined using the conventional FEM formulation, the absolute displacement field remains non-unique. An additional selection criterion is therefore required to identify a physically meaningful representative solution from the admissible solution set [4].

In practice, this difficulty is commonly addressed by imposing artificial constraints on selected degrees of freedom (DOFs) or by employing mathematical techniques such as the Moore–Penrose pseudoinverse [5][6]. However, the resulting displacement solution becomes dependent on either the arbitrarily selected reference constraints or the imposed minimum-norm condition. Therefore, such solutions may be governed primarily by mathematical assumptions rather than by the inherent physical characteristics of the structural system.

This study proposes the Finite Element Method with Energy Minimization (FEMEM), presented in the literature as a current state-of-the-art methodology, as a robust alternative to overcome these algebraic constraints [7]. The central argument of this study is that FEMEM reformulates the structural problem as the minimization of the total potential energy functional, (Π), and resolves the inherent indeterminacy of the classical FEM solution space through an energy-based selection principle. Furthermore, energy-based optimization methods are highly effective in handling structural systems undergoing large deflections and can accurately compute non-unique equilibrium solutions, a domain where classical linear matrix formulations severely struggle [8]. Within this framework, the study investigates how FEMEM identifies an energetically optimal and stable representative solution without requiring artificial constraints. Its performance and resulting displacement solutions are comparatively evaluated against the limitations of the conventional FEM formulation and the outcomes obtained using the Moore–Penrose pseudoinverse approach.

Methodology

Classical FEM Formulation and the Singularity Problem

In conventional finite element analysis (FEM), the equilibrium equation for a linear elastic system is established using the formulation ($Ku = F$), which defines the relationship among the global stiffness matrix ($[K]$), the nodal displacement vector (u), and the external load vector (F) [1]. However, when no physical supports or boundary constraints are assigned to the structure, the classical static FEM formulation cannot be applied directly.

A two-dimensional (2D) unsupported truss structure possesses three rigid-body modes: translation in the (x)-direction, translation in the (y)-direction, and in-plane rotation. Because these degrees of freedom remain unconstrained, the global stiffness matrix ($[K]$) becomes singular. The singularity of the matrix, indicated by a zero determinant ($\det(K) = 0$), prevents the computation of its inverse (K^{-1}) and, consequently, precludes the determination of a unique solution to the equilibrium equation ($Ku = F$).

Practical Approaches for Unconstrained Systems

In the literature and engineering practice, two principal approaches have been adopted to overcome the singularity problem encountered in the analysis of unsupported structures:

Artificial Degree-of-Freedom (DOF) Constraint: To eliminate the rigid-body modes, three degrees of freedom (e.g., the (u_x) and (u_y) displacements of one node together with the (u_x) or (u_y) displacement of another node) are artificially constrained to zero. This procedure does not represent the introduction of physical supports; rather, it merely establishes a reference coordinate system for the numerical solution. Under this approach, the computed member deformations, internal forces, and stresses remain physically meaningful and accurate, whereas the nodal displacements are expressed only relative to the selected reference point.

Pseudo-Inverse (Minimum-Norm) Solution: A mathematically more appropriate approach for unsupported systems is to replace the inverse of the singular stiffness matrix with its Moore–Penrose generalized inverse (K^+) [5][6]. The displacement field is then obtained from the formulation ($u = K^+F$). This method automatically removes the rigid-body modes from the solution space and returns the minimum-norm representative solution, i.e., the displacement vector with the smallest Euclidean norm ($||u||$) among the infinitely many admissible solutions. Nevertheless, the resulting displacement field does not represent absolute physical displacements.

Finite Element Method with Energy Minimization (FEMEM)

To overcome the algebraic singularity limitations of the classical finite element method, this study proposes the Finite Element Method based on Energy Minimization (FEMEM). Rather than attempting to solve a singular algebraic system, FEMEM formulates the problem as the minimization of the total potential energy functional (Π) [9]. For a linear elastic structure, the total potential energy is defined in Eq. (1).

$$\Pi = \frac{1}{2}u^T K u - u^T F \tag{1}$$

where the first term on the right-hand side represents the internal strain energy stored in the system, while the second term denotes the potential of the work performed by the external forces. Classical FEM transforms the equilibrium equations established at the element level into global coordinates to form a matrix equation (assembly stage). In contrast, FEMEM adopts a fundamentally different computational strategy; instead of assembling a global stiffness matrix, it explicitly minimizes the potential energy stored in each finite element [7]. Thus, nodal displacements are obtained directly as the result of an optimization problem rather than the solution of an algebraic equation system.

Minimizing the Π functional allows the use of metaheuristic optimization algorithms in problems with singular stiffness matrices [7][10]. The Total Potential Optimization using Metaheuristic Algorithms (TPO/MA) approach inherently accounts for geometric nonlinearities, offering robust solutions for plane-stress/strain and truss systems without requiring complex modifications to the global stiffness matrix [11][12]. Thus, nodal displacements are obtained directly as the result of an optimization problem, successfully capturing global minimum energy states even in highly non-linear deformations. The fundamental theoretical and operational differences between classical FEM and FEMEM are summarized in Table 1.

Table 1. Comparison between FEM and FEMEM approaches [7]

Comparison Criterion	Classical FEM	FEMEM
Basic Principle	Based on differential equilibrium equations.	Based on the minimization of total potential energy.
Assembly Stage	Requires the assembly of the global stiffness matrix ([K]).	Does not require global matrix assembly; energies are directly summed.

Solution Methodology	Solution of algebraic equation systems (Ku = F).	Solution via metaheuristic (TPO/MA, etc.) optimization algorithms.
Unconstrained (Free) Systems	Matrix becomes singular; requires artificial constraints.	Operates stably; finds the minimum energy state naturally.
Boundary Conditions	Mandatory to prevent rigid body motions.	Provides high flexibility for missing or unconventional boundary conditions.

Consequently, a stable and unique representative solution is obtained without introducing any artificial reference constraints. Unlike the classical FEM, which requires an external intervention such as the artificial assignment of support conditions to eliminate rigid-body modes, FEMEM resolves the indeterminacy of the solution space solely through the natural principle of energy minimization.

Results and Discussion

Truss Model and Loading Conditions

A 2D truss system model with 8 nodes and 13 elements was used to examine the proposed approaches. The plan of the model is given in Fig. 1. For all members, the cross-sectional area was defined as A = 200 mm² and the modulus of elasticity as E = 200,000 N/mm² ((for the initial pseudo-inverse analysis). The structural geometry was configured with a span of 3000 mm along the x-axis and a height of 4000 mm along the y-axis, starting from the coordinate (0,0). A downward load of 2,000,000 N was applied at Node 2, while upward loads of 1,000,000 N were applied at Nodes 4 and 8. The resultant vertical force is zero (1,000,000 + 1,000,000 − 2,000,000 = 0); therefore, the system is in self-equilibrium (internal static equilibrium).

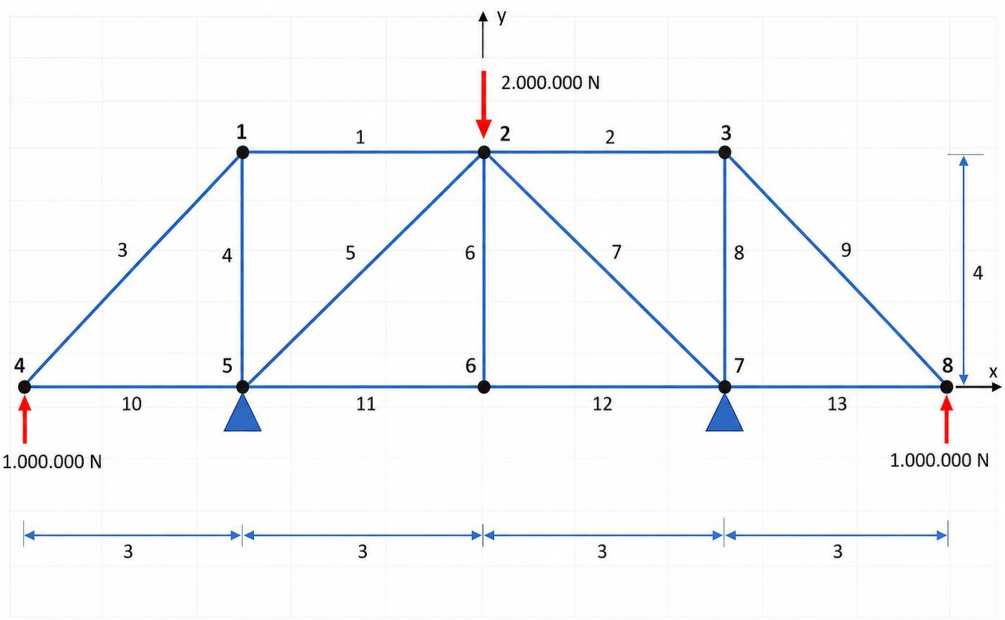

Figure 1. The examined case-the initial geometry and loading

Internal Forces, Stresses, and Member Elongations

The member internal forces, stresses, and axial deformations obtained from the pseudo-inverse solution of the unsupported truss system implemented in Python are fully consistent with the symmetric nature of the applied external loading.

Internal Forces and Stresses: The bottom chord members (11 and 12) experienced the largest tensile force (1,500,000 N, 7500 MPa). The top chord members (1 and 2) were subjected to compression (-750,000 N, -3750 MPa). Among the diagonal members, Members 3, 5, 7, and 9 carried compressive forces of (-1,250,000 N, -6250 MPa). The central vertical member (Member 6) acted as a zero-force member (0 N).

Axial Deformations: The greatest elongation was observed in Members 11 and 12 (112.50 mm), whereas the largest contraction occurred in Members 3, 5, 7, and 9 (-156.25 mm).

The internal forces, stresses, and axial deformations obtained using the pseudo-inverse algorithm accurately satisfy the structure's self-equilibrium condition ($\sum F = 0$) and therefore constitute unique, reliable, and physically meaningful engineering results.

Displacement Field and Solution Ambiguity

Because the displacement field cannot be obtained directly using classical FEM, the pseudo-inverse approach was employed, yielding maximum upward vertical displacements of 392.969 mm at Nodes 4 and 8, and maximum downward vertical displacements of -350.781 mm at Nodes 2 and 6. The deformed model is given in Fig 2.

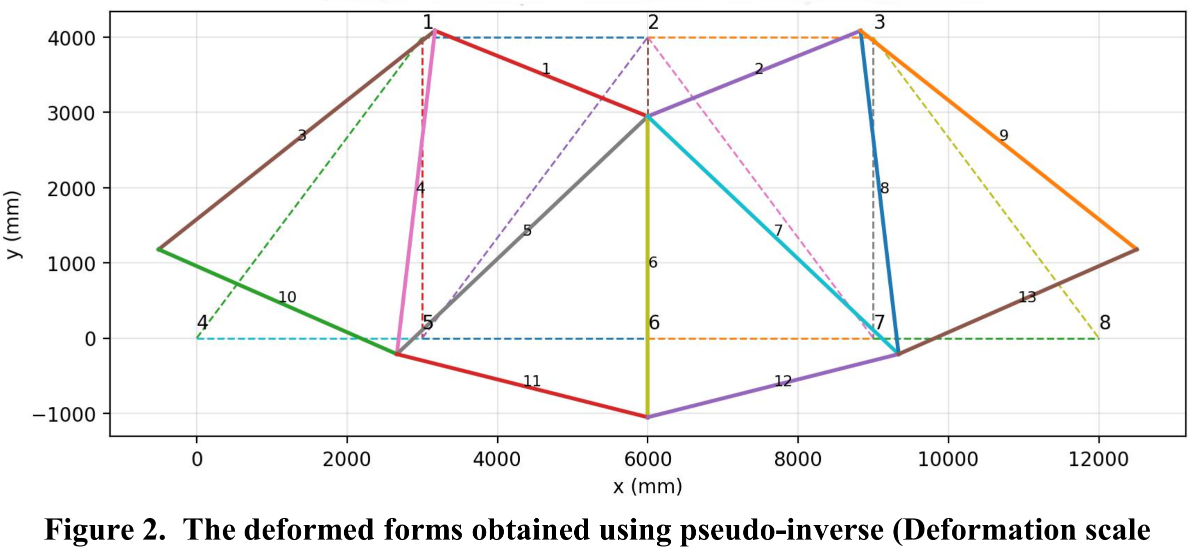

Figure 2. The deformed forms obtained using pseudo-inverse (Deformation scale coefficient = 3)

The pseudo-inverse method selects a specific representative displacement field by identifying the displacement vector with the minimum Euclidean norm. Consequently, the computed nodal displacements should not be interpreted as absolute physical displacements but rather as a mathematical reference solution.

FEMEM Solution: Geometric Nonlinearity and Multiple Equilibrium States

To demonstrate the advanced capabilities of FEMEM over linear matrix solutions, the same truss system was analyzed using the FEMEM algorithm. To observe the structural response under an even stiffer scenario, the Modulus of Elasticity was increased to E= 2,000,000 N/mm^2.

Classical FEM (and its pseudo-inverse derivative) inherently relies on the "small displacement theory," formulating the stiffness matrix based on the initial geometry. It, therefore, captures a local linear equilibrium state. FEMEM, conversely, computes the total potential energy based on the exact deformed nodal coordinates, inherently possessing geometric non-linearity (large displacement capability) [8][12].

Given the massive magnitude of the applied loads (2,000,000 N downwards, 1,000,000 N upwards) and the completely unconstrained (free-free) nature of the system in space, the metaheuristic optimization of FEMEM discovered a profoundly different global equilibrium state (Fig. 3).

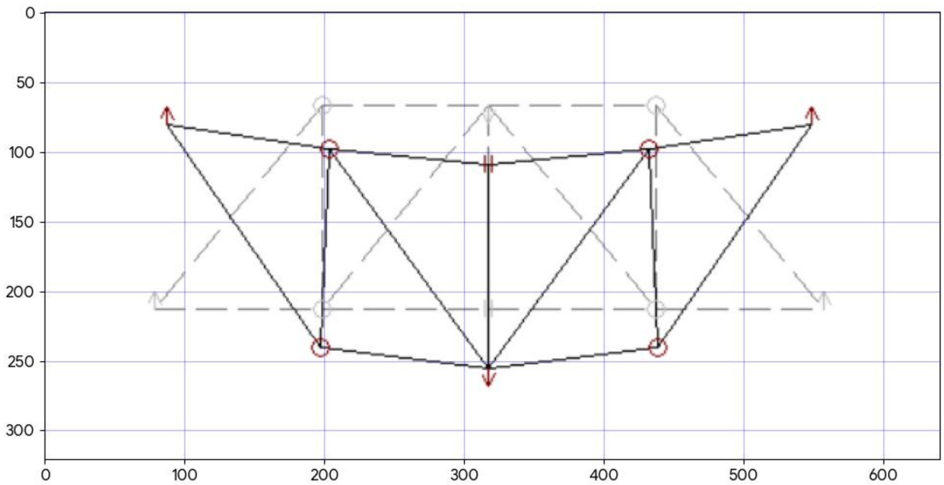

Figure 3. The exact kinematic inversion (snap-through) behavior captured by the FEMEM analysis

As seen in Fig. 3, rather than maintaining its original topology by excessively straining its elements, the unconstrained truss underwent a severe kinematic inversion, commonly known as a "snap-through" mechanism. The structure literally folded inside-out; Node 2 displaced massively in the downward direction, while Nodes 4 and 8 displaced heavily in the upward direction.

Mathematically, this extreme geometric deformation resulted in a total potential energy (Π = U - W) of approximately -16,755,791,485 N-mm. Although the internal strain energy (U) of the elements remains positive, the external loads performed an immense amount of positive work (W) because the nodes displaced extensively in the exact direction of the applied forces. The subtractive external work term (-W) vastly overpowered the strain energy, driving the functional into a deep global minimum. If physical boundary conditions (supports) were present, they would obstruct this inversion, and FEMEM would converge to the standard geometric shape. However, in a free-free space, FEMEM accurately highlights the physically most probable lowest-energy state (snap-through), proving that it can identify multiple and non-unique equilibrium configurations that linear classical FEM completely overlooks [8].

Conclusions

This study investigated the algebraic limitations encountered in the analysis of unsupported (free-free) structures and discussed the mechanism by which the Finite Element Method based on Energy Minimization (FEMEM) provides a stable and unique and geometrically non-linear solutions. Based on the theoretical and numerical investigations performed on the truss system, the following principal conclusions can be drawn:

Limitations of the Classical FEM: The conventional displacement-based finite element method cannot determine the displacement field directly for unsupported structures because the rigid-body modes render the global stiffness matrix singular. It also heavily relies on linear, small-displacement assumptions.

Limitations of Mathematical Filtering: The Moore-Penrose pseudo-inverse method produces accurate internal forces for a localized linear state. However, the resulting minimum-norm displacement field does not represent absolute physical displacements but a mathematically constrained reference.

Geometric Nonlinearity and Snap-Through Detection: FEMEM naturally resolves the indeterminacy of the displacement space. More importantly, as demonstrated by the numerical results, its optimization-based algorithm inherently accounts for large deflections. It successfully captures extreme kinematic inversions (snap-through behavior) and multiple equilibrium states driven by massive external work, leading to deep negative energy minimums ($\approx -16.7 \times 10^9$ N-mm) that linear algebraic formulations cannot detect.

In conclusion, for structures in which conventional boundary conditions are absent—such as orbiting space trusses—metaheuristic energy-based approaches like FEMEM provide a robust and physically consistent computational framework that vastly extends the boundaries of conventional computational mechanics.

References

[1] Bathe, K. J. (2006). *Finite element procedures*. Klaus-Jurgen Bathe.
[2] Zienkiewicz, O. C., & Taylor, R. L. (2005). *The finite element method set*. Elsevier.
[3] Felippa, C. A. (2004). *Introduction to finite element methods*. University of Colorado, 885.
[4] Pellegrino, S. (1993). Structural computations with the singular value decomposition of the equilibrium matrix. *International Journal of Solids and Structures*, 30(21), 3025-3035.
[5] Moore, E. H. (1920). On the reciprocal of the general algebraic matrix. Bulletin of the american mathematical society, 26, 294-295.
[6] Penrose, R. (1955, July). A generalized inverse for matrices. In Mathematical proceedings of the Cambridge philosophical society (Vol. 51, No. 3, pp. 406-413). Cambridge University Press.
[7] Toklu, Y. C., & Kaya, Y. (2026). Finite element method with energy minimization (FEMEM) in structural analysis: State-of-the-art. Challenge Journal of Structural Mechanics, 12(2), 145-161. doi:https://doi.org/10.20528/cjsmec.2026.02.007
[8] Toklu, Y. C., Temür, R., Bekdaş, G. (2015). Computation of nonunique solutions for trusses undergoing large deflections. International Journal of Computational Methods, 12(03), 1550022.
[9] Washizu, K. (1968). Variational methos in elasticity and plasticity. International Series of Monographs in Aeronautics and Astronautics.
[10] Toklu, Y.C., Bekdas, G., Nigdeli, S.M. (2021). Metaheuristics for structural design and analysis. John Wiley & Sons.

[11] Toklu, Y.C., Kayabekir, A.E., Bekdaş, G., Nigdeli, S.M., Yücel, M. (2020). Analysis of plane-stress systems via total potential optimization method considering nonlinear behavior. Journal of Structural Engineering, 146(11), 04020249.
[12] Toklu, Y.C., Bekdaş, G., Yücel, M., Nigdeli, S.M., Kayabekir, A.E., Kim, S., ... (2021). Total potential optimization using metaheuristic algorithms for solving nonlinear plane strain systems. Applied Sciences, 11(7), 3220.

A Meshless GFDM Approach for Incompressible Flow in an Eccentric Annulus

*Kutay Çelebioglu[1], and Metin Ger[2]

[1]Hydro Energy Research Center (ETU HYDRO), TOBB University of Economics and Technology, Ankara, Turkiye.
[2]Istanbul Aydın University, Istanbul, Turkiye.

*Presenting author: tkcelebioglu@etu.edu.tr
+Corresponding author: metinger@aydin.edu.tr

Abstract

In this study, the Generalized Finite Difference Method (GFDM), a meshless approach, is applied to incompressible viscous flow in an eccentric annulus using the vorticity–stream function formulation. The method is validated with the lid-driven cavity problem and then used to analyze flow between eccentric cylinders for Reynolds numbers between 250 and 1000 and eccentricity ratios up to 80%.

The results show that increasing Reynolds number and eccentricity significantly affect velocity distributions and streamline patterns, including the emergence of Taylor vortices. For the concentric case, numerical results agree well with the analytical solution, with an average deviation of about 5%. At high Reynolds numbers, convergence difficulties arise due to dominant convective effects.

The findings indicate that GFDM is an effective tool for modeling annular flows, although additional numerical treatments may be required for convection-dominated regimes.

Keywords: Eccentric annulus, generalized finite difference method, meshless methods, Taylor vortices

Introduction

Flows in annular geometries are encountered in a wide range of engineering applications, including drilling operations, journal bearings, rotating machinery, heat exchangers, and various process industries. In such systems, fluid motion occurs in the confined space between two cylindrical surfaces, and the prediction of flow behavior is essential for evaluating hydrodynamic forces, torque, and transport characteristics. In particular, annular flows play a critical role in situations where the relative motion between the inner and outer boundaries significantly influences system performance.

A special class of these flows arises when the axes of the inner and outer cylinders are not aligned, forming an eccentric annulus. In practical systems, eccentricity may result from manufacturing tolerances, mechanical deformations, or operational conditions such as vibrations and thermal stresses. The presence of eccentricity introduces strong asymmetry into the flow domain, leading to complex velocity distributions and flow structures that differ significantly from the concentric case. In addition, the combined effects of rotation and eccentricity may give rise to flow instabilities such as Taylor vortices, particularly at higher Reynolds numbers.

The analysis of flow in eccentric annuli is therefore of considerable importance for both design and performance assessment. However, the governing Navier–Stokes equations for such configurations are generally not amenable to analytical solutions, except for simplified cases such as concentric geometries. As a result, numerical methods are required to obtain accurate predictions of the flow field. Classical numerical approaches, including finite difference, finite volume, and finite element methods, have been widely used for this purpose. Nevertheless, these methods often rely on structured or body-fitted meshes, which may become difficult to generate and maintain for geometries involving strong irregularities or large eccentricities.

In recent years, meshless methods have emerged as a promising alternative for solving fluid flow problems. These approaches eliminate the need for predefined mesh connectivity and instead approximate the governing equations directly using scattered nodes. Among them, the Generalized Finite Difference Method (GFDM) offers a flexible framework for discretizing partial differential equations while maintaining high-order accuracy. Its ability to handle complex geometries with relative ease makes it particularly attractive for problems involving eccentric configurations.

In this study, the GFDM is applied to the analysis of incompressible viscous flow in an eccentric annulus. The governing equations are formulated using the vorticity–stream function approach, which removes the pressure variable from the system and automatically satisfies the continuity equation. The proposed formulation is first validated using a benchmark cavity flow problem and subsequently employed to investigate the effects of Reynolds number and eccentricity on the flow characteristics [1]. The results are analyzed in terms of velocity fields and streamline patterns, with particular attention to the development of asymmetric flow structures and vortex formation.

A substantial body of work has been devoted to understanding flow behavior in eccentric annuli, both analytically and experimentally. Early analytical studies provided exact solutions for fully developed laminar flow, offering fundamental insight into velocity distributions and wall shear stresses [2]. Experimental investigations further examined turbulent flow characteristics, including pressure drop, friction factors, and velocity distributions, highlighting the strong influence of eccentricity on flow asymmetry [3][4]. Later studies focused on flow stability and bifurcation, showing the transition from Couette flow to more complex regimes involving Taylor vortices as Reynolds number and eccentricity increase [5]. Additional experimental and numerical works further emphasized the role of eccentricity and rotational effects in modifying flow regimes and stability characteristics [6][7].

From a numerical perspective, a wide range of methods have been applied to annular flow problems. Classical techniques such as finite difference and finite volume methods have been successfully used in various configurations [8][9], but their reliance on structured or body-fitted meshes limits their flexibility in highly eccentric geometries. More advanced simulations have demonstrated improved accuracy but at a significant computational cost [10]. In recent years, meshless methods have emerged as an attractive alternative due to their ability to handle complex geometries without mesh generation. In particular, the Generalized Finite Difference Method (GFDM) has gained attention following foundational works on derivative approximations based on Taylor series expansions and weighted least squares formulations [11][12]. Subsequent studies demonstrated that GFDM can achieve high accuracy and efficiency, often outperforming other meshless approaches, especially in problems involving irregular node distributions and higher-order derivatives [13][14]. These developments highlight the potential of GFDM as a robust and flexible tool for solving complex fluid flow problems in eccentric geometries.

Methodology

Generalized Finite Difference Method

The Navier-Stokes equations governing the flow field include both convective and diffusive terms for velocity, along with a pressure term. The absence of a pressure term in the continuity equation introduces a constraint that couples the momentum and continuity equations. Classical mesh-based approaches, such as the finite volume method (FVM) and finite element method (FEM), are well established in computational fluid dynamics (CFD). However, their application to irregular geometries-such as the eccentric annular domain considered in this study-can be challenging due to mesh generation and grid quality requirements.

To address these limitations, a meshless approach based on the Generalized Finite Difference Method (GFDM) is employed. The GFDM eliminates the need for mesh connectivity and instead relies on local Taylor series expansions combined with a weighted least-squares minimization of the truncation error [15][16]. This formulation allows spatial derivatives to be approximated directly from scattered nodes.

Consider an arbitrary point $P(x_0, y_0)$ and a cloud of n neighbouring nodes, as illustrated in Fig. 1. A second-order Taylor series expansion of a scalar function f at a neighbouring node (x_i, y_i) about point P can be written as Eq. (1).

$$f_i(x+h_i, y+k_i) = f_0 + h_i\frac{\partial f_0}{\partial x} + k_i\frac{\partial f_0}{\partial y} + \frac{h_i^2}{2}\frac{\partial^2 f_0}{\partial x^2} + \frac{k_i^2}{2}\frac{\partial^2 f_0}{\partial y^2} + h_i k_i\frac{\partial^2 f_0}{\partial x \partial y} + o(\rho^3) \quad (1)$$

Where $h_i = x_i - x_0$ and $k_i = y_i - y_0$ represent the relative coordinates of the i^{th} node represent the relative coordinates of the P. Neglecting higher-order terms and applying this expansion to all neighbouring nodes yields a system of algebraic relations. Summation of these expressions leads to a compact form that is used to construct the error norm to be minimized.

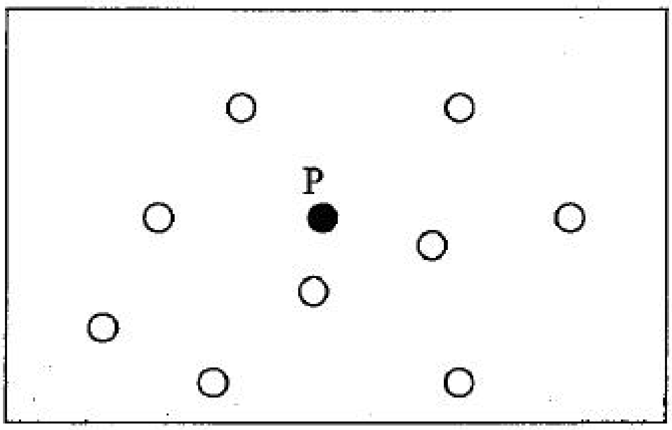

Figure 1. A set of points neighboring point P

To determine the unknown derivatives at point P, a weighted least-squares approach is adopted. The error norm is defined as Eq. (2).

$$B = \sum_{i=1}^{n} \left[\left[f_0 - f_i + h_i \frac{\partial f_0}{\partial x} + k_i \frac{\partial f_0}{\partial y} + \frac{h_i^2}{2}\frac{\partial^2 f_0}{\partial x^2} + \frac{k_i^2}{2}\frac{\partial^2 f_0}{\partial y^2} + h_i k_i \frac{\partial^2 f_0}{\partial x \partial y} + o(\rho^3)\right] w_i\right]^2 \quad (2)$$

where w_i is a weighting function associated with each node. In this study, a distance-based weighting function of the form $w_i = 1/d_i^3$ is used, where d_i is the Euclidean distance between node i and point P. This choice ensures that nodes closer to P have a stronger influence on the approximation, improving local accuracy and numerical stability.

The derivatives at point P, namely $\frac{\partial f}{\partial x}, \frac{\partial f}{\partial y}, \frac{\partial^2 f}{\partial x^2}, \frac{\partial^2 f}{\partial y^2}$ *and* $\frac{\partial^2 f}{\partial x \partial y}$ are obtained by minimizing the error norm B. This results in a system of five linear equations corresponding to the five unknown derivatives.

The resulting system can be expressed in matrix form as Eq. 3

$$A \cdot Df = F \quad (3)$$

where the matrix A is constructed from weighted sums of the relative coordinates of the neighbouring nodes, and therefore depends solely on the node distribution and weighting function. The vector Df contains the unknown derivatives at point P, and the vector F is formed from the function values at the neighbouring nodes.

By rearranging the system, the derivatives can be expressed explicitly in terms of the nodal function values (Eq. 4).

$$Df = A^{-1} \cdot G \cdot f = C \cdot f \quad (4)$$

where C is referred to as the coefficient (or star) matrix. Each row of matrix C provides the coefficients required to approximate a specific derivative as a linear combination of the function values at the surrounding nodes.

These derivative expressions are then used to discretize the governing equations over the entire computational domain. In this way, the partial differential equations are transformed into a system of algebraic equations defined at the nodal points.

Advantages of the Method

The GFDM provides several advantages for the analysis of flow in eccentric annular geometries. Since the method is meshless, it naturally accommodates irregular node distributions, which is particularly beneficial for non-concentric cylindrical domains. The formulation is local, meaning that derivatives at each node are computed using only neighbouring nodes, resulting in a straightforward and flexible implementation. Furthermore, the method allows for easy insertion of additional nodes without requiring re-meshing, enabling adaptive refinement in regions of interest. Boundary conditions can be incorporated directly at boundary nodes, and the method is capable of producing stable and accurate solutions even for highly distorted node configurations.

Computational Framework and Node Distribution

The numerical solution procedure is implemented through a dedicated computational program consisting of a main solver and auxiliary subroutines. The main program is responsible for solving the governing equations iteratively, while the subroutines construct the spatial derivative operators based on the Generalized Finite Difference Method (GFDM) and assemble the resulting algebraic system.

The computational domain, corresponding to the eccentric annular geometry, is discretized using a structured distribution of nodes without employing any mesh connectivity. The node distribution is generated by placing nodes along concentric circles of varying radii, with their centers offset according to the prescribed eccentricity. Nodes along each circular layer are distributed at constant angular increments. An example of the resulting node arrangement for an eccentricity of 60% is illustrated in Fig. 2.

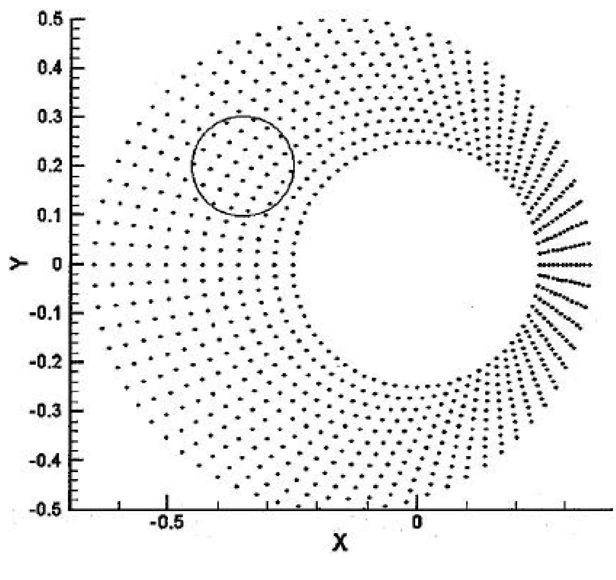

Figure 2. The node structure built for 60% eccentricity

The node set used in this study consists of 864 nodes, with 12 nodes aligned in the radial direction. The angular spacing between nodes is 5°, ensuring sufficient resolution of the flow field. The eccentricity is introduced by shifting the center of the inner cylinder relative to the outer cylinder, resulting in a non-uniform node distribution that accurately represents the geometric asymmetry.

For each node P, the spatial derivatives required in the governing equations are computed using a local cloud of neighboring nodes. The selection of these neighboring nodes plays a crucial role in the accuracy and stability of the GFDM approximation.

A structured selection strategy is adopted, as shown in Fig. 3, where nodes surrounding point P are chosen within a predefined influence region. Since five derivative components are to be determined (i.e., first-order derivatives in x and y, and second-order derivatives $\partial^2/\partial x^2$, $\partial^2/\partial y^2$, and $\partial^2/\partial x \partial y$), at least five neighboring nodes are required. In this study, a total of 12 neighboring nodes are used to enhance robustness and minimize numerical error.

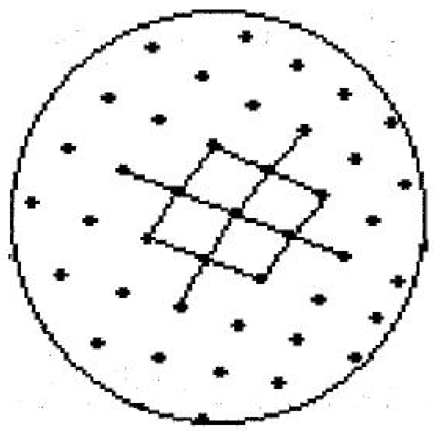

Figure 3. The selection of nodes

The derivatives at each node are obtained by minimizing the weighted residual defined in Eq. 2, leading to a linear system expressed in Eq. 3. The system is then inverted to compute the coefficient matrix C, as given in Eq. 4, which directly relates the derivatives at node P to the function values at surrounding nodes.

These coefficient matrices are computed locally for each node and stored in a global matrix structure, allowing efficient reuse during the iterative solution process.

Governing Equations: Vorticity–Stream Function Formulation

The flow is modeled using the two-dimensional incompressible Navier–Stokes equations, reformulated in terms of vorticity (ζ) and stream function (ψ). This formulation eliminates the pressure variable, thereby avoiding the need for pressure–velocity coupling schemes such as SIMPLE. The vorticity transport equation is given in Eq.5.

$$\frac{\partial \zeta}{\partial t} + u\frac{\partial \zeta}{\partial x} + v\frac{\partial \zeta}{\partial y} = \nu\left(\frac{\partial^2 \zeta}{\partial x^2} + \frac{\partial^2 \zeta}{\partial y^2}\right) \tag{5}$$

where u and v are velocity components, and ν is the kinematic viscosity.

The vorticity is defined in Eq. 6.

$$\zeta = \frac{\partial v}{\partial x} - \frac{\partial u}{\partial y} \tag{6}$$

Velocity components are obtained from the stream function (Eq. 7).

$$u = \frac{\partial \psi}{\partial y}, v = -\frac{\partial \psi}{\partial x} \tag{7}$$

Substituting these relations into the vorticity definition yields the Poisson equation for the stream function (Eq. 8).

$$\frac{\partial^2 \psi}{\partial x^2} + \frac{\partial^2 \psi}{\partial y^2} = -\zeta \tag{8}$$

Temporal and Spatial Discretization

The vorticity transport equation is solved using a fully implicit time integration scheme. The temporal derivative is approximated using a first-order forward difference (Eq. 9).

$$\frac{\partial \zeta}{\partial t} = \frac{\zeta^{k+1} - \zeta}{\Delta t} \tag{9}$$

All spatial derivatives at time level $k+1$ are computed using GFDM through the coefficient matrices C. For example, the first derivative in the x-direction is expressed in Eq. 10.

$$\frac{\partial \zeta}{\partial x} = \sum_{i=1}^{n} C_{1,i}\zeta_i \tag{10}$$

Substituting these expressions into the vorticity transport equation results in the discretized equation at node P (Eq. 11).

$$\frac{\zeta_P^{k+1} - \zeta_P^k}{\Delta t} + u^* \sum C_{1,i}\zeta_i + v^* \sum C_{2,i}\zeta_i = \nu\left(\sum C_{3,i}\zeta_i + \sum C_{4,i}\zeta_i\right) \tag{11}$$

where u^* and v^* denote lagged velocities used to linearize the convective terms.

Boundary Conditions and Solution Strategy

Boundary conditions are applied based on physical constraints of the problem. The outer cylinder is treated as a solid wall with a constant stream function value, typically set to zero. The inner boundary is also a solid wall, but its stream function value is related to the flow rate between the boundaries (Eq. 12).

$$\psi_{inner} - \psi_{outer} = \Delta q \tag{12}$$

The resulting algebraic system is written in matrix form as Eq. 13.

$$\tilde{A} \cdot \tilde{\zeta} = \tilde{L} \tag{13}$$

This system is solved using an LU decomposition-based solver with iterative refinement to ensure numerical stability and accuracy.

Iterative Solution Procedure and Stability Considerations

The solution procedure is iterative in time, advancing until a steady-state solution is achieved. At each iteration:

1. Vorticity is updated using Eq. 11
2. Stream function is computed by solving the Poisson equation
3. Velocity components are updated from Eq. 7
4. Boundary conditions are recalculated

The time step size Δt is selected based on stability considerations. The Courant–Friedrichs–Lewy (CFL) condition is used as a guideline (Eq. 14).

$$c_r = \frac{u\Delta t}{\Delta x} \leq 1 \tag{14}$$

Although the implicit scheme is theoretically unconditionally stable, excessively large time steps may lead to divergence due to nonlinear coupling and boundary condition sensitivity. Therefore, appropriate time step values are chosen to ensure convergence for all eccentricity and Reynolds number cases.

Boundary Conditions and Case Selection

The computational domain consists of two cylindrical boundaries forming an eccentric annulus. The outer cylinder is stationary, whereas the inner cylinder rotates with the prescribed angular velocity ω_1. The angular velocity of the outer cylinder is taken as zero, $\omega_2 = 0$, corresponding to a fixed outer wall. No-slip boundary conditions are imposed on both solid boundaries.

In the vorticity–stream function formulation, the velocity components are expressed in terms of the stream function as given in Eq. 7. Since a solid wall is itself a streamline, a constant stream function value is assigned along each wall. The stream function at the outer boundary is set to zero, while the value at the inner boundary is related to the flow rate between the two streamlines, as expressed in Eq. 12. This treatment is illustrated schematically in Fig. 4.

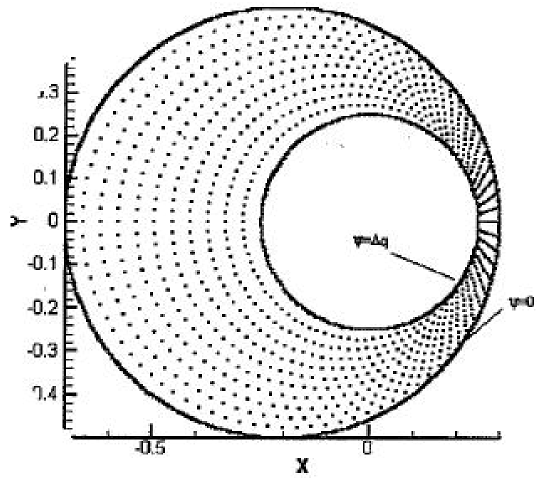

Figure 4. Boundary conditions for streamlines

The wall vorticity is evaluated using the definition of vorticity given in Eq. 6. For curved wall boundaries, no term is neglected; therefore, the boundary vorticity is calculated from the velocity gradients. These boundary values are updated during the iterative solution procedure together with the velocity field.

The geometric parameters are kept constant in all case studies, with the outer and inner cylinder radii taken as $R_{outer} = 0.5$ m and $R_{inner} = 0.25$ m, respectively. The eccentricity ratio is varied between 0% and 80%, corresponding to eccentricity values from 0 to 0.20 m. The working fluid is modelled with water-like properties, $with\ \mu = 1.0 \times 10^{-3}\ N{\cdot}s\ /\ m^2$, $\nu = 1.0 \times 10^{-6}\ m^2/s, and\ \rho = 999\ kg/m^3$.

The Reynolds number is defined using Eq. 15.

$$Re = \frac{V \cdot D}{\nu} \tag{15}$$

For the present two-dimensional rotational flow, the representative Reynolds number is expressed in terms of the angular velocity of the inner cylinder as given in Eq. 16. Three Reynolds numbers, namely 250, 750, and 1000, and three eccentricity ratios, namely 0%, 40%, and 80%, are resulting in 9 computational cases (Table 1).

$$Re = \frac{\omega \cdot R_{inner}^2}{\nu} \tag{16}$$

Table 1. Case studies

Re \ Ecc	0	40%	80%
250	Case 1	Case 2	Case 3
750	Case 4	Case 5	Case 6

1000	Case 7	Case 8	Case 9

This selection allows the comparison of both Reynolds number effects and eccentricity effects without overloading the results section with repetitive figures.

Results and Discussion

A total of nine simulations were performed to investigate the effects of Reynolds number and eccentricity on the flow within an eccentric annulus (Figs. 5-7).

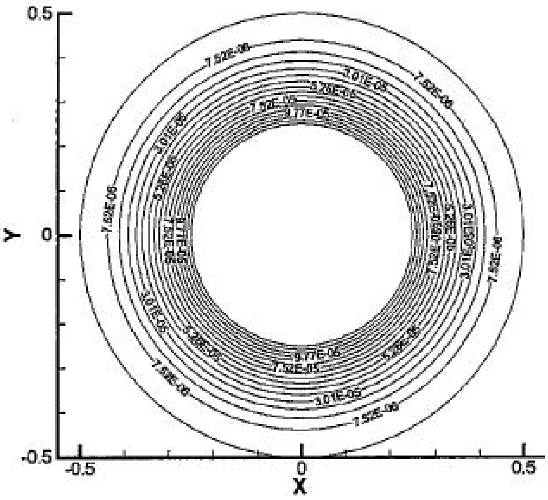

(a)

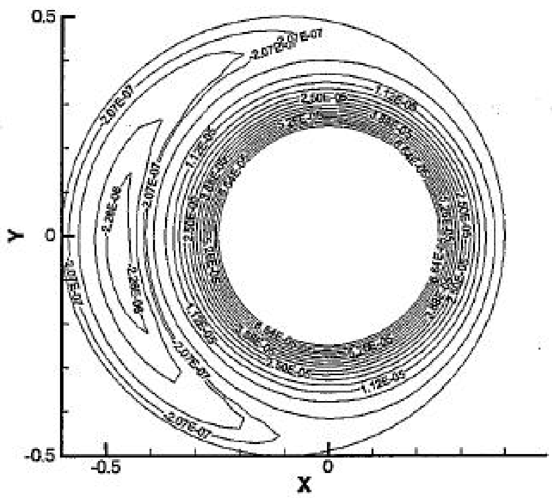

(b)

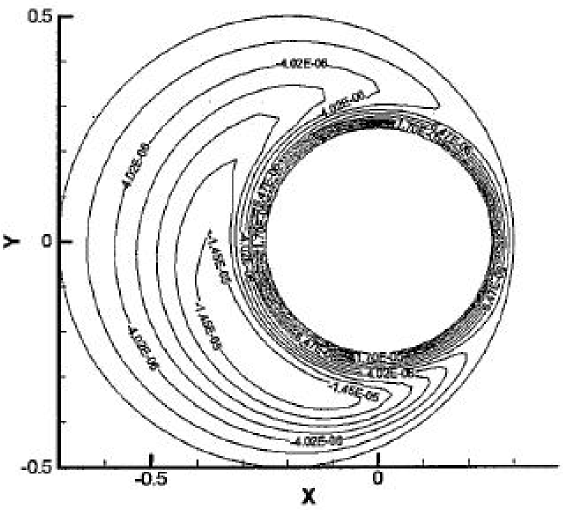

(c)

Figure 5. Streamline plot for Case 1 (a), Case 2 (b), and Case 3 (c)

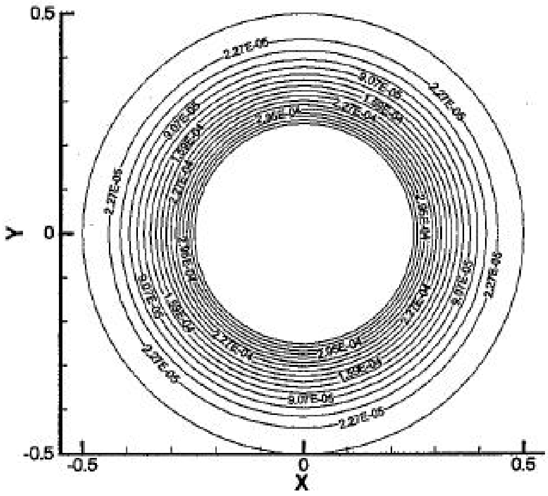

(a)

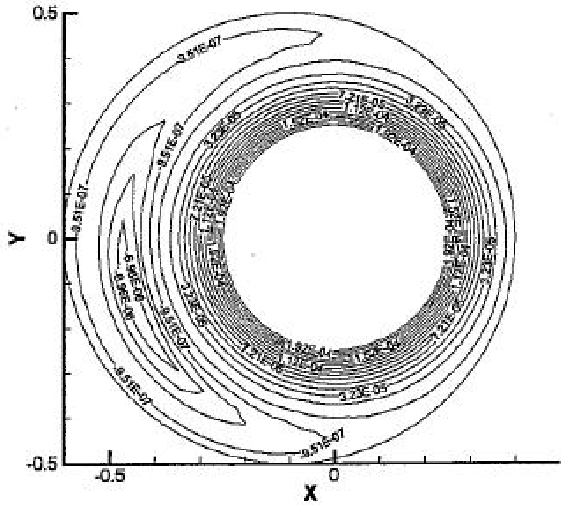

(b)

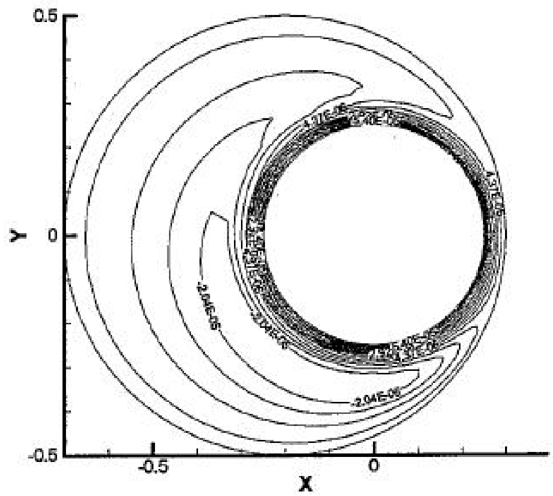

(c)

Figure 6. Streamline plot for Case 4 (a), Case 5 (b), and Case 6 (c)

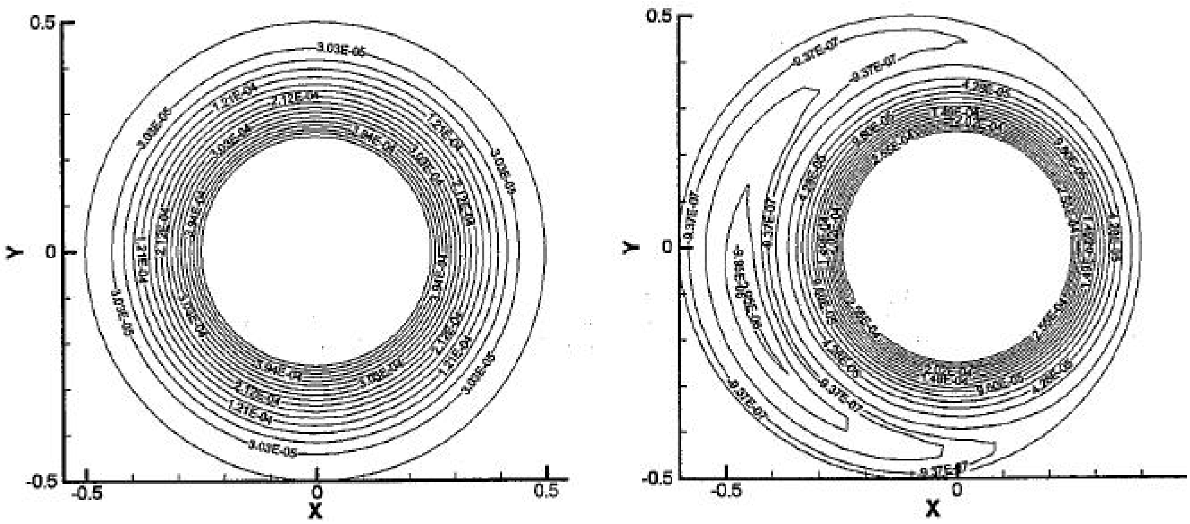

(a) **(b)**

Figure 7. Streamline plot for Case 7 (a), and Case 8 (b)

Case 9 did not converge on a stable solution within the present numerical framework. This case corresponds to a highly convection-dominated regime due to the combined effect of high Reynolds number and large eccentricity. The absence of stabilization techniques, such as upwinding for convective terms, leads to numerical instability under these conditions. Therefore, this case is excluded from the detailed analysis, although it provides useful insight into the limitations of the method.

The flow behavior is evaluated through velocity fields and streamline patterns. As the Reynolds number increases, the flow gradually shifts from a viscous-dominated regime to a convection-dominated one. This transition not only alters the flow structure but also affects numerical stability. In particular, for high Reynolds numbers and large eccentricities, the governing equations become strongly convection-dominated, which may lead to convergence difficulties in the absence of stabilization techniques.

Increasing eccentricity introduces significant geometric asymmetry, resulting in non-uniform velocity distributions. At low Reynolds numbers, the flow remains smooth and predominantly laminar. However, with increasing Reynolds number, inertial effects become dominant and lead to the formation of Taylor-type vortical structures, which intensify with both Reynolds number and eccentricity.

All simulations are carried out using a time-marching approach until steady-state is reached. Computational effort increases with Reynolds number and eccentricity due to stronger nonlinear effects.

The computational cost of the simulations, evaluated in terms of CPU time, is presented in Fig. 8 and Fig. 9 as a function of Reynolds number and eccentricity. As seen in Fig. 8, CPU time increases consistently with Reynolds number for all eccentricity levels due to the increasing dominance of convective effects, which introduce stronger nonlinearities and require more iterations for convergence. Similarly, Fig. 9 shows that higher eccentricity leads to increased CPU time, as geometric asymmetry results in more complex flow structures and slower convergence. The combined effect of high Reynolds number and large eccentricity significantly amplifies the computational effort, indicating that both parameters play a crucial role in determining not only the flow behavior but also the efficiency of the numerical solution procedure.

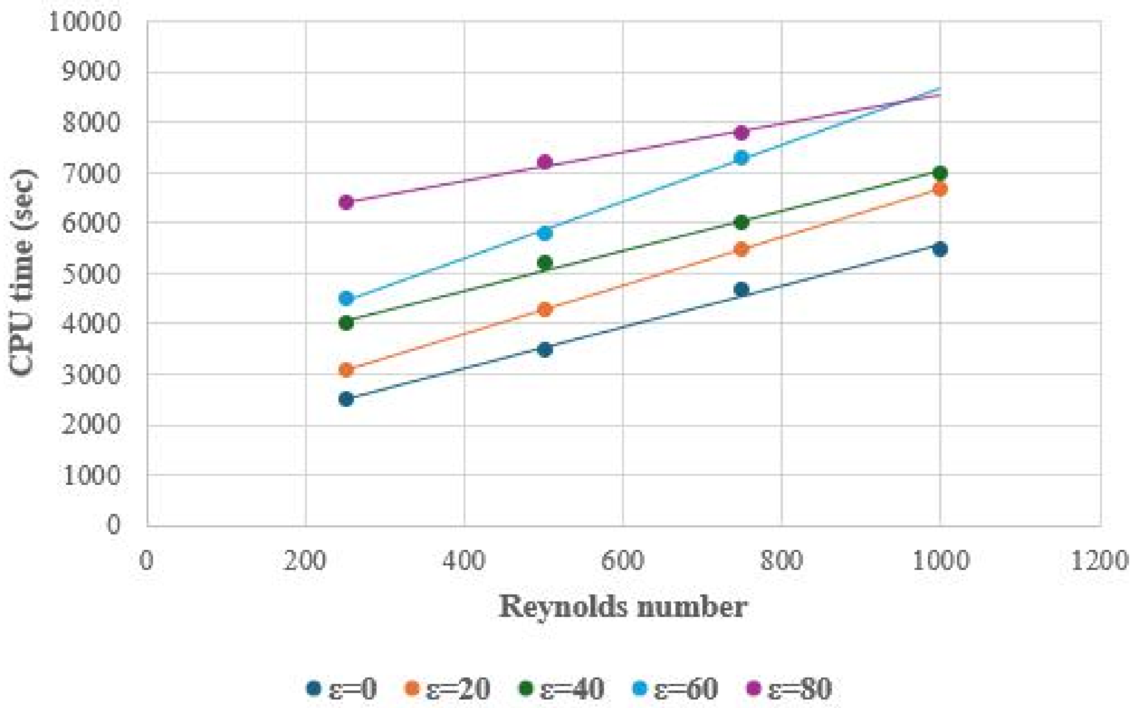

Figure 8. Effect of Reynolds number on CPU time

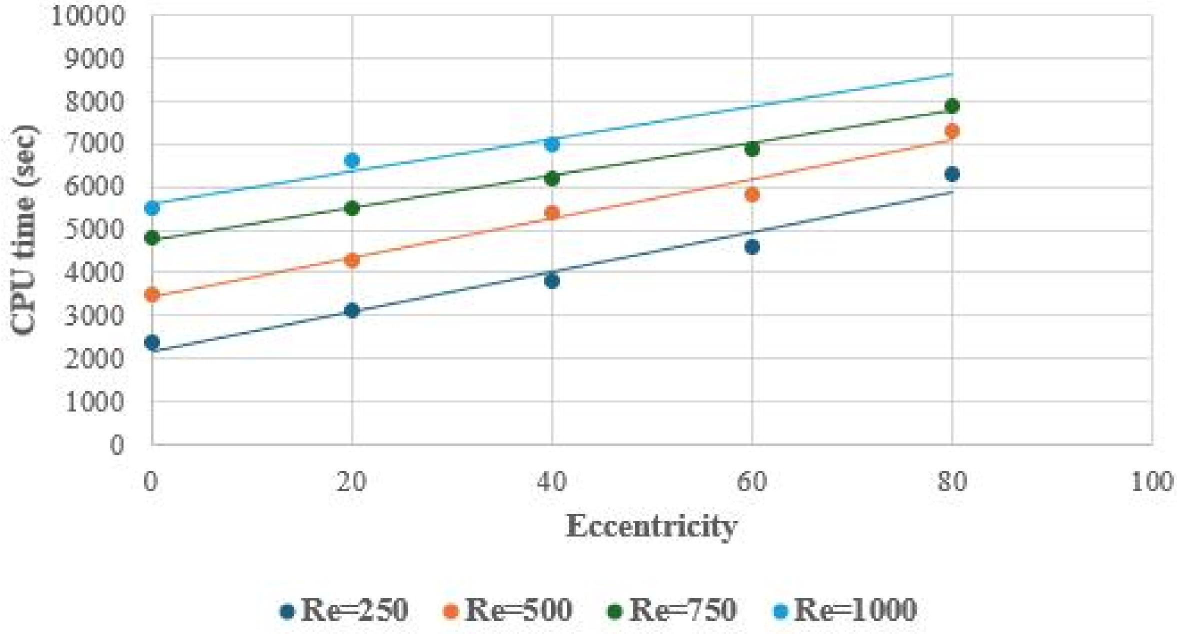

Figure 9. Effect of Eccentricity on CPU time

Validation of Results

The accuracy of the proposed numerical approach is assessed by comparing the computed results with the analytical solution available for the concentric annulus case. In this configuration, the inner cylinder rotates while the outer cylinder remains stationary, allowing a direct evaluation of the velocity distribution in the radial direction.

Fig. 10 presents the comparison between numerical and analytical velocity profiles for Re=250. A very good agreement is observed throughout the domain, with both solutions exhibiting nearly identical trends. The numerical results slightly overpredict the velocity values, particularly in the intermediate radial region, but the overall deviation remains limited.

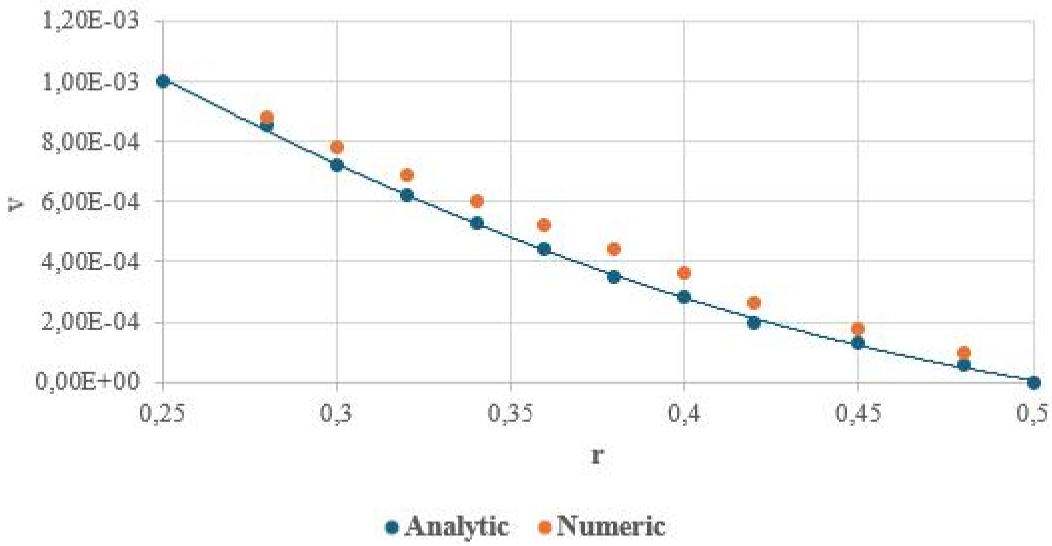

Figure 10. Comparison of Results with Analytical Solution for Re=250

This level of agreement demonstrates that the generalized finite difference method provides reliable predictions for laminar flow in annular geometries. The small deviations observed can be attributed to discretization effects and the numerical treatment of boundary conditions.

Conclusion

In this study, the flow within an eccentric annulus was successfully simulated using the generalized finite difference (meshless) method. The results demonstrate that the method is capable of accurately capturing the velocity distribution and flow structure over a range of Reynolds numbers and eccentricity ratios. The comparison with analytical solutions for the concentric case showed good agreement, with deviations remaining within acceptable limits.

The analysis revealed that both Reynolds number and eccentricity significantly influence the flow behavior, leading to increased asymmetry and the development of vortex structures at higher values. From a numerical perspective, it was observed that high Reynolds numbers and large eccentricities introduce convergence difficulties due to the dominance of convective effects. Although the method provides accurate and flexible solutions for complex geometries, it requires relatively high computational effort and may need stabilization techniques for convection-dominated flows. Future work should focus on incorporating turbulence modeling, improving the treatment of convective terms, and extending the approach to three-dimensional problems.

References

[1] Celebioğlu, T. K. (2002) *Spiraling Flow Through an Eccentric Annulus*, M.Sc. Thesis, Middle East Technical University, Department of Civil Engineering, Ankara, Turkiye.
[2] Snyder, W. T. and Goldstein, G. A. (1965) An analysis of fully developed laminar flow in an eccentric annulus, *A.I.Ch.E. Journal*, 11(3), 462–467.
[3] Jonsson, V. K. and Sparrow, E. M. (1966) Experiments on turbulent flow phenomena in eccentric annular ducts, *Journal of Fluid Mechanics*, 25(1), 65–86.
[4] Usui, H. and Tsuruta, K. (1980) Analysis of fully developed turbulent flow in an eccentric annulus, *Journal of Chemical Engineering of Japan*, 13(6).
[5] Dai, R., Dong, Q. and Szeri, A. Z. (1992) Flow between eccentric rotating cylinders: bifurcation and stability, *International Journal of Engineering Science*, 30(10), 1323–1340.
[6] Nouri, J. M., Umur, H. and Whitelaw, J. H. (1993) Flow of Newtonian and non-Newtonian fluids in concentric and eccentric annuli, *Journal of Fluid Mechanics*, 253, 617–641.
[7] Gravas, N. and Martin, B. W. (1978) Instability of viscous axial flow in annuli having a rotating inner cylinder, *Journal of Fluid Mechanics*, 86(2), 385–394.
[8] Kit, E. and Mazor, E. (1990) Numerical solution of laminar flow generated in an annulus by rotating screens, *Acta Mechanica*, 83, 9–24.
[9] Char, M. and Hsu, Y. (1998) Computation of buoyancy-driven flow in an eccentric centrifugal annulus with a non-orthogonal collocated finite volume algorithm, *International Journal for Numerical Methods in Fluids*, 26, 323–343.
[10] Quadrio, M. and Luchini, P. (2002) Direct numerical simulation of the turbulent flow in a pipe with annular cross-section, *European Journal of Mechanics B/Fluids*.
[11] Perrone, N. and Kao, R. (1975) A general finite difference method for arbitrary meshes, *Computers and Structures*, 5, 45–58.
[12] Liszka, T. (1984) An interpolation method for an irregular net of nodes, *International Journal for Numerical Methods in Engineering*, 20, 1599–1612.
[13] Gavete, L. and Cuesta, J. L. (2001) A numerical comparison of two different meshless methods, *European Conference on Computational Mechanics*.
[14] Benito, J. J., Ureña, F. and Gavete, L. (2001) Influence of several factors in the generalized finite difference method, *Applied Mathematical Modelling*, 25, 1039–1053.
[15] Liszka, T. and Orkisz, J. (1980) The finite difference method at arbitrary irregular grids and its application in applied mechanics, *Computers and Structures*, 11, 83–95.

Finite Element Method with Energy Minimization (FEMEM) in Structural Analysis with Applications to Tensegrity Structures

Yusuf Cengiz Toklu[1], Gebrail Bekdaş[2], Ayla Ocak[3] and *†Sinan Melih Nigdeli[2]

[1] Department of Civil Engineering, Istanbul Aydın University, 34295 Küçükçekmece/Istanbul/Türkiye
[2] Department of Civil Engineering, Istanbul University-Cerrahpaşa, 34320 Avcılar/Istanbul/Türkiye
[3] Smart Infrastructure Technician Program, Gelisim Vocational School, Istanbul Gelisim University, 34310 Avcılar/Istanbul/Türkiye

*Presenting author: melihnig@iuc.edu.tr
†Corresponding author: melihnig@iuc.edu.tr

Abstract

The Finite Element Method (FEM) has long been one of the most powerful computational techniques in structural engineering for the analysis of linear and nonlinear systems. Nevertheless, conventional FEM approaches may encounter significant limitations in problems involving severe geometric nonlinearity, unstable or under-constrained systems, multiple equilibrium configurations, progressive failure, and displacement constraints. To address these challenges, the Finite Element Method with Energy Minimization (FEMEM) has emerged as an alternative framework based on direct minimization of the total potential energy of structural systems. This paper presents a comprehensive state-of-the-art review of FEMEM in structural analysis. The theoretical background of FEMEM is discussed together with its fundamental differences from classical matrix-based FEM formulations. Existing FEMEM applications on trusses, cable networks, plane-stress and plane-strain systems, and three-dimensional continuum structures are reviewed to demonstrate the capabilities of the method in solving highly nonlinear structural problems. Particular emphasis is placed on tensegrity structures as representative examples of complex nonlinear systems. These examples demonstrate the effectiveness of FEMEM in capturing large displacements, prestressing effects, nonlinear material behavior, and multiple stable equilibrium states without requiring specialized nonlinear iterative formulations commonly employed in traditional FEM approaches. The findings indicate that FEMEM provides a robust and flexible computational framework for advanced structural analysis and shows strong potential for future applications in adaptive, deployable, and intelligent structural systems.

Keywords: Finite Element Method with Energy Minimization; FEMEM; nonlinear structural analysis; total potential energy optimization; tensegrity structures; cable-strut systems; metaheuristic algorithms; prestressed structures; structural stability; computational mechanics; deployable structures; energy minimization

Introduction

The Finite Element Method (FEM) has been the dominant numerical tool in structural mechanics for several decades and is widely recognized as the standard approach for structural analysis [1-2]. While conventional FEM is highly effective for linear structural analysis, numerous enhanced formulations have been developed to successfully address material and geometric nonlinearities [3-5]. Despite these advances, some static structural problems remain difficult or impossible to solve using conventional equilibrium-based FEM formulations. In certain cases, although the solution is straightforward from the perspective of energy minimization, an appropriate matrix equilibrium equation cannot be established.

To overcome this limitation, the Finite Element Method based on Energy Minimization (FEMEM), first introduced in 2004 [6, 7], was proposed. Like FEM, FEMEM begins by discretizing the structure into finite elements. However, instead of establishing equilibrium equations, it determines the structural response by minimizing the total potential energy stored in the elements. This energy-based formulation allows the analysis of structural problems that cannot be handled by either conventional or nonlinear FEM. Since its introduction, FEMEM has been successfully applied to several such problems, although further research is still needed to extend its applicability to a wider range of structural analysis problems.

FEM and FEMEM follow the same initial steps, including structural modeling, discretization into finite elements, node selection, and definition of shape functions. Their main difference lies in the solution procedure. FEM formulates and solves global equilibrium equations based on the stiffness matrix, whereas FEMEM determines the structural response by minimizing the total potential energy of the system while allowing displacement constraints to be incorporated naturally. As a result, FEMEM can successfully analyze problems involving geometric or material nonlinearities, multiple equilibrium configurations, under-constrained systems, and support failures, where conventional FEM may encounter difficulties or fail to converge. However, for linear structural analysis, FEM remains computationally more efficient and generally provides higher numerical accuracy. Therefore, FEMEM should be considered a complementary approach that extends the applicability of conventional FEM to a broader class of structural analysis problems.

The remainder of this paper is organized as follows. First, the fundamental concepts of the Finite Element Method with Energy Minimization (FEMEM) are introduced, together with a comparison between FEMEM and the conventional Finite Element Method (FEM), highlighting their respective advantages and limitations. This is followed by a comprehensive review of FEMEM applications to various structural systems, including truss structures, cable networks, plane-stress and plane-strain problems, and three-dimensional continuum structures. A brief description of the review methodology adopted for tensegrity-related studies is then provided. Subsequently, representative applications to tensegrity structures are presented to illustrate the capability of FEMEM in modeling highly nonlinear structural behavior, such as large displacements, prestressing effects, and multiple equilibrium configurations. Finally, the main findings of the review are summarized, current limitations of FEMEM are discussed, and potential directions for future research and practical structural engineering applications are outlined.

FEMEM Applications for Structural Systems

Truss structures were the first structural systems analyzed using FEMEM, initially introduced as Total Potential Optimization using Metaheuristic Algorithms (TPO/MA) [6,7]. Early studies demonstrated that FEMEM accurately solves both linear and nonlinear trusses with various constitutive models, including elastic, elastoplastic, strain-hardening, strain-softening, and buckling behaviors, while enabling progressive failure analysis through user-defined stress–strain relationships. Subsequent research extended FEMEM to space trusses [8], structures with multiple equilibrium configurations [9,10], unilateral supports [11, 12], smart trusses [13], thermal loading [14, 15], and unstable or under-constrained systems [16]. Numerous optimization algorithms have been integrated into FEMEM [17-22], while neural networks have also been explored as an alternative solution strategy [23]. More recently, FEMEM has been successfully applied to progressive failure analysis of trusses, demonstrating its capability to capture structural collapse sequences that are difficult to simulate using conventional FEM [24].

Cable network structures represent another important application area of FEMEM. Since cable elements cannot resist compression, these systems are inherently nonlinear and are commonly analyzed using iterative nonlinear FEM techniques [25]. FEMEM has been successfully applied to both prestressed and non-prestressed cable networks, producing highly accurate predictions while avoiding specialized nonlinear formulations [25-28]. Comparisons with established numerical solutions reported by Lewis [29], Thai and Kim [30] and Hau [31] confirmed the excellent accuracy and robustness of the FEMEM approach.

Tensegrity structures, consisting of discontinuous compression members and continuous tension elements, exhibit highly nonlinear behavior due to prestressing, large displacements, and multiple equilibrium states [32]. Conventional analysis methods generally rely on iterative Newton–Raphson-based formulations or other specialized nonlinear procedures [33-38]. In contrast, FEMEM analyzes tensegrity systems directly through energy minimization without requiring dedicated nonlinear solution strategies. The method has been successfully applied to various three-dimensional and planar tensegrity structures, including towers, habitats, cantilever beams, and multi-module systems, demonstrating accurate prediction of prestressed configurations and highly nonlinear responses [39-42].

FEMEM has also been extended to plane-stress and plane-strain problems, including plates with openings, soil–structure interaction, and other two-dimensional continuum systems [43-47]. For linear problems, FEMEM results show excellent agreement with conventional FEM, while hypothetical nonlinear constitutive models have been introduced to evaluate its performance in nonlinear analyses. Different metaheuristic optimization algorithms have been investigated, with most providing solutions comparable to FEM in terms of total potential energy, demonstrating the flexibility and effectiveness of the energy-minimization framework.

The application of FEMEM to three-dimensional continuum structures is relatively recent. Existing studies have considered cantilever beams, thick plates, and three-dimensional prisms discretized using eight-node hexahedral elements [48]. The reported results indicate that FEMEM achieves satisfactory accuracy, with improved solution quality obtained through finer finite-element discretizations, suggesting promising potential for more complex three-dimensional structural analyses in future research.

In Fig. 1, the progress of FEMEM for different types of structural analyses were shown. Also, recent review studies have summarized the development and applications of FEMEM in structural engineering [49, 50]. Building upon these contributions, the present review provides a more comprehensive discussion of FEMEM applications across different structural systems, with particular emphasis on tensegrity structures.

FEMEM Methodology for Tensegrity Structures

Tensegrity structures exhibit highly nonlinear behavior due to large displacements, prestressing, and the interaction between tension-only cables and compression struts. Their equilibrium is governed by the minimum total potential energy rather than solely by force equilibrium. Unlike conventional finite element formulations, which solve nonlinear equilibrium equations iteratively, the Finite Element Method with Energy Minimization (FEMEM) determines the equilibrium configuration by directly minimizing the total potential energy of the structure using a metaheuristic optimization algorithm.

The analysis starts with the discretization of the tensegrity structure into bar and cable elements. The initial geometry, material properties, prestressing conditions, external loads, and boundary conditions are defined. The nodal displacement vector,

$$D = \left[u_1 \; v_1 \; w_1 \cdots u_{Nj} \; v_{Nj} \; w_{Nj}\right], \tag{1}$$

is considered as the set of optimization variables.

For each candidate displacement field, the deformed length of every member is evaluated from its nodal coordinates. The corresponding strain is computed as

$$\varepsilon = \frac{L_D - L_0}{L_0}, \tag{2}$$

where $L_0$and Ldenote the initial and deformed member lengths, respectively. The constitutive model is then used to determine the stress, including prestress when applicable,

$$\sigma = \sigma(\varepsilon) + \sigma_0. \tag{3}$$

The strain energy density is obtained from the stress–strain relationship,

$$e(\varepsilon) = \int_0^{\varepsilon} \sigma(\varepsilon) d\varepsilon + \sigma_0 \varepsilon. \tag{4}$$

and the strain energy of each element is calculated by

$$S = ALe, \tag{5}$$

where A is the cross-sectional area. The total potential energy of the structure is then formulated as

$$U(\varepsilon) = \sum_{j=1}^{N_m} e_j A_j L_j - \sum_{i=1}^{N_P} P_i u_i \tag{6}$$

where the first term represents the total internal strain energy and the second term denotes the work done by the external loads. Additional prestressing energy can be incorporated when required.

The objective of FEMEM is to determine the displacement vector that minimizes the total potential energy using a metaheuristic optimization algorithm. Since the optimization procedure is independent of the energy formulation, different algorithms such as Harmony Search, Genetic Algorithms, Particle Swarm Optimization, Differential Evolution, JAYA, Teaching–Learning-Based Optimization, and other population-based methods can be employed within the same framework. After convergence, the optimal displacement field is used to evaluate member forces, stresses, reactions, and the final deformed configuration. This energy-based formulation naturally accommodates large displacements, prestressing, tension-only cable behavior, and multiple equilibrium states without requiring specialized nonlinear iterative solution schemes. In Fig. 2, the general methodology is summarized.

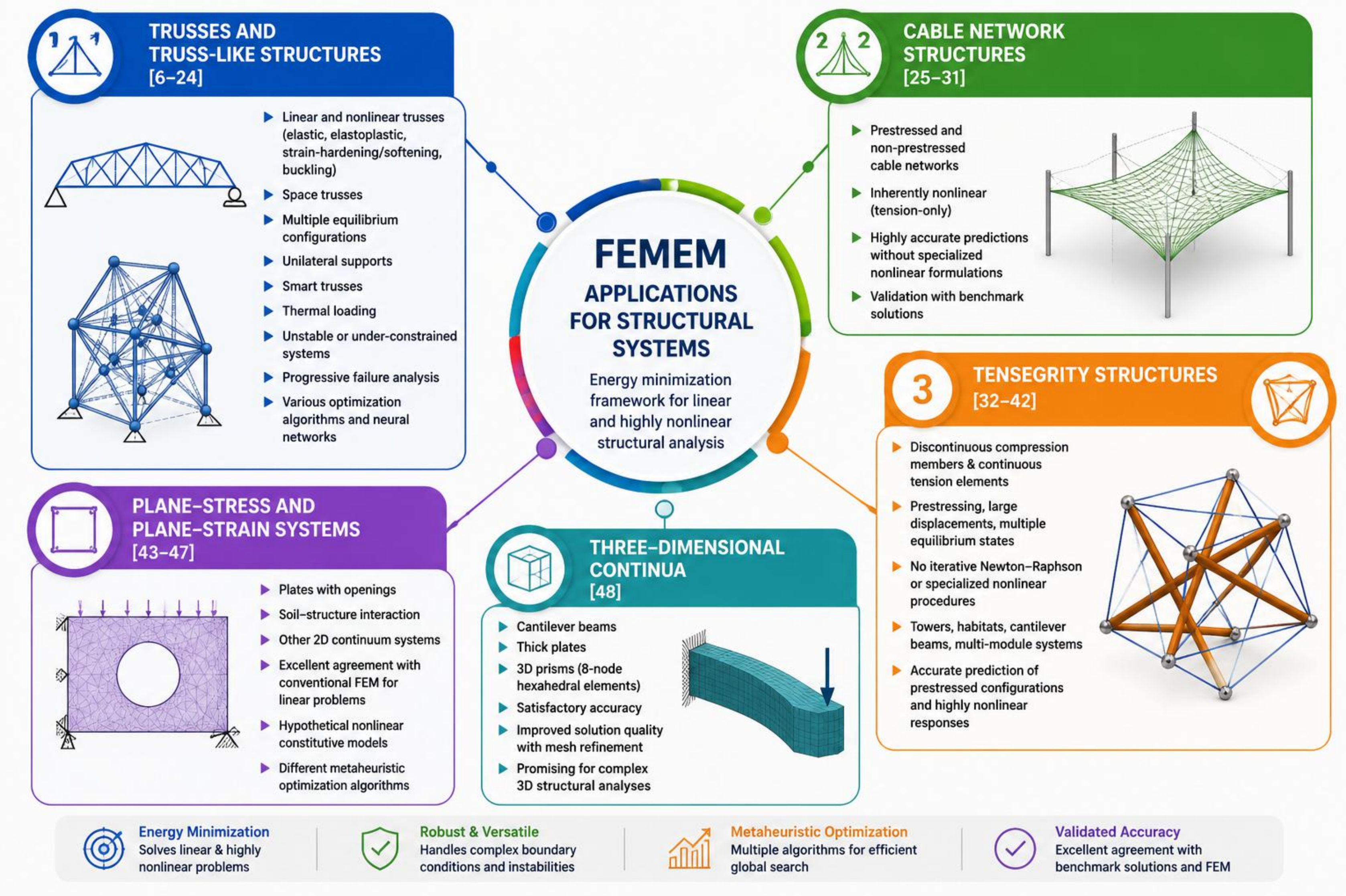

Figure 1. FEMEM Applications for Structural Systems and Advantages

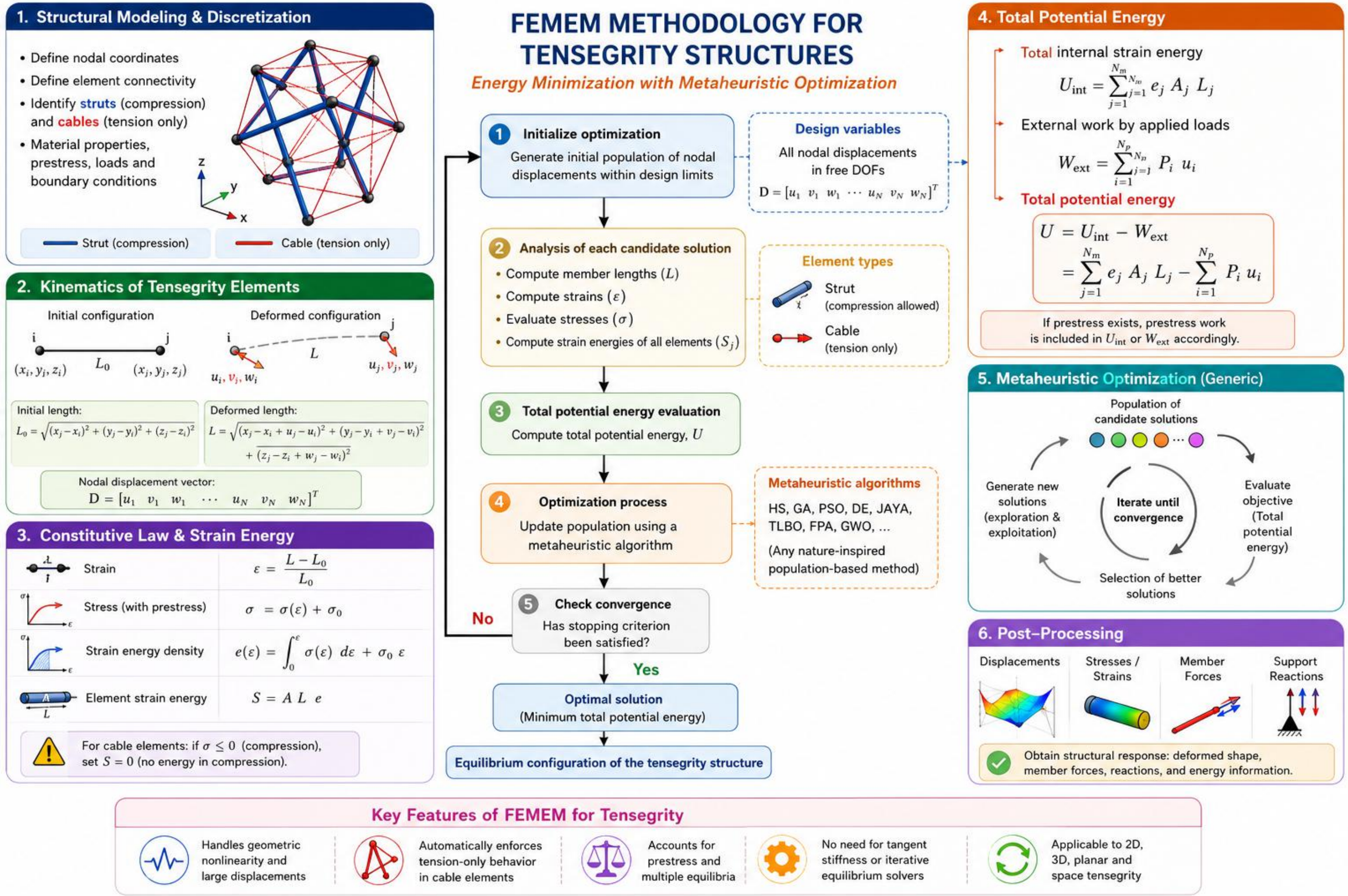

Figure 2. FEMEM Methodology for Tensegrity Structures

Tensegrity Structure Example

The example considers a single-layer cyclic tensegrity structure [51] consisting of 8 struts and 24 cables, with the base nodes fully restrained and a concentrated vertical load applied to the upper node. The structural geometry, nodal coordinates, and properties including harmony search (HS) [52] parameters are presented in Fig. 3, Table 1, and Table 2, respectively.

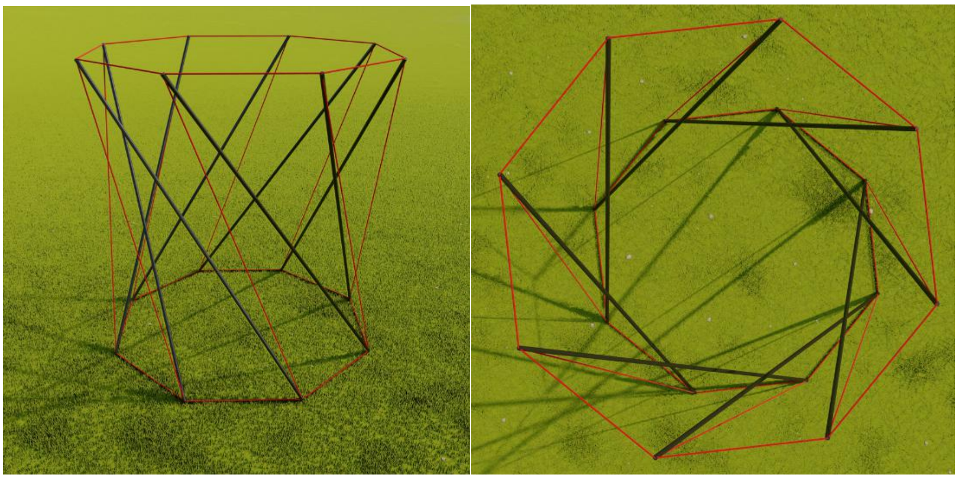

Figure 3. The structural geometry [42]

Table 1. Joint Coordinates [51]

Node	Coordinates (mm)		
	x	y	z
1	0	500	0
2	-353.553	353.553	0
3	-500	0	0
4	-353.553	-353.553	0
5	0	-500	0
6	353.553	-353.553	0
7	500	0	0
8	353.553	353.553	0
9	0	500	1000
10	-353.553	353.553	1000
11	500	0	1000
12	-353.553	-353.553	1000
13	0	-500	1000
14	353.553	-353.553	1000
15	500	0	1000
16	353.553	353.553	1000

Table 3. Joint Coordinates

Symbol	Definition	Value
$HMCR$	Harmony Memory Considering Rate	0.5-1
$HMCR_{in}$	Initial Harmony Memory Considering Rate	0.5
FW	Fret Width	0-0.05
FW_{in}	Initial Fret Width	0.05

mt	Maximum iteration number	100000
t	Iteration number	1-100000
pn	Population number	30
s	Number of struts	8
c	Number of cables	24
A_1	Cross-sectional area of struts (mm^2)	Different for cases
A_2	Cross-sectional area of cables (mm^2)	Different for cases
E	Modulus of elasticity of all elements (kN/mm^2)	200

To investigate the influence of member stiffness on the structural response, a parametric study was performed by considering sixteen cases with different cross-sectional areas of the struts (A_1) and cables (A_2). The cross-sectional areas of both member types were increased proportionally from 50–200 mm² for the struts and 5–20 mm² for the cables. For each case, the equilibrium configuration was determined using the HS within the FEMEM framework. The optimization process was terminated when the minimum total potential energy was obtained or the maximum number of iterations was reached. The resulting minimum total potential energy, convergence iteration, and nodal displacements are summarized in Table 4.

Table 4. The results for different cases

					Maximum and Minimum Displacements (mm)					
Case	A_1 (mm^2)	A_2 (mm^2)	Energy (Nmm)	Iteration	u	v	w	u	v	w
1	50	5	-1.4807E+09	66714	624.4828	0	0	0	-1769.9	-1000
2	60	6	-1.4249E+09	54476	612.4459	0	0	0	-1771.79	-1000
3	70	7	-1.3714E+09	99814	603.19	0	0	0	-1773.45	-1000
4	80	8	-1.3193E+09	79486	595.8676	0	0	0	-1774.91	-1000
5	90	9	-1.2682E+09	100000	589.9274	0	0	0	-1776.21	-999.934
6	100	10	-1.2174E+09	99996	587.2166	0	0	0	-1767.09	-956.6
7	110	11	-1.1669E+09	99998	572.7811	0	0	0	-1747.09	-878.937
8	120	12	-1.1172E+09	99998	527.3383	0	0	0	-1671.58	-750.143
9	130	13	-1.0714E+09	99636	484.2275	0	0	0	-1631.42	-673.352
10	140	14	-1.0294E+09	99971	432.3103	0	0	0	-1583.08	-580.892
11	150	15	-9.9112E+08	99981	388.253	0	0	0	-1537.46	-520.713
12	160	16	-9.5606E+08	99403	338.5127	0	32.95075	0	-1487.37	-465.076
13	170	17	-9.2390E+08	98718	289.9687	0	90.12741	-67.9236	-1426.5	-530.816
14	180	18	-8.9483E+08	99029	438.202	0	107.2765	-81.954	-1399.78	-417.525
15	190	19	-8.6791E+08	99999	232.4078	0	129.0144	-122.335	-1358.53	-360.782
16	200	20	-8.4310E+08	99555	201.7603	53.23456	143.5578	-156.855	-1320.08	-336.901

The results demonstrate that increasing the cross-sectional areas of both the struts and cables significantly affects the structural response. As the member areas increase from Case 1 to Case 16, the minimum total potential energy gradually increases from -1.48×10^9 Nmm to -8.43×10^8 Nmm, indicating a reduction in the strain energy stored in the structure due to the increased overall stiffness.

A similar trend is observed for the displacement response. The maximum displacement in the u-direction decreases continuously from 624.5 mm to 201.8 mm, while the largest negative displacement in the v-direction is reduced from approximately -1770 mm to -1320 mm. Likewise, the maximum negative w-displacement decreases from -1000 mm to approximately

-337 mm. These results confirm that increasing the cross-sectional areas leads to a considerably stiffer tensegrity system with reduced deformation under the same external loading.

The optimization converged successfully for all sixteen cases. The first four cases converged before 80000 iterations, whereas most of the remaining cases required nearly the maximum allowable iterations, suggesting that stiffer structures produce a more complex optimization landscape. Nevertheless, stable equilibrium configurations were obtained for every case, demonstrating the robustness of the HS-based FEMEM approach over a broad range of structural stiffnesses.

An interesting observation is that the response remains nearly symmetric for the first eleven cases, where the maximum displacement occurs mainly in the u-direction. For larger member cross-sectional areas (Cases 12-16), non-zero displacements also develop in the transverse v- and w-directions, indicating a change in the equilibrium configuration and the emergence of a different deformation mode. This behavior illustrates the capability of FEMEM to capture changes in equilibrium states associated with variations in structural stiffness.

Conclusions

This paper presented a comprehensive review of the Finite Element Method with Energy Minimization (FEMEM) and its applications to structural analysis. Unlike the conventional finite element method, which determines the equilibrium state by solving matrix equilibrium equations, FEMEM directly searches for the minimum total potential energy of the structural system through optimization. This energy-based formulation enables the analysis of structural problems involving large displacements, prestressing, multiple equilibrium configurations, unstable or under-constrained systems, and other highly nonlinear behaviors that may be difficult to address using conventional FEM formulations.

The review demonstrated that FEMEM has been successfully applied to a wide range of structural systems, including truss structures, cable networks, plane-stress and plane-strain continua, three-dimensional solid structures, and tensegrity systems. The flexibility of the formulation allows different metaheuristic optimization algorithms to be incorporated without modifying the underlying energy equations, making FEMEM a versatile computational framework for nonlinear structural analysis.

A representative tensegrity example was also presented to demonstrate the practical application of the method. A parametric investigation involving different cross-sectional areas of struts and cables showed that increasing member stiffness reduced the structural deformation and increased the minimum total potential energy, while the optimization algorithm successfully converged for all investigated cases. Furthermore, changes in member stiffness altered the equilibrium configuration and deformation pattern, illustrating the capability of FEMEM to capture multiple nonlinear equilibrium states and complex structural responses.

Although the current applications of FEMEM have produced promising results, further research is still needed to expand its application to other structural systems, including beam, frame, plate-bending, shell, and coupled structural models, as well as dynamic, stability, fracture, and multiphysics problems. Future developments may also focus on improving computational efficiency through advanced optimization algorithms, parallel computing techniques, and machine learning-assisted optimization. Considering its robust theoretical foundation and continuously expanding range of applications, FEMEM has the potential to become an effective alternative computational framework for solving challenging structural mechanics problems that are difficult to analyze using conventional finite element formulations.

References

[1] Gupta, K. K., & Meek, J. L. (1996). A brief history of the beginning of the finite element method. International journal for numerical methods in engineering, 39(22), 3761-3774.
[2] Sabat, L., & Kundu, C. K. (2020). History of finite element method: a review. Recent Developments in Sustainable Infrastructure: Select Proceedings of ICRDSI 2019, 395-404.
[3] De Borst, R., Crisfield, M. A., Remmers, J. J., & Verhoosel, C. V. (2012). Nonlinear finite element analysis of solids and structures. John Wiley & Sons.
[4] Reddy, J. N. (2014). An Introduction to Nonlinear Finite Element Analysis Second Edition: with applications to heat transfer, fluid mechanics, and solid mechanics. OUP Oxford.
[5] Belytschko, T., Liu, W. K., Moran, B., & Elkhodary, K. (2014). Nonlinear finite elements for continua and structures. John wiley & sons.
[6] Toklu, Y. C. (2004). Application of optimization techniques to structural analyses: truss example. In Structures 2004: Building on the Past, Securing the Future (pp. 1-12).
[7] Toklu, Y. C. (2004). Nonlinear analysis of trusses through energy minimization. Computers & structures, 82(20-21), 1581-1589.
[8] Toklu, Y. C., Bekdaş, G., Temür, R., Toklu, Ş. Ç., Uzun, F. (2013). Nonlinear Analysis of Structures by Total Potential Optimization using Meta-heuristic Algorithms (TPO/MA). European Group for Intelligent Computing in Engineering, EG-ICE 2013, 20th International Workshop: Intelligent Computing in Engineering, Technical University of Vienna, Austria, July 01 - 03, 2013
[9] Toklu, Y. C., Temür, R., & Bekdaş, G. (2015a). Computation of nonunique solutions for trusses undergoing large deflections. International Journal of Computational Methods, 12(03), 1550022.
[10] Toklu, Y. C. (2023). Nonlinear Analysis of Structures by Total Potential Optimization Using Metaheuristic Algorithms (TPO/MA). Journal of Civil Engineering and Architecture, 17, 152-160.
[11] Bekdaş, G., Temür, R., & Toklu, Y. C. (2014). Analysis of Structures with Unilateral Boundary Conditions. Metaheuristics and Engineering, 113.
[12] Temur, R., Bekdaş, G., Türkan, Y. S., & Toklu, Y. C. (2014). Investigating the behavior of the truss structures with unilateral boundary conditions. In 5th European Conference of Civil Engineering (ECCIE'14) (pp. 22-24).
[13] Toklu, Y. C., & Arditi, D. (2014). Smart trusses for space applications. In 14th ASCE international conference on engineering, science, construction and operations in challenging environments. Earth and Space (pp. 27-29).
[14] Bekdaş, G., Temür, R., & Toklu, Y. C. (2014). Analyses of truss structures under thermal effects. In 5th European Conference of Civil Engineering (ECCIE'14) (pp. 22-24).
[15] Toklu, Y. C., Bekdaş, G., & Temür, R. (2015). Investigation of thermal effects on analyses of truss structures via metaheuristic approaches. In 6th European Conference of Civil Engineering. Budapest, Hungary.
[16] Toklu, Y. C., Bekdaş, G., & Nigdeli, S. M. (2018). Analysis of under-constrained and unstable structures by the method TPO/MA. In AIP Conference Proceedings (Vol. 1978, No. 1). AIP Publishing.
[17] Toklu, Y. C., Bekdaş, G., & Temur, R. (2013c). Analysis of trusses by total potential optimization method coupled with harmony search. Structural Engineering and Mechanics, 45(2), 183-199.
[18] Toklu, Y. C., Temur, R., & Bekdas, G. (2015c). Teaching learning based optimization algorithm for analyses of trusses considering elastoplastic behavior. Fluids, Heat and Mass Transfer, Mechanical and Civil Engineering; Recent Advances in Mechanical Engineering Series, 17.
[19] Bekdaş, G., Temür, R., & Toklu, Y. C. (2015). Analyses of truss structures via total potential optimization implemented with teaching learning based optimization algorithm. In 3rd International Conference on Optimization Techniques in Engineering.
[20] Bekdaş, G., Kayabekir, A. E., Nigdeli, S. M., & Toklu, Y. C. (2019). Advanced energy-based analyses of trusses employing hybrid metaheuristics. The Structural Design of Tall and Special Buildings, 28(9), e1609.
[21] Bekdaş, G., Nigdeli, S. M., & Toklu, Y. C. (2023). A modified Jaya algorithm and application to structural analysis of trusses. In AIP Conference Proceedings (Vol. 2849, No. 1). AIP Publishing.
[22] Nigdeli, S. M., Bekdaş, G., Yücel, M., Kayabekir, A. E., & Toklu, Y. C. (2022). Analysis of non-linear structural systems via hybrid algorithms. In Intelligent Computing & Optimization: Proceedings of the 4th International Conference on Intelligent Computing and Optimization 2021 (ICO2021) 3 (pp. 536-545). Springer International Publishing.
[23] Mai, H. T., Lieu, Q. X., Kang, J., & Lee, J. (2022). A robust unsupervised neural network framework for geometrically nonlinear analysis of inelastic truss structures. Applied Mathematical Modelling, 107, 332-352.
[24] Aras, D. (2024) Progressive collapse analysis of truss systems (in Turkish), MS Thesis, Eskişehir Osmangazi University
[25] Toklu, Y. C., Bekdaş, G., & Temür, R. (2017). Analysis of cable structures through energy minimization. Structural Engineering and Mechanics, 62(6), 749-758.

[26] Temur, R., Bekdaş, G., & Toklu, Y. C. (2014). Analysis of cable structures through total potential optimization using meta-heuristic algorithms. In ACE2014, 11th International Congress on Advances in Civil Engineering (pp. 21-25).
[27] Kayabekir, A. E., Nigdeli, S. M., Bekdaş, G., & Toklu, Y. C. (2018, June). The analyses of spatial cable structures employing new generation metaheuristic methods. In 9th GRACM 2018 International Congress on Computational Mechanics (pp. 4-6).
[28] Nigdeli, S. M., Bekdaş, G., & Toklu, Y. C. (2019). Total potential energy minimization using metaheuristic algorithms for spatial cable systems with increasing second order effects. In 12th International Congress on Mechanics (HSTAM2019) (pp. 22-25).
[29] Lewis, W. J. (1989). The efficiency of numerical methods for the analysis of prestressed nets and pin-jointed frame structures. Computers & Structures, 33(3), 791-800.
[30] Thai, H. T., & Kim, S. E. (2011). Nonlinear static and dynamic analysis of cable structures. Finite elements in analysis and design, 47(3), 237-246.
[31] Hậu, M. T. (2025). Physics-informed differential evolution for nonlinear analysis of cable nets. Journal of Science and Technology-IUH, 73(1).
[32] Kahla, N. B., & Kebiche, K. (2000). Nonlinear elastoplastic analysis of tensegrity systems. Engineering Structures, 22(11), 1552-1566.
[33] Gaiotti, R., & Smith, B. S. (1989). P-delta analysis of building structures. Journal of Structural Engineering, 115(4), 755-770.
[34] Skelton, R. E., Helton, J. W., Adhikari, R., Pinaud, J. P., & Chan, W. (2017). An introduction to the mechanics of tensegrity structures. In The mechanical systems design handbook (pp. 315-388). CRC Press.
[35] Juan, S. H., & Tur, J. M. M. (2008). Tensegrity frameworks: Static analysis review. Mechanism and Machine Theory, 43(7), 859-881.
[36] Nuhoglu, A., & Korkmaz, K. A. (2011). A practical approach for nonlinear analysis of tensegrity systems. Engineering with Computers, 27, 337-345.
[37] Tran, H. C., & Lee, J. (2011). Geometric and material nonlinear analysis of tensegrity structures. Acta Mechanica Sinica, 27, 938-949.
[38] Li, H., Zhang, H., Zheng, Y., & Zhang, L. (2016). A peridynamic model for the nonlinear static analysis of truss and tensegrity structures. Computational Mechanics, 57(5), 843-858.
[39] Toklu, Y. C., Temür, R., Bekdaş, G., & Uzun, F. (2013). Space applications of tensegric structures. In 2013 6th International Conference on Recent Advances in Space Technologies (RAST) (pp. 29-32). IEEE.
[40] Toklu, Y. C., Uzun, F., Bekdas, G., Temur, R. (2014a). Structural Analysis of Tensegric Structures for Space Applications. 14th ASCE International Conference on Engineering, Science, Construction and Operations in Challenging Environments, Earth and Space 2014,"Engineering for Extreme Environments". October 27-29, 2014, St. Louis, Missouri, USA
[41] Toklu, Y. C., & Uzun, F. (2016). Analysis of tensegric structures by total potential optimization using metaheuristic algorithms. Journal of Aerospace Engineering, 29(5), 04016023
[42] Bekdaş, G., Ocak, A., Nigdeli, S. M., & Toklu, Y. C. (2024). A metaheuristic-based method for analysis of tensegrity structures. The Structural Design of Tall and Special Buildings, 33(7), e2091.
[43] Toklu, Y. C., Yayli, M. O., & Altan, B. (2014b). Analysis of plane stress problems as optimization problems. METAHEURISTICS AND ENGINEERING, Bilecik University, pp.45-47
[44] Toklu, Y. C., Kayabekir, A. E., Bekdaş, G., Nigdeli, S. M., & Yücel, M. (2020). Analysis of plane-stress systems via total potential optimization method considering nonlinear behavior. Journal of Structural Engineering, 146(11), 04020249.
[45] Kayabekir, A. E., Toklu, Y. C., Bekdaş, G., Nigdeli, S. M., Yücel, M., & Geem, Z. W. (2020). A novel hybrid harmony search approach for the analysis of plane stress systems via total potential optimization. Applied Sciences, 10(7), 2301.
[46] Toklu, Y. C., Bekdaş, G., Yücel, M., Nigdeli, S. M., Kayabekir, A. E., Kim, S., & Geem, Z. W. (2021). Total potential optimization using metaheuristic algorithms for solving nonlinear plane strain systems. Applied Sciences, 11(7), 3220.
[47] Temür, R. (2021). Analyses of plane stress and plane strain through energy minimization. In Structures (Vol. 33, pp. 728-736). Elsevier.
[48] Can, U. C., Ozbasaran, H., Toklu, Y. C. (2022) "Structural Analysis of Solids using Finite Element Method with Optimization" ICONDATA'22 (5th International Conference on Data Science and Applications). 7 - 11 September 2022, Fethiye – Mugla, Türkiye.
[49] Bekdaş, G., Ocak, A., Nigdeli, S. M., Toklu, Y. C., Kim, S., & Geem, Z. W. (2025). Total Potential Optimization Using Metaheuristic Algorithms for Analysis of Structural Systems. In Optimization Methods for Finite Element Analysis and Design (pp. 107-130). CRC Press.
[50] Toklu, Y. C., & Kaya, Y. (2026). Finite element method with energy minimization (FEMEM) in structural analysis: State-of-the-art. Challenge Journal of Structural Mechanics, 12(2), 145-161.
[51] Murakami, H. (2001). Static and dynamic analyses of tensegrity structures. Part 1. Nonlinear equations of motion. International Journal of Solids and Structures, 38(20), 3599-3613.

[52] Geem, Z.W.; Kim, J.H.; Loganathan, G. V. A new heuristic optimization algorithm: harmony search. Simulation 2001, 76(2), 60-68.

A Confidence-Gated Seismic DT-Driven CPS Framework for Trustworthy Structural Monitoring

*Ahsan Shahbaz1, †Baiping Dong2

[1]School of Civil Engineering, Tongji University, Shanghai 200092, China.

*Presenting author: ahsanshahbaz1998@gmail.com

†Corresponding author: baipingdong@tongji.edu.cn

Abstract

Seismic structural monitoring requires rapid adaptation of sensing and computation while confirming that uncertain measurements or inconsistent digital-twin (DT) outputs are not released as reliable information. This study proposes a confidence-gated seismic DT-driven cyber-physical system (CPS) framework that integrates event-triggered operation, edge-level data assurance, DT updating, and governed service release. Time-critical functions, including timestamp validation, buffering, data-completeness assessment, synchronization, event confirmation, and hard-constraint screening, are performed close to the data source. Higher-fidelity state estimation, model updating, persistent storage, and cross-event analysis are allocated to digital-twin and cloud resources according to their timing and computational requirements. A provisional system-level confidence index combines signal quality, data completeness, synchronization, physical-digital consistency, and latency adequacy. When integrated with hard-constraint checks, the index classifies each output as trusted, requiring engineering review, or fail-safe. The major contribution is the decoupling of event recognition from update permissibility, which avoids a detected event from being automatically regarded as a reliable structural state. The proposed framework also presents layered architecture, computational workflow, audit criteria, and staged evaluation pathway. Calibration and validation using field-monitoring data or real-time hybrid simulation are required before any automated feedback function can be authorized.

Keywords: digital twin; cyber-physical system; seismic structural monitoring; confidence assessment; edge computing; event-triggered operation

1. Introduction

Cyber-physical systems (CPS) and digital-twin (DT) technology have emerged as advanced technologies enabling real-time structural control, predictive analysis, and optimizing of maintenance strategies [1]. DT provides evolving virtual representations of physical assets, whereas CPS connect sensing, communication, computation, and physical or organizational response. Their integration has therefore attracted increasing attention in structural health monitoring, predictive maintenance, and intelligent infrastructure management [1–5]. Recent structural DT applications have demonstrated sensor integration, model updating, and visualization [2,3,5], while CPS studies have established distributed sensing and real-time communication architectures [4,6,7]. Despite significant progress in the individual development of CPS and DT, there is a lack of a practical seismic deployment framework.

Seismic monitoring introduces requirements that are not fully represented by general-purpose DT-CPS frameworks. The system operates for long periods under normal conditions but must rapidly increase sensing and processing activity during a transient event. At the same time, strong motion may increase packet loss, timing uncertainty, sensor saturation, and disagreement between measured and model-estimated responses. Dong et al. reviewed the available conventional frameworks and identified data acquisition, management, synchronization, and feedback control as major challenges; however, these frameworks do not quantify the latency tolerances, creating feasibility problems [1]. Similarly, existing DT implementations by Angjeliu et al., Hielscher et al., and Li et al. for structural health monitoring (SHM) demonstrate strong capabilities in post-event analysis but lack the real-time closed-loop actuation for seismic events [8–10].

This study addresses these limitations by advancing the framework proposed by Dong et al. from a descriptive layer arrangement to an operational decision framework for seismic monitoring [1]. The proposed confidence-gated seismic DT-driven CPS framework provides the supervisory mechanism that coordinates event-dependent system operation, assigns functions according to their timing and computational requirements, and regulates whether each digital-twin update is accepted, withheld for engineering review, or rejected. The framework is therefore focuses not on developing another structural model, but on how sensing, computation, digital representation, and service delivery should integrate when the reliability of the available information is uncertain.

The previously published framework by Dong et al. introduced a general five-layer framework for integrating CPS and DT in structural engineering [1]. In contrast, the present study develops this broad conceptual framework into a seismic-specific operational framework. It introduces event-dependent monitoring modes, explicit allocation of operations between edge and DT/cloud resources, confidence-based control of DT update release, hard-constraint overrides, and auditable trusted, review, and fail-safe decision states. The proposed framework therefore extends Dong et al.'s architecture by defining how sensing, computation, model evaluation, and service releases should be coordinated when data and model reliability may be affected during and after a seismic event.

This research work formalizes four interconnected mechanisms, which are mode-dependent operation over the earthquake-monitoring cycle, edge–cloud task allocation, confidence-based update admissibility with hard-constraint overrides, and auditable service governance incorporating provenance, version control, human review, and rollback. All mechanisms together provides a structured basis for translating the general five layers of the DT-driven CPS framework into a testable implementation specification. The remaining sections presents the proposed framework and operational logic, defines the computational workflow, and outlines the staged pathways for future implementation and evaluation.

2. Proposed confidence-gated seismic DT-driven CPS framework

The proposed framework extends the five-layer DT-driven CPS architecture of Dong et al. for seismic structural monitoring by integrating event-dependent operating modes, edge-level data assurance, edge–cloud task allocation, confidence-gated DT updating, and auditable service release within a unified operational structure. The proposed framework is designed mainly for structural monitoring, condition evaluation, engineering review, and alert assistance. Accordingly, event thresholds, confidence weights, synchronization tolerances, latency limits, and hard-constraint criteria must be calibrated for the monitored structure, sensing system, and intended service. Table 1 summarizes the resulting design requirements and corresponding framework mechanisms, which provide the basis for the layered architecture presented in the following subsection.

Table 1. Operational design requirements and corresponding framework mechanisms

Design requirements	Operational concern	Framework mechanism
Event-responsive operation	Continuous high-intensity processing is unnecessary during extended normal conditions	Normal, seismic-alert, and post-event operating modes
Data-quality assurance	Missing, saturated, corrupted, or nonphysical measurements may affect DT updating	Edge data-assurance engine
Temporal consistency	Packet disorder, timing mismatch, and heterogeneous sampling may compromise synchronization	Timestamp verification, buffering, and channel alignment
Communication-resilient operation	Exclusive reliance on remote cloud resources may delay time-critical processing	Edge–cloud task allocation
Physical–digital consistency	Credible measurements may disagree with the current DT state	Residual-based consistency monitoring
Controlled service release	Uncertain model outputs may otherwise appear authoritative	Confidence gate before downstream services
Protection against critical faults	A weighted confidence score may conceal a severe individual failure	Hard-constraint override
Decision traceability	Mode transitions and update decisions may be difficult to reconstruct	Data provenance, model and threshold versioning, diagnostic flags, and operator records

2.1 Layered architecture

The proposed confidence-gated seismic DT-driven CPS framework is composed of five functionally integrated layers that regulate the progression of information from structural sensing to decision-making support. Figure 1 illustrates the overall proposed framework. The physical layer contains the monitored structure, sensing network, data-acquisition setup, and any operational smart devices. Acquired measurements are transferred to the edge data layer, where timestamp validation, short-term buffering, packet-order verification, completeness assessment, channel synchronization, event detection, and hard safety screening are performed before the information is transferred to the digital environment. The DT layer subsequently analyzes the structural state, updates the digital representation, evaluates the residual between measured and predicted responses, and supports longer-term analytical functions. The confidence gate then formulates signal quality *Q(t)*, data completeness *P(t)*, synchronization *S(t)*, physical-digital consistency *M(t)*, and latency adequacy *L(t)*, together with the prescribed hard constraints, to classify each update as trusted, requiring engineering review, or fail-safe. Only updates that satisfy the confidence and authorization criteria are transferred to the service and governance layer for visualization, condition assessment, alert generation, engineering review, audit recording, and permitted operational actions. The feedback path is therefore governed by both confidence assessment and system authorization, preventing unverified digital-twin outputs from directly influencing the physical system.

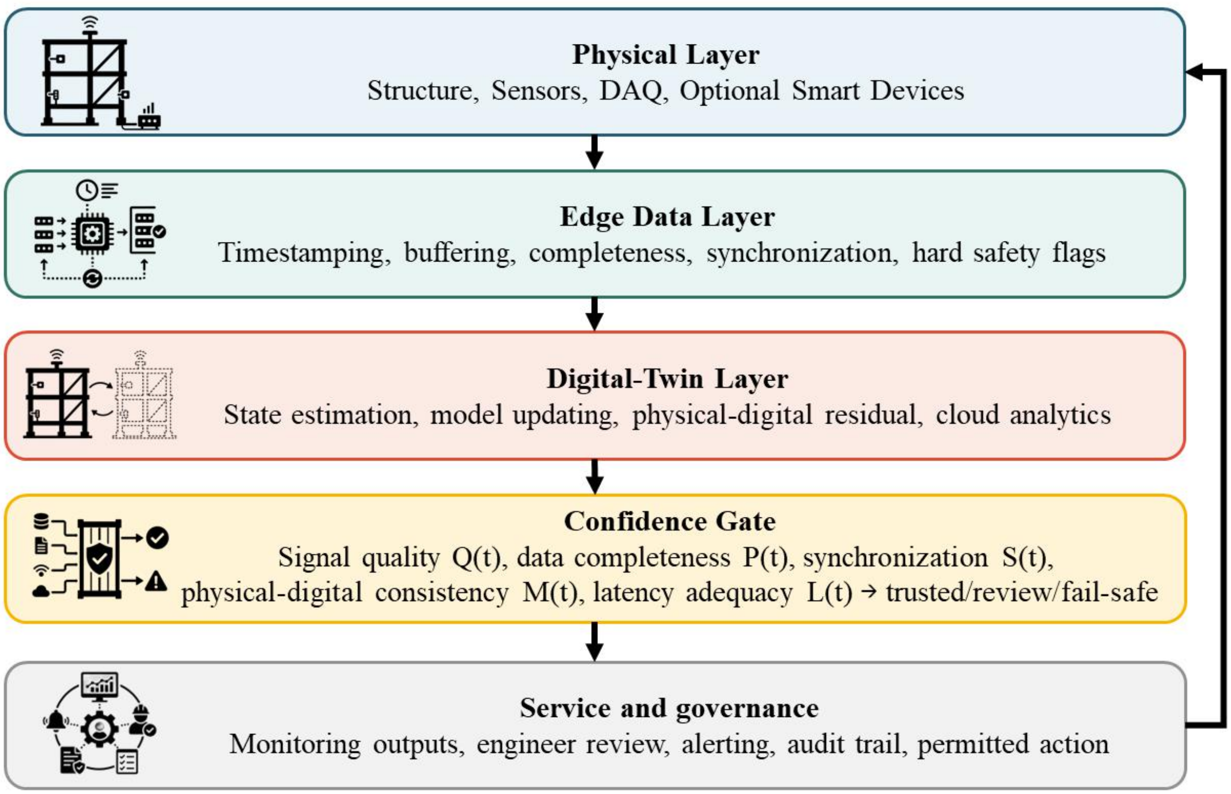

Figure 1. Proposed confidence-gated, event-triggered, edge-cloud DT-CPS framework

2.2 Event-triggered operational modes

Seismic monitoring is organized as a state-dependent process in which sensing, computation, and decision-making functions are involved over the earthquake sequence. Figure 2 illustrates that the framework distinguishes normal monitoring, seismic alert operation, and post-event analysis. The system ensures baseline synchronization, sensor-health surveillance, and low-rate analytical functions during normal conditions. A transition request is initiated when the edge data layer detects a configured event indicator and confirms that the trigger is supported by sufficient sensor channels without violating prescribed timing or data-quality constraints. Seismic-alert operation then increases acquisition priority, edge assurance, and the frequency of digital-twin state estimation. Following the termination of strong motion, the framework enters the post-event state for residual-condition assessment, model review, and inspection support. Normal operation is restored only after the assessment has been completed and a reliable baseline has been re-established.

Event-triggered mode changes are therefore not confined to a single architectural layer. The edge data layer computes event detection and preliminary trigger validation, the DT layer adapts its estimation and updating functions, and the service and governance layer records and manages the operational consequences of the transition. The confidence gate evaluates the reliability of the information and current DT state before the transition or associated outputs are accepted. Event detection identifies the need for a change in operation, whereas the confidence gate determines whether the available information is sufficiently trustworthy for that change to proceed. This separation prevents incomplete, corrupted, or desynchronized measurements from producing an unjustified mode transition or an unreliable structural assessment

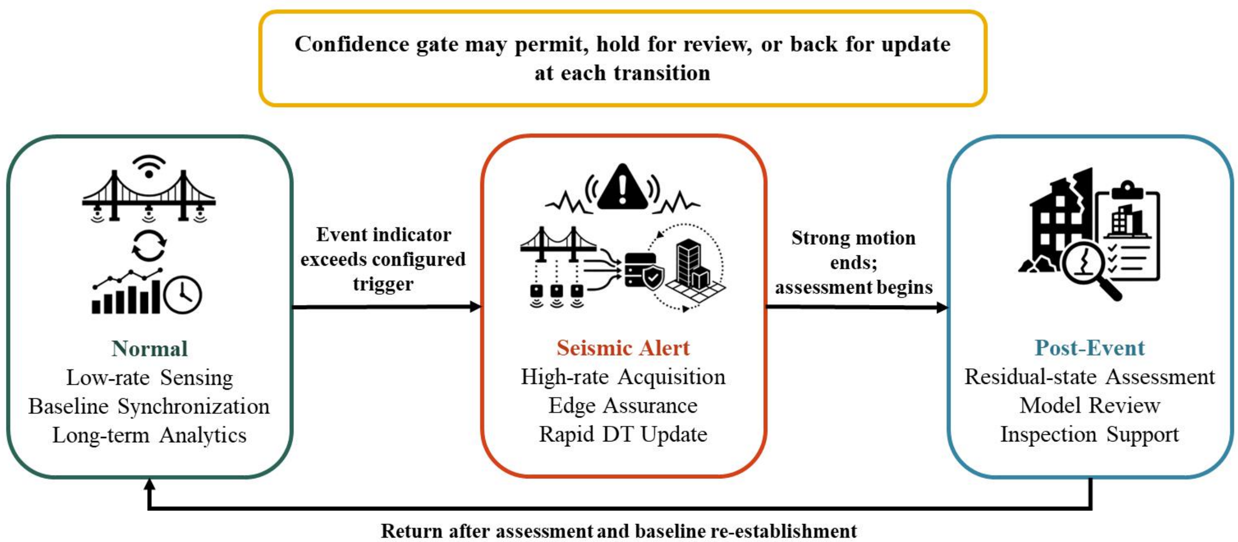

Figure 2. Event-triggered operating modes and transition logic

2.3 Edge-cloud task allocation

The allocation of functions between edge and DT/cloud resources is governed by timing criticality, communication dependence, computational demand, and the consequence of delayed execution. Operations requiring immediate and communication-resilient processing are performed at the edge, including timestamp verification, buffering, packet-order checking, data-quality screening, synchronization, event-trigger confirmation, and hard-constraint evaluation. Computationally intensive or less time-sensitive functions, such as high-fidelity state estimation, numerical simulation, model updating, cross-event analysis, persistent storage, and model-version management, are assigned to DT and cloud services. When rapid local estimation is necessary, a validated reduced-order model or computationally efficient surrogate can operate at the edge, whereas the high-fidelity DT performs detailed analysis and long-term historical evaluation. The resulting allocation is therefore not fixed, but may be adapted according to available hardware, network conditions, and the criticality of the intended service. The confidence gate is not assigned exclusively to either the edge or the cloud; it combines edge-derived data-assurance indicators with DT-derived model-consistency and latency information to determine whether an update is released, retained for engineering review, or rejected. Table 2 summarizes the corresponding allocation of functions between edge and DT/cloud resources.

Table 2. Functional allocation between edge and DT/cloud resources

Function	Edge responsibility	DT/cloud responsibility
Data ingestion	Timestamping, short-term buffering, packet-sequence verification, and sensor-status checking	Persistent storage, archival, and data-provenance management
Data assurance	assurance Completeness assessment, range and saturation checks, outlier screening, synchronization, and hard data flags	Long-term data-quality statistics, sensor-health trends, and recalibration support
Structural analysis	Rapid feature extraction and optional validated reduced-order inference	High-fidelity state estimation, simulation, model updating, and uncertainty analysis
Decision support	Local alert initiation and predefined fallback activation within authorized limits	Condition assessment, inspection prioritization, and maintenance support
Governance	Watchdog operation, local fail-safe logic, and cached permissions	Threshold and policy management, model versioning, audit records, and operator-action logging

2.4 Confidence index and decision states

The confidence gate evaluates the trustworthiness of each data-model update at the system level rather than representing the statistical uncertainty of an individual estimator. Five normalized component scores are considered: signal quality *Q(t)*, data completeness *P(t)*, synchronization *S(t)*, physical-digital consistency *M(t)*, and latency adequacy *L(t)*. Each index score ranges from 0 to 1, where higher values indicating better reliability conditions. A provisional composite confidence index is defined as:

$$C(t) = w_Q * Q(t) + w_P * P(t) + w_S * S(t) + w_M * M(t) + w_L * L(t) \tag{1}$$

$$w_Q + w_P + w_S + w_M + w_L = 1, w_i \geq 0 \tag{2}$$

Each component is evaluated for synchronized data block and normalized within range of 0 and 1. The signal quality assures compliance with measurement range, saturation, and outlier criteria. The completeness score defines the proportion of received samples relative to the expected samples. The synchronization score examines temporal alignment among sensing channels, while the physical-digital consistency score is evaluated from the normalized difference between measured and digital predicted responses. The latency-adequacy score computes the total acquisition, communication, and computational delay with the allowable latency limit. The specific normalization functions and limits must be calibrated for the monitored structure and intended applications.

The weighting coefficients and decision thresholds are structure-specific and should be calibrated according to the monitored structure, sensor network, DT model, and intended application. The weighted index is supplemented by a hard-constraint check to confirm that a critical failure is not masked by satisfactory values in other components. Hard-constraint violations may include the loss of essential sensing networks, missing data, model convergence failure, timestamp discrepancies exceeding the allowable tolerance, or applications beyond the validation domain of the DT. The hard-constraint indicator *H(t)* is assigned to 1 when all hard-constraints are satisfied and 0 when any hard-constraint is violated. There are two thresholds confirm the decision state in which τ_N for trusted operation and τ_F for fail-safe operation, with $\tau_N > \tau_F$. The state definition is:

$$D(t) = \begin{cases} Trusted,\ H(t) = 1\ and\ C(t) \geq \tau_N \\ Review,\ H(t) = 1\ and\ \tau_F < C(t) < \tau_N \\ Fail-safe,\ H(t) = 0\ and\ C(t) \leq \tau_F \end{cases} \quad (3)$$

Trusted updates are accepted and released downstream services. Updates assigned to the review state are withheld from automatic release and submitted for engineering assessment. Fail-safe are rejected or rolled back to the most recent accepted DT state, after which the prescribed fallback process is activated. Figure 3 illustrates the complete confidence-assessment and decision - making support.

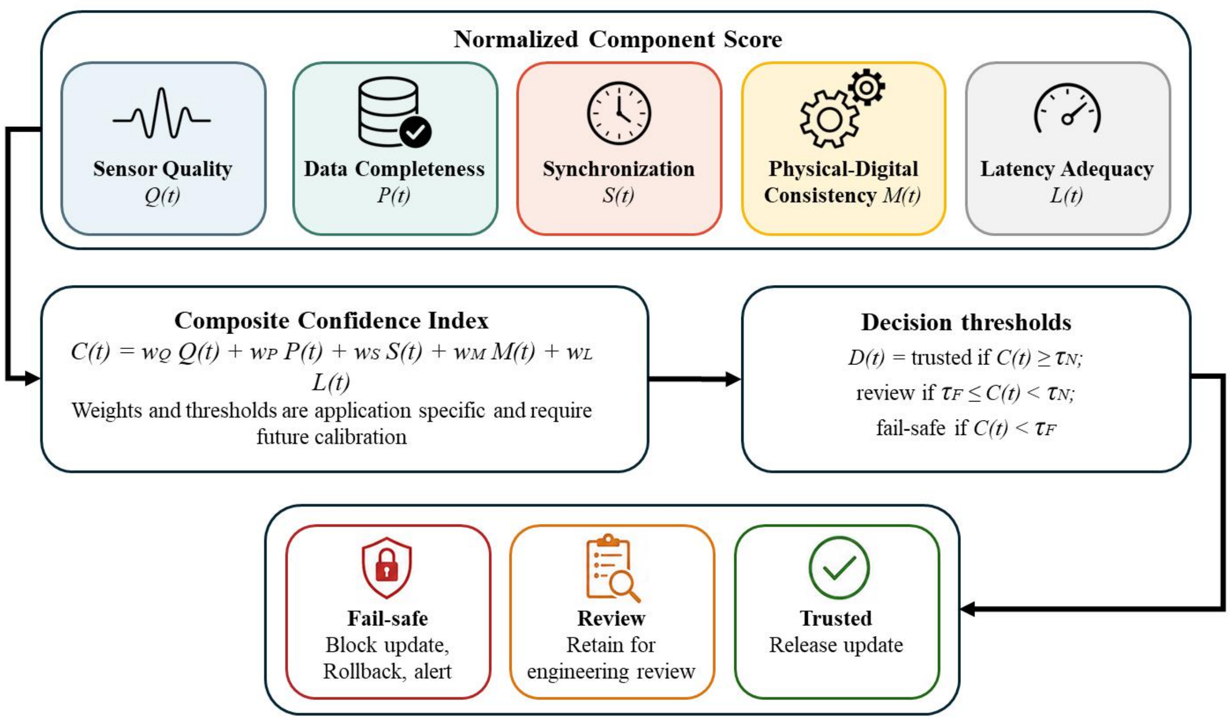

Figure 3. Confidence-gated decision logic for trusted, review, and fail-safe states

3. Computational workflow

The computational workflow follows a sequential update closed loop that transforms raw sensors data into confidence-labelled results. Each block of multi-sensor measurements is initially assigned a timestamp and packet identifier, along with the timing information needed for subsequent traceability. The edge-based assurance stage subsequently analyzes data completeness, measurement limits, sensor saturation, anomalous values, packet order, and channel condition. This assessment computes the signal quality score $Q(t)$, the completeness score $P(t)$, and any linked hard data flags. Information than passes these initial checks is then assigned to a shared time reference, from which the synchronization score $S(t)$ and the corresponding synchronized data block are obtained.

The synchronized data block is transferred to the DT service, where the structural state is computed and the corresponding responses are predicted. The difference between predicted and measured responses is used to compute the physical-digital consistency score $M(t)$. Meanwhile, timestamps linked with data acquisition, transmission, and computation are used to calculate the latency-adequacy score $L(t)$. The confidence gate integrates the five component scores, applies the defined decision thresholds, and confirms all hard constraints before identifying each update into one of the three decision conditions.

Updates classified as trusted are transferred to authorized structural monitoring and condition-assessment applications. Updates with moderate confidence are blocked from automatic release and are instead transferred for engineering review together with their confidence scores and diagnostic flags. Fail-safe updates are rejected or reverted to the latest approved state, followed by activation of the defined fallback procedure. Auditability is preserved throughout whole procedure by recording data provenance, operating model, individual component scores, threshold and model revisions, decision status, diagnostic flags, and any other subsequent action taken by the operator. These records allow every accepted, reviewed, or rejected update to be independently traced, recreated, and evaluated.

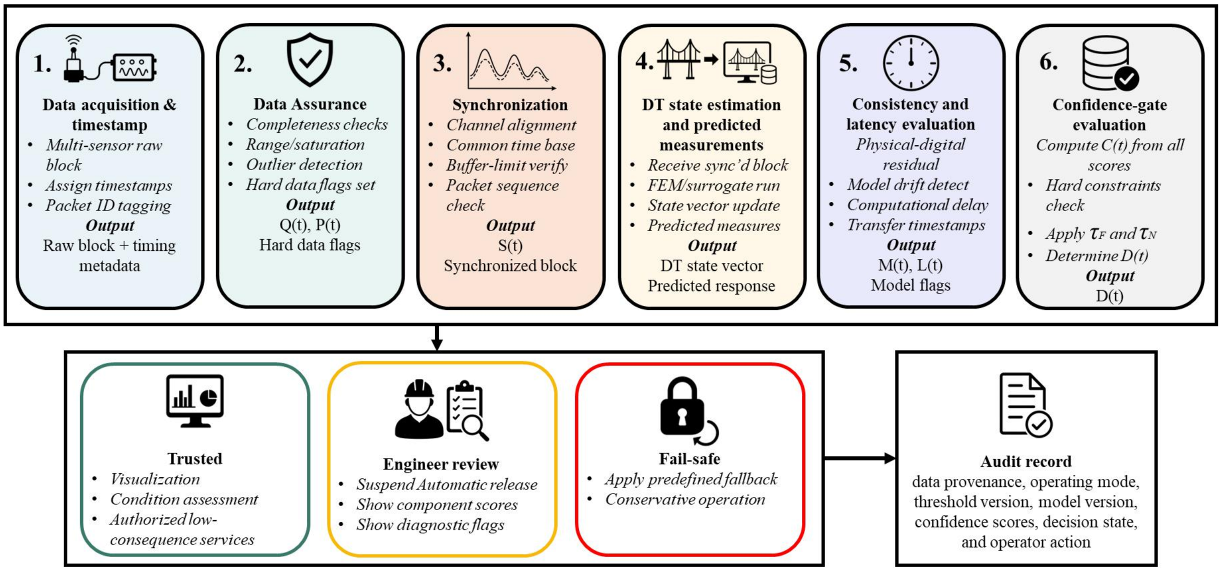

Figure 4. Algorithmic sequence for one update

4. Implementation pathways and future evaluation

The developed framework may be implemented in either an instrumented field structure or a real-time hybrid simulation (RTHS) platform. For field deployment, edge-processing functions can be linked into the local data acquisition system or monitoring gateway, while DT and cloud-based services perform structural-state estimation, model administration, and long-term assessment. The proposed confidence gate mechanism controls whether the resulting information is forwarded for visualization, condition assessment, or inspection support, thereby preventing the risk that incomplete or inconsistent information are regarded as dependable evidence of structural change.

RTHS offers a suitable controlled setup for the initial deployment of the proposed framework because physical data, digital models, timing records, and actuator interfaces are already integrated within a CPS testing system [11]. The developed workflow should initially be operated in shadow mode, where mode changes, confidence component scores, hard-constraint breaches, and decision status are logged without affecting the experiment. This whole setup allows the event logic, timing performance, physical-digital residuals, and fallback procedures to be analyzed before advisory outputs or automated permissions are activated. Advancement to higher levels of automation should take place only after the evidence needed at each previous stage has been established, as outlined in Table 3.

Table 3. Staged implementation and evidence required before progression

Stage	Primary activity	Required evidence
Offline replay	Evaluate the event-detection and confidence-assessment logic using archived data or deliberately degraded records	Reliable detection of delayed, missing, misaligned, saturated, and inconsistent data

Stage	Primary activity	Required evidence
Shadow DT	Execute the workflow influencing operation or testing	Consistent timing, stable residuals, and reproducible decisions
Advisory service	Provide confidence-labelled outputs to engineers	Decision agreement with engineering judgement and documented threshold refinement
Limited automation	Permit predefined low-consequence alerts or recommendations	Verified fallback performance, controlled false alarms, and independent safety review
Authorized closed loop	Enable validated feedback functions	System validation under representative loading, sensing, communication, and failure condition

5. Discussion

The primary contribution of the developed framework is the distinction between event recognition and the acceptance of DT updates. Event detection logic determines when the monitoring system should transition between operating modes, while the developed confidence gate evaluates whether the available data and model predictions are reliable enough for downstream operations. This distinction is particularly important during earthquake events, when increased sensing and computational demands may occur alongside missing data, sensor saturation, synchronization errors, communication latency, or inconsistencies between predicted and measured responses. By integrating component-level confidence measures with hard-constraint checks, the framework introduces an engineering-review state between automatic acceptance and full rejection. Consequently, uncertain cases can be examined without being interpreted either as verified structural change or as completely unusable information.

The framework supports monitoring, condition assessment, inspection services, alerts, and other authorized services, but does not validate autonomous structural control. Implementation therefore progresses from offline replay and shadow operations to advisory or limited automated operations. This staged process allows system logic, confidence scores, timing, fallback processes, and audit records to be analyzed without affecting the structure. Traceability is enabled by integrating each decision to its data source, confidence scores, thresholds, model revision, and operator actions. The framework has not been validated using experimental or field data, and its parameters need application-specific calibration. The additive confidence gate mechanism may also require more advanced formulations to capture dependencies among its components. Future studies should evaluate decision accuracy, robustness to degraded data, model drift, and fallback performance. Cybersecurity, standardization, cost, and regulatory approval remain beyond the present scope.

6. Conclusion

The study proposed a confidence-gated seismic DT-driven CPS framework for structural monitoring during normal operation, seismic alerts, and post-event assessment. The framework combines edge-level data quality assurance, coordinated work distribution between edge and DT/cloud resources, evaluation of physical-digital agreement, and confidence-based regulation of DT update release. Its primary contribution is the distinction between event identification and update acceptance, ensuring the system to classify updates as reliable, requiring engineering review, or requiring fail-safe operation. The workflow further confirms traceability by recording data provenance, threshold and model revisions, diagnostic indicators, and operator actions. As the framework is currently at the conceptual design stage, its confidence-components settings, state-transition rules, timing constraints, and fallback process must be calibrated and validated using field-monitoring data or RTHS before any automated feedback capability can be approved.

References

[1] Dong B, Shahbaz A, Karavasilis TL. Integration of cyber-physical systems and digital twins in structural engineering : Applications , challenges and future advancements. J Build Eng 2026;119:115259. https://doi.org/10.1016/j.jobe.2026.115259.

[2] Jiang F, Ma L, Broyd T, Chen K. Digital twin and its implementations in the civil engineering sector. Autom Constr 2021;130. https://doi.org/10.1016/j.autcon.2021.103838.

[3] Chiachío M, Megía M, Chiachío J, Fernandez J, Jalón ML. Structural digital twin framework: Formulation and technology integration. Autom Constr 2022;140. https://doi.org/10.1016/j.autcon.2022.104333.

[4] Doghri W, Saddoud A, Chaari Fourati L. Cyber-physical systems for structural health monitoring: sensing technologies and intelligent computing. J Supercomput 2022;78:766–809. https://doi.org/10.1007/s11227-021-03875-5.

[5] Hu X, Olgun G, Assaad RH. An intelligent BIM-enabled digital twin framework for real-time structural health monitoring using wireless IoT sensing, digital signal processing, and structural analysis. Expert Syst Appl 2024;252. https://doi.org/10.1016/j.eswa.2024.124204.

[6] Hackmann G, Guo W, Yan G, Sun Z, Lu C, Dyke S. Cyber-physical codesign of distributed structural health monitoring with wireless sensor networks. IEEE Trans Parallel Distrib Syst 2014;25:63–72. https://doi.org/10.1109/TPDS.2013.30.

[7] Aktan E, Bartoli I, Glišić B, Rainieri C. Lessons from Bridge Structural Health Monitoring (SHM) and Their Implications for the Development of Cyber-Physical Systems. Infrastructures 2024;9. https://doi.org/10.3390/infrastructures9020030.

[8] Angjeliu G, Coronelli D, Cardani G. Development of the simulation model for Digital Twin applications in historical masonry buildings: The integration between numerical and experimental reality. Comput Struct 2020;238. https://doi.org/10.1016/j.compstruc.2020.106282.

[9] Hielscher T, Khalil S, Virgona N, Hadigheh SA. A neural network based digital twin model for the structural health monitoring of reinforced concrete bridges. Structures 2023;57. https://doi.org/10.1016/j.istruc.2023.105248.

[10] Li X, Zhang FL, Xiang W, Liu WX, Fu SJ. Structural health monitoring system based on digital twins and real-time data-driven methods. Structures 2024;70. https://doi.org/10.1016/j.istruc.2024.107739.

[11] Zhang R, Phillips BM, Fernández-Cabán PL, Masters FJ. Cyber-physical structural optimization using real-time hybrid simulation. Eng Struct 2019;195:113–24. https://doi.org/10.1016/j.engstruct.2019.05.042.

Structural Damage Detection Based on Improved Noise Reduction Technique and Convolutional Neural Network

Tianlong Ouyang[1], Junfeng Dai[1], Shixing Liu[1], Jiqiao Zhang[1,*], Gongfa Chen[1,2], Fangsen Cui[3]

[1]School of Civil and Transportation Engineering, Guangdong University of Technology, Guangzhou, 510006, China
[2]Sino-French Institute, Dongguan University of Technology, Dongguan, 523808, China
[3]Institute of High Performance Computing (IHPC), Agency for Science, Technology and Research (A*STAR), Singapore 138632, Republic of Singapore

Abstract In the process of structural damage identification, the structural signals collected by sensors will inevitably be affected by noise generated from environmental and human factors. To prevent weak damage features from being submerged by external noise, enable convolutional neural network (CNN) to accurately extract key features, and improve the damage recognition rate, this study proposes a noise reduction method that combines complete ensemble empirical mode decomposition with adaptive noise (CEEMDAN) and an improved wavelet thresholding technique. The effectiveness and practicality of the proposed method are verified through numerical simulations and vibration experiments. The results indicate that the combination of CEEMDAN and the improved wavelet thresholding method yields the best denoising performance, effectively removing noise from structural signals. The average accuracy of CNN-based damage recognition exceeds 95%, which is significantly higher than the damage recognition accuracies obtained by using single denoising methods or CNN recognition without prior denoising.

Keywords: Structural damage detection, Vibration signal denoising, Empirical modal decomposition, Wavelet threshold decomposition, Convolutional neural network

1. Introduction

Due to the complexity of the engineering environment, in the actual process of structural damage detection (SDD), the vibration signals of the structure are easily affected by the noise brought by external factors. How to extract weak damage features and adopt effective means to denoise the acceleration signals so that the convolutional neural network (CNN) can quickly recognize and accurately localize them is one of the difficulties faced by current SDD technology[1].

Traditional SDD methods often struggle to meet the requirements of efficient, real-time, non-contact, and comprehensive monitoring. Vibration-based SDD methods have emerged and gradually become one of the core technologies for modern structural health monitoring (SHM). The occurrence of structural damage will change the physical properties of the structure, such as local stiffness, mass, and damping, which will lead to changes in the vibration characteristics of the structure (such as frequency[2], mode shapes[3][4], curvature[5], etc.) and vibration signals (acceleration signals[6], strain signals[7], displacement signals[8], etc.). The acceleration signal of the structure does not rely on the physical model of the structure and enable direct time-frequency analysis, retaining the most authentic structural vibration information and largely avoiding the problem of information loss caused by the modal analysis process.

In recent years, CNN has been proven to be a versatile and powerful tool. As a supervised multi-layer feed-forward artificial neural network, CNN leverages its powerful capability to not only learn feature-output associations, but also automate the entire feature extraction process. After appropriate training, direct mapping from the original input to the final output can be found. Its feature enables it to decompose complex tasks into smaller and simpler parts, thus performing well in complex tasks[9]. Zhan et al. investigated the noise immunity of CNNs and trained CNNs through the combined effect of structural parameter randomness and sampling noise, demonstrating that CNN has remarkable noise resistance[10]. Jamshidi et al. used a dataset consisting of the acceleration response of concrete beams under impact hammer tests to evaluate the accuracy of CNN classification, and the results showed that the CNN can successfully classify the severity of damage[11]. Teng et al. illustrated the process of CNN feature extraction in the detection of defects on the surface of structures[12]. Yang et al. jointly constructed a network model with CNN and LSTM, and performed SDD on a steel bridge structure downsizing model under different working conditions, which verified the advantages of the method in terms of accuracy and precision[13]. The above results all illustrate that CNN has good damage detection performance.

Regardless of the SDD method employed, the identification process is often affected by human errors and environmental variations, which introduce high-frequency white noise into the output acceleration signals. During CNN training, noise-contaminated data not only reduces training efficiency but also results in incorrect learning, ultimately decreasing the SDD accuracy. As a novel signal processing method, empirical mode decomposition (EMD) was first proposed by Huang et al.[14] in 1998. Since its introduction, it has attracted the attention of numerous scholars at home and abroad, and its applications in the field of SDD have gradually increased. Pines et al. decomposed the time-series model of one-dimensional structures using the EMD method to obtain modal information such as damping and phase, thereby determining the presence, location, and severity of structural damage[15]. To address the issue of noise interference in sampling signals for bridge health monitoring, Yan employed a denoising algorithm combining EMD with wavelet transform[16]. Through comparative numerical simulation and finite element simulation tests, the effectiveness and practicality of this method were verified. Deering et al. homogenized the distribution of extreme points in the original signal by adding a masking signal, thereby suppressing mode mixing[17]. Wu et al. improved the EMD and proposed the ensemble empirical mode decomposition (EEMD)[18]. Then Yeh et al. [19] proposed complementary ensemble empirical mode decomposition (CEEMD), which reduced reconstruction errors caused by white noise while maintaining decomposition effects similar to EEMD by adding white noise with opposite signs to the original signal, performing EMD on the two signals separately, and then calculating the mean value. However, both EEMD and CEEMD suffer from the common drawback of heavy computational load[20]. Based on the theoretical framework of EMD, Torres et al.[21] proposed complete ensemble empirical mode decomposition with adaptive noise (CEEMDAN) by injecting Gaussian white noise into the signal, performing multiple decompositions, and integrating and averaging the decomposition results, drawing on the method of EEMD. Dai et al.[22] systematically reviewed the research progress of EMD in the fields of one-dimensional and multi-dimensional signal analysis. Through a comparative analysis of EMD, EEMD, and CEEMDAN, they revealed the following key advantages. CEEMDAN adopts an adaptive white noise injection strategy, adding Gaussian white noise at each modal decomposition stage in a decreasing proportion of the hierarchical structure. This significantly reduces the noise residue in the intrinsic mode functions (IMFs). Meanwhile, by introducing a global iteration termination criterion, the decomposition efficiency of CEEMDAN is improved by approximately 50% compared with traditional methods, while ensuring the reconstruction accuracy of the signals. Aiming at the severe noise problem in bridge vibration signals under complex environments, He et al.[23] denoised the original signals by combining CEEMDAN with permutation entropy, solving the problems of mode mixing and endpoint effects, and verifying the superiority and application value of this method through vibration signal analysis of actual long-span bridge structures. Liu et al. developed a joint denoising method based on CEEMDAN and multiscale permutation entropy for flow-releasing structures[24]. This method improves the signal denoising effect and can accurately remove noise from the vibration signals of flow-releasing guide walls. Compared with the method proposed by He et al., it demonstrates greater engineering application value in terms of complex noise suppression, real-time performance, and scene adaptability. Although CEEMDAN shows significant advantages in non-stationary signal processing, its algorithm still has several problems that need to be solved[25]. Empirical evidence indicates that residual noise remains in the intrinsic mode functions (IMFs) derived from CEEMDAN, particularly within the high-frequency components of the signal. This residual noise can lead to spurious frequency modulation artifacts during Hilbert spectral analysis. Furthermore, in the initial stages of decomposition, the algorithm is susceptible to the stochastic nature of the white-noise-assisted process, resulting in unphysical and excessive decomposition modes.

Wavelet decomposition (WD) is a denoising method based on the wavelet transform theory. Zhou et al.[26] proposed an adaptive threshold algorithm combined with an improved threshold function to track noise, and verified the effectiveness of this method through simulation experiments. Sha[27] proposed a 1/2 threshold method, simulation experiments and engineering examples with deformation monitoring signals, compared the effectiveness of this method with soft and hard thresholding methods, and proved that this method is more effective. Li et al.[28] adopted an improved wavelet threshold joint noise reduction method, which effectively extracted the structural vibration information of the guide wall and well filtered out low-frequency water flow noise and part of high-frequency white noise. Although wavelet threshold noise reduction has good time-frequency characteristics and signal decomposition ability, it is interfered by many influencing factors, such as the number of wavelet decomposition layers[29], denoising evaluation[30][31], and threshold function. Generally, it is difficult to select appropriate parameters manually. For example, in the threshold algorithm proposed by Gan et al.[32], the estimated threshold of the first layer is too large, which is likely to cause the phenomenon of "over-suppressing" wavelet coefficients. Since different signals exhibit distinct characteristics, threshold parameters often require targeted resetting and adjustment, which not only reduces computational efficiency but also impedes satisfactory outcomes. This study first optimizes the correlation coefficient method of CEEMDAN by introducing an adaptive threshold factor based on the improved wavelet thresholding method, enabling the algorithm to autonomously adapt to diverse signals for optimal results. Subsequently, a denoising approach integrating CEEMDAN and improved wavelet thresholding is proposed. The IMF components decomposed by CEEMDAN are classified into high-frequency and low-frequency modal categories, and the improved wavelet thresholding method is jointly applied to decompose and reconstruct high-frequency components, further suppressing noise interference. Finally, CNNs are employed to perform damage identification and localization on denoised signals from numerical experiments and vibration experiments. It is demonstrated that this method significantly enhances the training efficiency and recognition accuracy of CNN, exhibits excellent denoising performance and universality, and can effectively reduce high-frequency noise interference in structural signals.

2. Methods

2.1 CEEMDAN

The core idea of CEEMDAN is based on the EMD theory, adopting a strategy of adaptive noise injection and recursive decomposition. It draws on the approach of the EEMD, which involves injecting Gaussian white noise into the signal, performing multiple decompositions, then integrating the decomposition results and calculating their average. This not only ensured the quality of decomposition but also significantly improves computational efficiency. Its decomposition process is as follows:

(1) Adaptive noise is introduced into the original signal $r_0(t) = s(t)$ to suppress mode mixing by destroying the intrinsic scale of the signal through dynamic noise perturbation. Its formula is as follows:

$$\varepsilon_{k-1} = \frac{\varepsilon_0}{\sqrt{k}} \tag{1}$$

where ε_0 is the noise amplitude and k is the decomposition order.

(2) Positive and negative noise pairs are introduced to ensure that the noise is completely canceled out.

$$r_{k-1}^{(i,\pm)}(t) = r_{k-1}(t) \pm \varepsilon_{k-1}\omega_i(t) \tag{2}$$

(3) Each noise-added signal is subjected to one EMD sieving to extract the first-order IMF.

$$\mathrm{IMF}_k^{(i,\pm)}(t) = \mathrm{EMD}_1\left(r_{k-1}^{(i,\pm)}(t)\right) \tag{3}$$

(4) Statistical averaging calculations are conducted to eliminate the effects of random noise.

$$\mathrm{IMF}_k(t) = \frac{1}{2M}\sum_{i=1}^{M}\left[\mathrm{IMF}_k^{(i,+)}(t) + \mathrm{IMF}_k^{(i,-)}(t)\right] \tag{4}$$

(5) The extracted IMFs are stripped layer by layer to gradually approximate the overall trend or residual noise of the signal.

$$r_k(t) = r_{k-1}(t) - \mathrm{IMF}_k(t) \tag{5}$$

The above steps are repeated until the residual signal is monotonic (the number of extreme points is no more than 2). At this point, it is indicated that no further oscillatory modes could be decomposed, and finally k-th IMFs are obtained. The decomposition flowchart is shown in Figure 1.

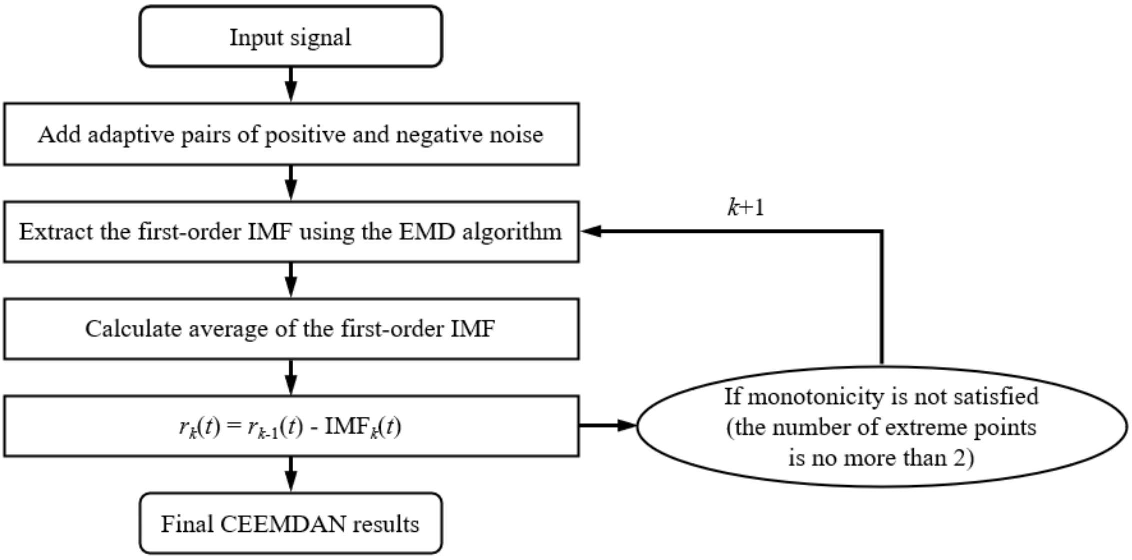

Figure 1 Flowchart of CEEMDAN.

CEEMDAN symmetrically injected pairs of positive and negative noise, and gradually reduces the noise amplitude corresponding to high-frequency IMF components. This mechanism effectively suppressed noise interference in high-frequency components while ensuring the purity of low-frequency modes. Meanwhile, in each decomposition stage, only the first-order IMF is extracted from the current residual signal, avoiding repeated EMD of the entire signal. This method significantly improves computational efficiency and result consistency while ensuring the quality of decomposition.

After applying the CEEMDAN, multiple IMFs are generated, and some of these components still contained noise or redundant information. Therefore, it is necessary to screen out the effective modes. Traditional screening methods relied on manual experience to select IMFs, which is subjective and inefficient. The Pearson correlation coefficient (PCC) method is a statistical index used to measure the linear relationship between two continuous variables. Its value ranged from -1 to 1, and it could be used to assess the linear correlation between two variables and the direction of the correlation. Its calculation formula is as follows:

$$\rho_k = \frac{\sum_{t=1}^{N}[s(t)-\bar{s}][c_k(t)-\bar{c}_k]}{\sqrt{\sum_{t=1}^{N}[s(t)-\bar{s}]^2}\sqrt{\sum_{t=1}^{N}[c_k(t)-\bar{c}_k]^2}} \tag{6}$$

where $s(t)$ is the original signal, $c_k(t)$ is the k-th IMF, ρ_k is the correlation coefficient value of the k-th IMF. The closer the value of the correlation coefficient is to 0, the lower the similarity between the original signal and the IMF, and the weaker the correlation between them.

To enhance the reliability of the decomposition results and objectively select effective modes, a threshold criterion is introduced into the IMFs obtained from CEEMDAN[33], to distinguish between effective modes and noise modes. Additionally, the gradient calculation is optimized to automatically find the optimal solution for the threshold, which served as the final threshold for screening. The decomposition process is as follows:

(1) Introduction of a standardized formula for thresholds:

$$\lambda = \frac{\max(\rho_k)}{10 \times \max(\rho_k) - 3} \tag{7}$$

where the IMF is judged to be a valid mode when $\rho_k > \lambda$, and a noise mode when $\rho_k < \lambda$.

(2) Using Python's loop computation script, the gradient is computed in the interval $[0.1, \lambda]$ with 0.01 as the step size, generating a new series of thresholds β. A series of decompositions are obtained by using the thresholds as filtering conditions.

(3) The signal to noise ratio (SNR) and root mean squared error (RMSE) are used as evaluation metrics[34] to assess the decomposition results after each calculation, and the decomposition result with the highest SNR and the smallest RMSE is selected. The corresponding threshold at this point is the optimal threshold, as shown below. The SNR is a classical measure of denoising effect. It represented the relative strength of the signal compared to the noise. The higher the SNR is, the better the denoising effect is. On the other hand, the RMSE is used to measure the difference between the denoised signal and the original signal. The smaller the RMSE is, the better the denoising performance is.

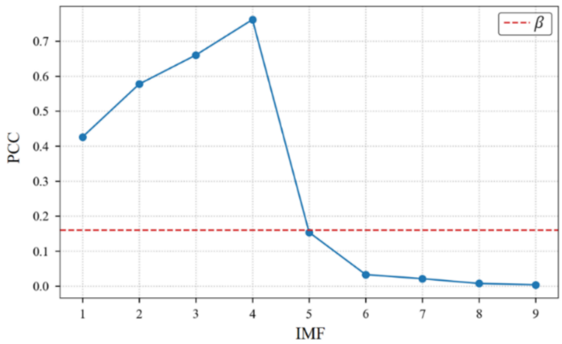

Figure 2 Correlation coefficient values for each order of IMF.

2.2 Wavelet Improved Threshold Decomposition

Wavelet threshold decomposition is a denoising method established on the basis of wavelet transform theory, which is characterized by multi-scale and decorrelation. Although wavelet threshold decomposition had good time-frequency analysis and signal decomposition ability, it is easily interfered by many influencing factors, such as the number of wavelet decomposition layers, denoising evaluation, threshold function and so on. Among them, the selection of threshold parameters, as a crucial step in wavelet threshold decomposition, directly affected the denoising effect. A threshold that is too high might lead to signal loss, while a threshold that is too low failed to effectively remove noise. Manual selection often involved the dilemma of striking a balance between preserving signal features and suppressing noise, making it generally difficult to obtain appropriate parameters.

Conventional threshold functions primarily include the hard thresholding method and the soft thresholding method as shown in Equations (8) and (9). The hard thresholding method is widely used due to its simple and straightforward processing. However, it had the problem of "one-size-fits-all", and there is a discontinuous jump at the threshold value when $|x| = \lambda$, lacking smoothness. The soft thresholding method, by introducing a smoothing coefficient, could generate continuous signals and reduce the oscillation of the reconstructed signals. Nevertheless, it also suffered from the issue of constant deviation, which led to the loss of some important features of the signals. Hard threshold expression:

$$\hat{d}_{j,k} = \begin{cases} d_{j,k}, & |d_{j,k}| \geq \lambda \\ 0, & |d_{j,k}| < \lambda \end{cases} \tag{8}$$

Soft threshold expression:

$$\hat{d}_{j,k} = \begin{cases} \text{sign}(d_{j,k})(\,|d_{j,k}| - \lambda), & |d_{j,k}| \geq \lambda \\ 0, & |d_{j,k}| < \lambda \end{cases} \tag{9}$$

where $d_{j,k}$ is the wavelet detail coefficient, which contained the detail and noise of the signal; and λ is the threshold.

In order to solve the above problems, this study proposed a modified wavelet thresholding function incorporating Heursure's adaptive selection principle[35]. The improved threshold expression is as follows.

$$\hat{d}_{j,k} = \begin{cases} ud_{j,k} + (1-u)\text{sign}\big(d_{j,k}\big)\{|d_{j,k}| - \dfrac{\lambda}{\log_2\left[2 + t\big(|d_{j,k}| - \lambda\big)\right]}\}, & |d_{j,k}| \geq \lambda \\ 0, & |d_{j,k}| < \lambda \end{cases} \tag{10}$$

where $u = \frac{2}{\pi}\arctan(t(|d_{j,k}| - \lambda)^2)$, $t \geq 0$. When $t = 0$, the value of $\hat{d}_{j,k}$ is the soft threshold, and when $t \to \infty$, the value of $\hat{d}_{j,k}$ is the hard threshold. The comparison of the improved wavelet threshold with the soft and hard thresholds is shown in Figure 3.

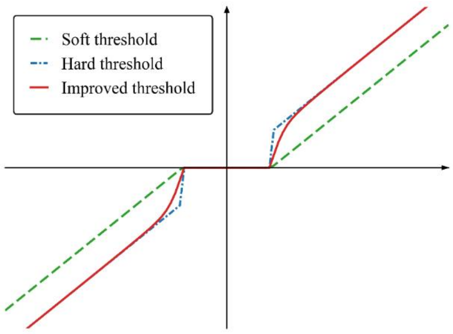

Figure 3 Comparison of improved threshold, soft threshold and hard threshold.

In this study, the adjustment factor t is introduced to realize the change of function radian by changing the size of t (as in Figure 4), and Python is used to increase the gradient calculation and comparison function to make it adaptive for different signals to get the optimal result.

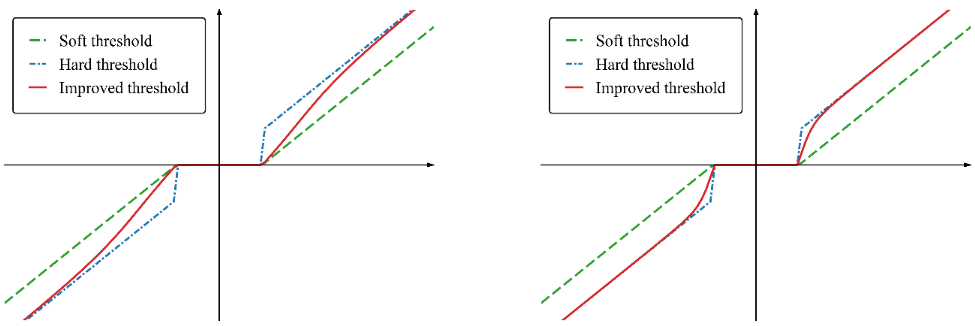

(a) *t*=0.5 (b) *t*=10

Figure 4 Threshold functions for different moderators.

From the figure, it could be seen that the improved threshold avoided the jump discontinuity phenomenon of the hard threshold and reduced the constant error existing in the soft threshold, which could better reflect the real characteristics of the signal while retaining the advantages of both.

2.3 Improved noise reduction methods

CEEMDAN yields useful IMFs, yet noise-dominated components (e.g., red-marked in Figure 5) may retain critical features. Therefore, in order to further improve the signal-to-noise ratio, it is necessary to carry out the secondary noise reduction process for these noise-containing high-frequency components, and this paper proposed a method combining CEEMDAN with improved wavelet thresholding for joint denoising of the signal.

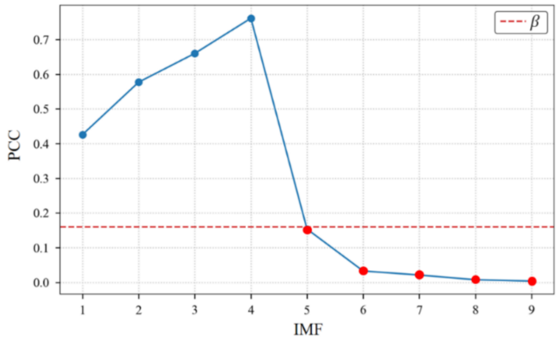

Figure 5 Noisy high-frequency components.

Firstly, the original signal is preliminarily decomposed by CEEMDAN. Then, vector screening is carried out using the optimized correlation coefficient algorithm to distinguish useful IMFs from noisy IMFs, and the useful IMFs are retained. Secondly, the noisy IMFs are subjected to noise reduction again using the improved wavelet thresholding method, and then reconstructed through wavelet inversion to obtain the denoised noisy IMFs. Finally, the noise reduction signal is obtained by reconstructing the useful IMFs and the denoised noisy IMFs. The decomposition flowchart is shown as Figure 6.

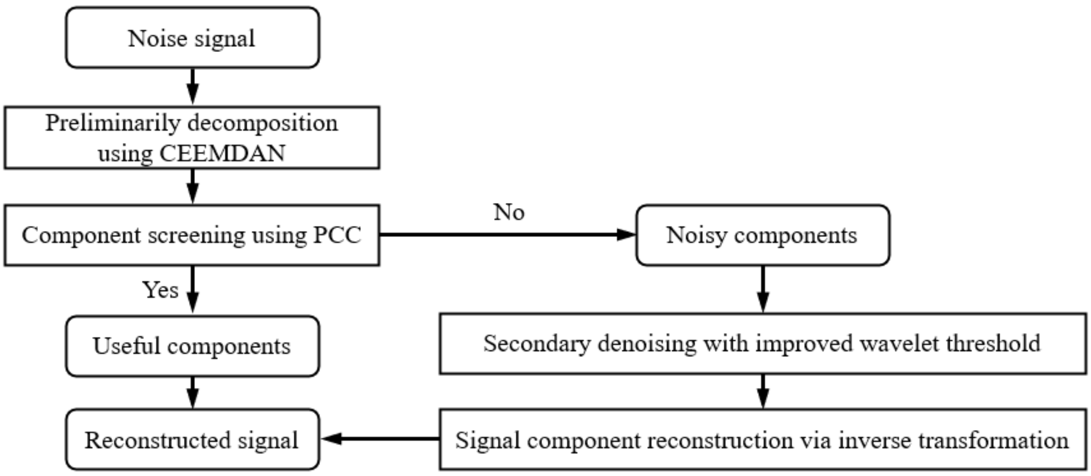

Figure 6 Process of improved denoising methods.

2.4 Input to CNN

In this study, the CNN is constructed based on the Matlab platform. The Adam optimizer is employed to enhance the adaptability of the network, and the nonlinearity is strengthened through the ReLU activation layer. Firstly, the acceleration signals of the structure are used as input data. Taking the beam structure in Figure 7 as an example, three acceleration sensors (marked by red five-pointed stars in the figure) are utilized to collect data. Each sensor obtained 1,000 data points. Then, the data from the three sensors are stored as a 1,000×3 text data, which is regarded as a matrix and served as the input of the CNN, with the number of rows being 1,000 and the number of columns being 3. The output result of a CNN classification task is usually a category label, such as the probability of category A or B. Therefore, it is necessary to preset the number of categories according to the working conditions and number the different working conditions in the construction of CNN. Suppose the three crack damage conditions with different locations are numbered as 1, 2, and 3. Then when the network output result is 1, it meant that there is damage at the location of 1, and when the output result is 2, it meant that there is damage at the location of 2, and so on.

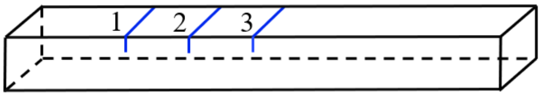

Figure 7 Beams.

3. Numerical experiment

To validate the effectiveness of the improved denoising method, simulations are conducted using noise-contaminated signals. First, the denoising effects of EMD, EEMD, and CEEMDAN algorithms are individually analyzed, comparing their performance differences. Second, wavelet hard thresholding, soft thresholding, and improved wavelet thresholding algorithms are separately investigated, with the superiority of the improved thresholding method verified through evaluation metrics. Finally, cross-combination experiments are performed on these two categories of algorithms, confirming the comprehensive advantages of CEEMDAN combined with improved wavelet thresholding. In practical engineering, the vibration subjected to structures is typically multimodal, with distinct frequencies across different modes. Therefore, this section superimposed multiple cosine waves with varying frequencies and amplitudes, adding Gaussian white noise to simulate complex noise interference in real-world environments. Synthetic noisy signals are generated using:

$$\begin{cases} X_1(t) = 5e^{(-t/2)} \cdot \cos(16t) \\ X_2(t) = 2e^{(-t/2)} \cdot \cos(50t) \\ X_3(t) = 2e^{(-t/2)} \cdot \cos(100t) \\ f(t) = X_1(t) + X_2(t) + X_3(t) + \eta \end{cases} \tag{11}$$

The frequencies of the three signals are 16 Hz, 50 Hz, and 100 Hz, respectively. By adding Gaussian white noise with a magnitude of 10 dB, the signal-to-noise ratio is incorporated into the synthesized signal. The noisy signal η is shown in the figure below.

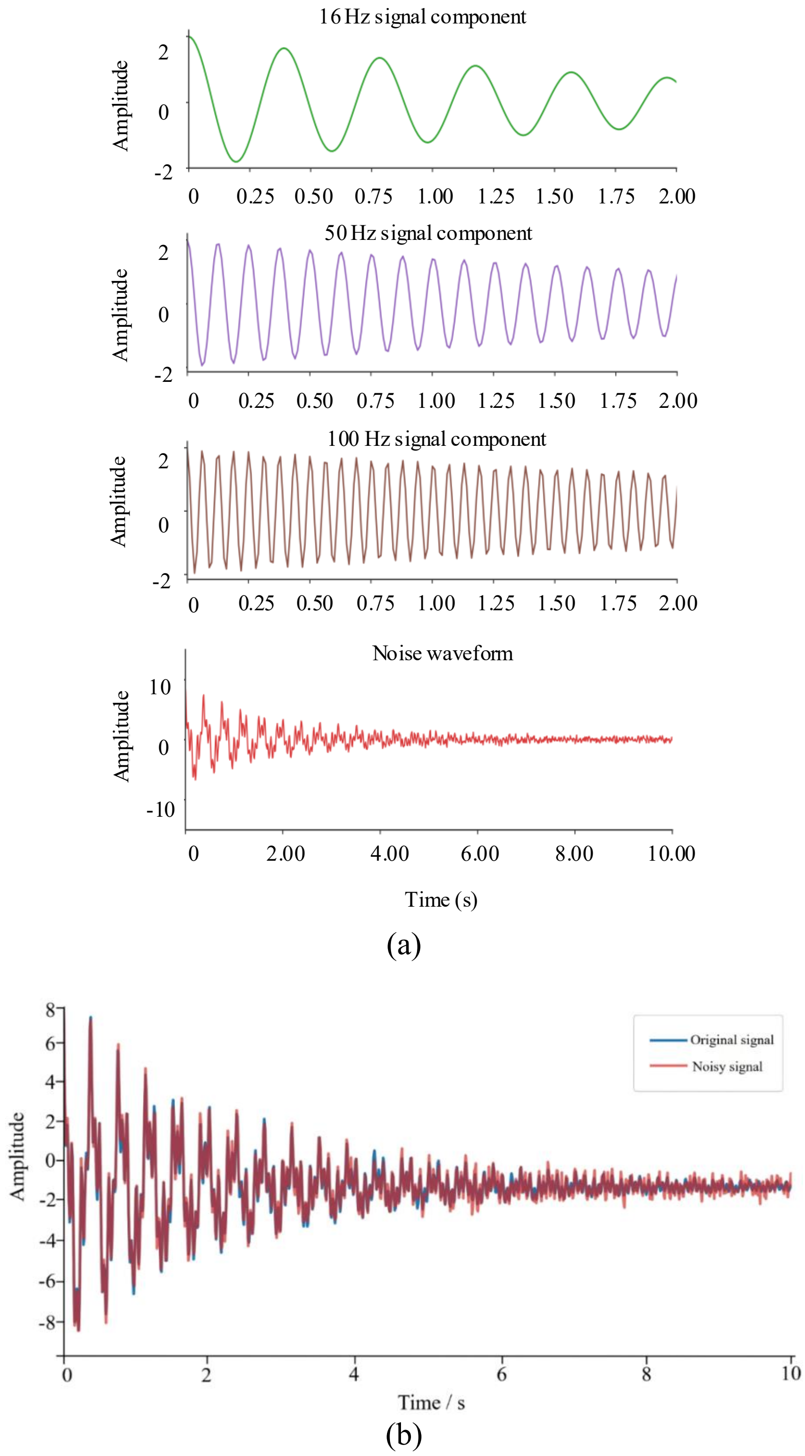

Figure 8 Analog signal with noise: (a) Signal component waveform; (b) Comparison of noisy signal and original signal.

Firstly, EMD, EEMD, CEEMDAN are performed on the noise-containing signal, and the decomposition results are shown in Figure 9.

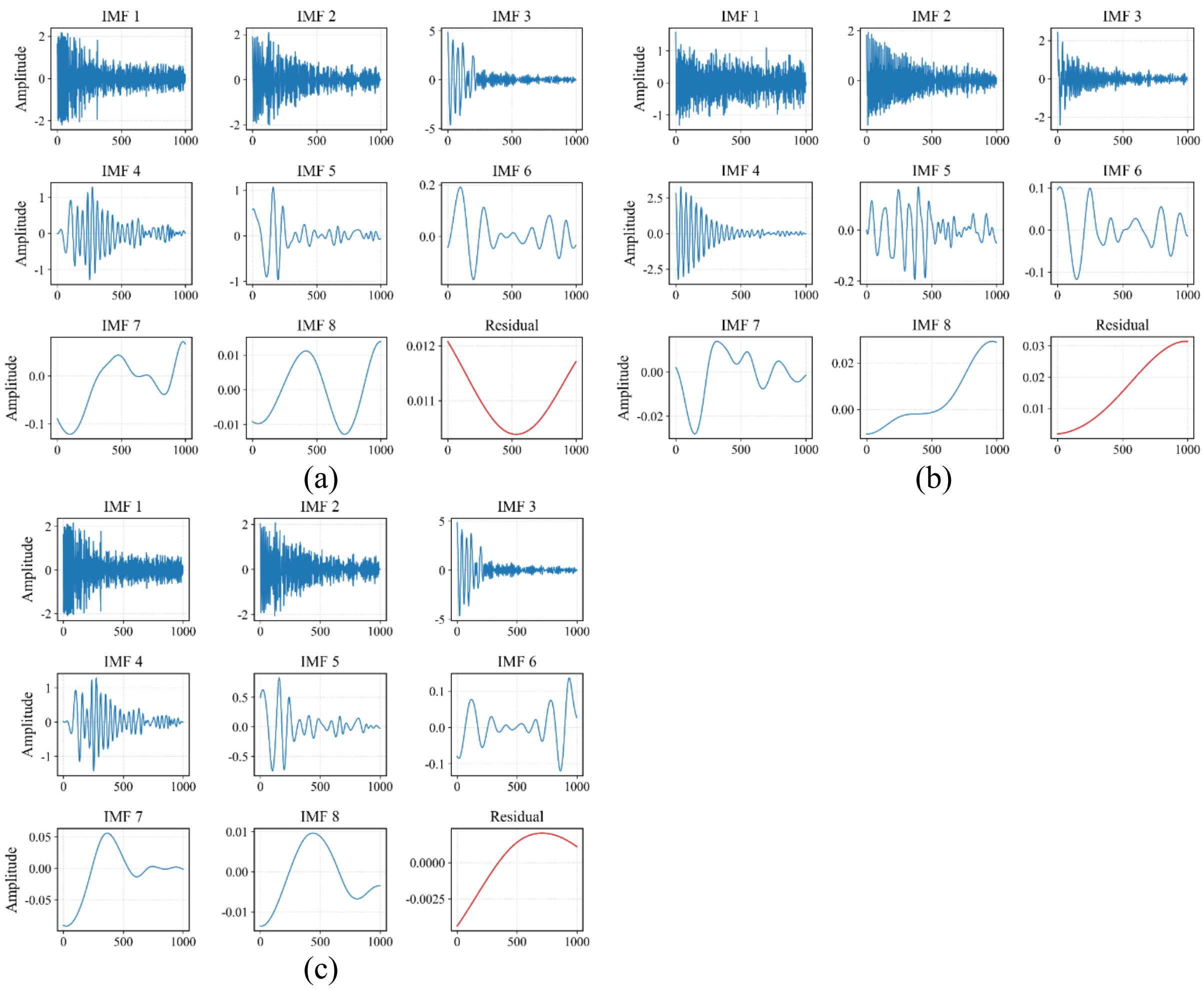

Figure 9 (a) EMD; (b) EEMD; (c) CEEMDAN.

According to the optimized correlation coefficient method described in section 2.1, combined with the loop calculation function of Python, the optimal threshold value for each decomposition method is determined. Subsequently, the IMFs obtained from the decomposition are screened using the threshold β as a criterion to distinguish between low-frequency useful components and high-frequency noise-containing components. The optimal thresholds of the three decomposition methods are shown in Figure 10, from which the correlation coefficients between the IMFs decomposed by each decomposition method and the original signal could be clearly seen.

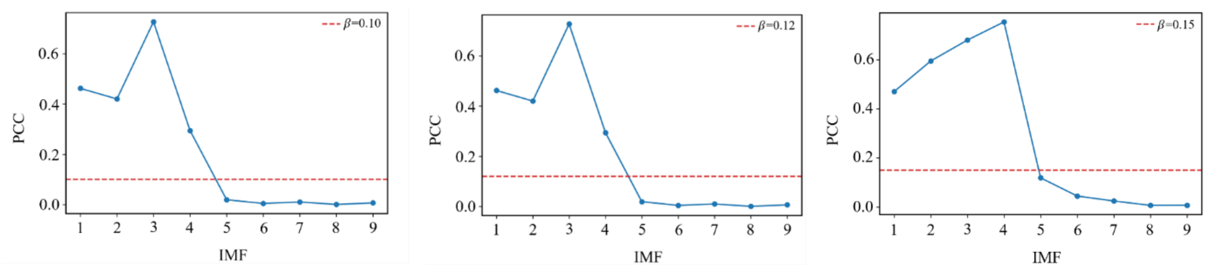

(a) (b) (c)

Figure 10 Selection of the effective IMF: (a) β=0.10; (b) β=0.12; (c) β=0.15.

As could be seen from the Figure 10, the first four IMFs of each graph are larger than the threshold β. Therefore, all three decomposition methods had obtained four useful components, and the useful components of the three methods are reconstructed separately to obtain the denoised signal.

To compare the denoising effects of the three methods, SNR and RMSE are adopted as evaluation metrics. Specifically, SNR reflects the noise level in the reconstructed signal, while RMSE quantifies the error magnitude between the original and reconstructed signals. A higher SNR indicates a greater signal-to-noise ratio in the reconstructed signal, implying less noise contamination and clearer signal characteristics. A lower RMSE signifies a smaller deviation between the reconstructed and original signals, better preserving the intrinsic features of the source signal. As shown in Table 1, the CEEMDAN method achieved the highest SNR (21.66 dB) and lowest RMSE (0.0212 cm), demonstrating its superiority over EMD and EEMD in attaining enhanced denoising performance.

Table 1 Evaluation results using SNR and RMSE.

Decomposition methods / Evaluation metrics	EMD	EEMD	CEEMDAN
SNR (dB)	13.729	16.655	22.825
RMSE	0.307	0.22	0.11

Before validating the wavelet improvement thresholding method, the foundation parameters needed to be set. Daubechies (db) wavelet and Symlet (Sym) wavelet had significant advantages in non-smooth signals and vibration signals due to high vanishing moments and approximate symmetry. Therefore, based on the rule of thumb, db 1 ~ 8 and Sym 1 ~ 8 are selected as the wavelet bases, the number of decomposition layers are 1 ~ 5, and wavelet threshold denoising test is performed using wavelet soft threshold and hard threshold as the threshold function.

A cross-validation approach is employed for different wavelet bases and decomposition levels. For each combination, ten wavelet decompositions are performed to generate ten evaluation results. These results are then averaged, and the mean value served as the final outcome for that specific combination. Irrespective of whether the wavelet hard threshold or soft threshold method is used, the SNR reached its minimum and the RMSE attained its maximum when the wavelet base is db8 and the decomposition level is 3. Therefore, the wavelet basis of db8 and the number of decomposition layers of 3 are chosen as the base parameters for the subsequent decomposition.

In the noise reduction process based on the wavelet improvement threshold, the key is the setting of the tuning factor t. Therefore, the wavelet decomposition of the noise-containing signal is next performed at different values of t to obtain the optimal values of SNR and RMSE, and the results are shown in Figure 11, with t ranging from [0, 10].

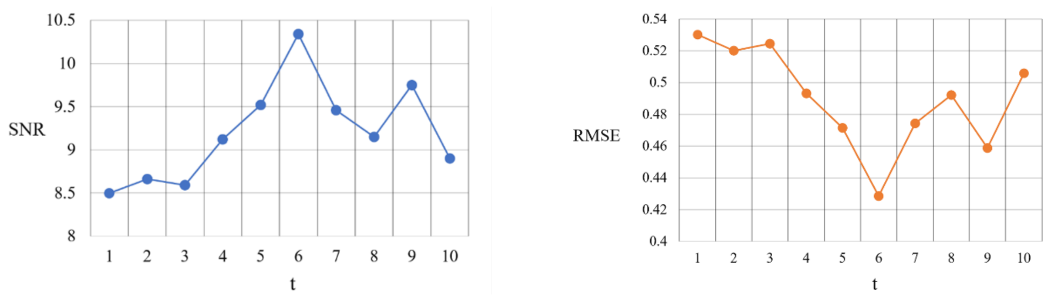

Figure 11 Evaluation results using wavelet improvement threshold: (a) SNRs corresponding to different regulators t; (b) RMSE corresponding to different regulators t.

From the results in Figure 11, it could be seen that the maximum value of the SNR is 10.34 dB, and the minimum value of the RMSE is 0.4285. These two values correspond to the results when t = 6. Therefore, when the adjustment factor t is 6, the corresponding wavelet threshold decomposition result is optimal, and the value of t at this time is the optimal adjustment factor.

In order to further enhance the denoising effect, this study proposed an improved noise reduction method based on CEEMDAN combined with wavelet improved thresholding method, which performed secondary denoising on the signal by combining the advantages of both. The results of combining EMD, EEMD, CEEMDAN with wavelet hard threshold, soft threshold and wavelet improved threshold and cross-validation are shown in Table 2, where wavelet hard threshold, soft threshold and improved threshold are represented by hard, soft and improved respectively. It could be seen by comparison that for any class of modal decomposition methods, the performance of the joint noise reduction method is better than that of the single noise reduction method, and the combined wavelet improved threshold method is the best, the combined wavelet hard threshold method is the second best, and the combined wavelet soft threshold method is the second best. Meanwhile, whether using a single empirical modal decomposition method or combining the wavelet thresholding algorithm, the results of EMD, EEMD, and CEEMDAN showed a gradual increasing trend. Notably, the CEEMDAN-wavelet improved thresholding hybrid achieved the peak SNR value (30.959 dB) and the lowest RMSE (0.042), indicating its superior noise suppression capability.

Table 2 Cross-validation results.

	EMD	EEMD	CEEMDAN
SNR (dB)	13.729	16.655	22.825
RMSE	0.307	0.22	0.11
	EMD+soft	EEMD+soft	CEEMDAN+soft
SNR (dB)	23.902	25.097	27.686
RMSE	0.096	0.083	0.062
	EMD+hard	EEMD+hard	CEEMDAN+hard
SNR (dB)	27.229	28.475	28.935
RMSE	0.065	0.058	0.053
	EMD+improved	EEMD+improved	CEEMDAN+improved
SNR (dB)	28.881	29.222	30.959
RMSE	0.054	0.055	0.042

4. Experimental verification

4.1 Experimental preparation

The experimental model employed in this study for testing purposes is a steel bridge, with the schematic diagram of the vibration experimental setup shown in Figure 12. The bridge model has dimensions of 2.4 m in length, 0.3 m in width, and 0.3 m in height, and it is constructed using 4 angle steel members and 60 flat steel components. Specifically, the angle steel members are equal-angle L-beams with dimensions of 0.03 mm × 0.03 m × 0.002 m, while the flat steel components are rectangular-section moment steel with dimensions of 0.02 m × 0.002 m. The upper and lower angles and the flat steel are connected with bolts, and the constraints are fixed on the two ends. The main instruments used in this test include: dynamic data acquisition instrument (JM-3841), nondestructive intact and damaged bars, and acceleration sensor (YD-2150), as shown in Figure 13. Among them, the damaged bars are simulated by removing one-third of the cross-section, as shown in Figure 13(e).

Figure 12 Experimental model of steel frame bridge.

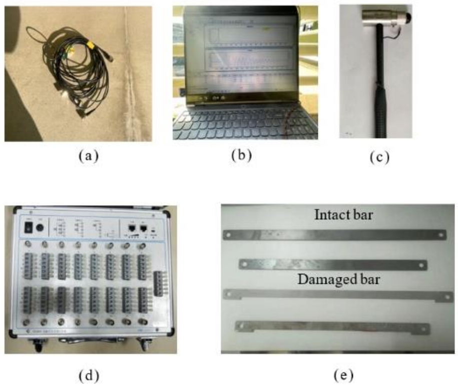

Figure 13 Experimental equipment.

4.2 Data samples

Firstly, 7 acceleration signal sensors are installed at the acquisition point location as shown in Figure 14, and each sensor is connected to the dynamic data acquisition instrument via wires, with a sampling frequency of 200 Hz and an acquisition time of 1 minute. Then, through force hammer excitation on the steel bridge model, the acceleration signals generated by the structural vibration are collected by the acceleration sensor. The force hammer is used to strike the excitation point 15 times within 1 minute, and 400 acceleration sampling points are intercepted each time, thereby obtaining 6000 × 7 sampling points from the 7 acceleration signal acquisition points.

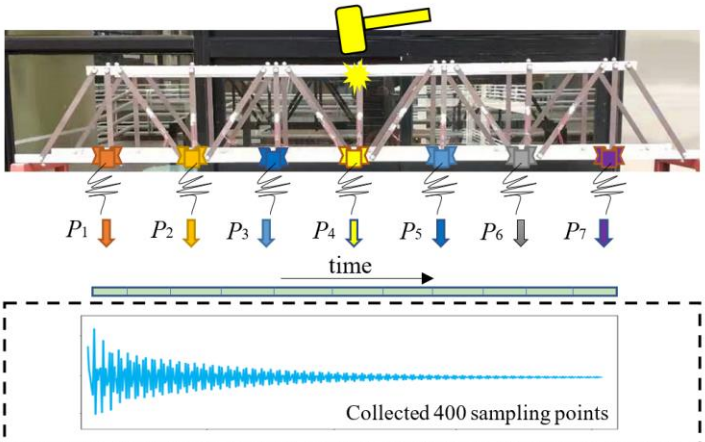

Figure 14 Signal acquisition.

In this section, the three bars marked in red in Figure 15 are taken as damage objects, numbered 1, 2 and 3 respectively. 8 damage scenarios are designed according to the different numbers of damaged bars, including 1 no-damage scenario, 3 single-damage scenarios, 3 double-damage scenarios and 1 triple-damage scenario, as shown in Table 3.

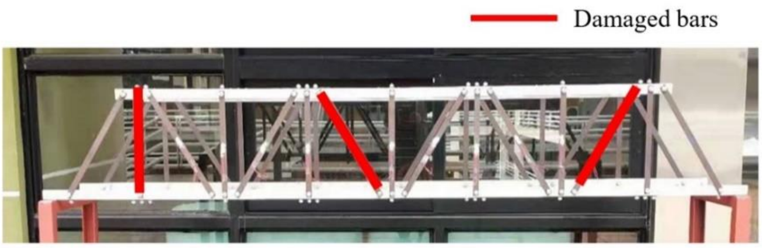

Figure 15 Damage bar location.

Table 3 Design of conditions for steel frame bridges.

Damage condition	Damage form	Damaged bars	Number of samples in training set	Number of samples in test set
1	Intact	/	406	175
2		Bar 1	406	175
3	Single damage	Bar 2	406	175
4		Bar 3	406	175
5		Bars 1、2	406	175
6	Double damage	Bars 1、3	406	175
7		Bars 2、3	406	175
8	Triple damage	Bars 1、2、3	406	175
	Total		3248	1400

Owing to the non-stationary and non-linear nature of acceleration signals, the sensor-collected data exhibit considerable variations in range, amplitude, or distribution characteristics. Direct application of these signals to the model could result in unstable training processes or compromised model learning outcomes. Therefore, it is necessary to perform normalization processing. MinmaxScaler is a common data preprocessing method, whose core principle is to mean-center and variance-scale the inputs of each layer of the neural network, so that the distribution of activation values is always maintained in a stable interval, such as [0, 1] or [-1, 1]. This method is scaled by the following Equation:

$$X_{scaled} = \frac{X - \min(X)}{\max(X) - \min(X)} \tag{12}$$

The Minmaxscaler based on Python is used to preprocess the input data, and the core code is as follows:

```
# import sklearn tool library
from sklearn.preprocessing import MinMaxScaler
# Calculate the scaling parameters based on the data
Acceleration_data = scaler.fit_transform(acceleration_data.reshape(-1, 1))
```

To transform the values of all features to a uniform scale, eliminate the differences in the magnitude of input features, thereby improve the convergence speed during model training, mitigate the problems of vanishing or exploding gradients, and enable the model to find the optimal solution more quickly, the acquired acceleration signals are normalized, as illustrated in Figure 16.

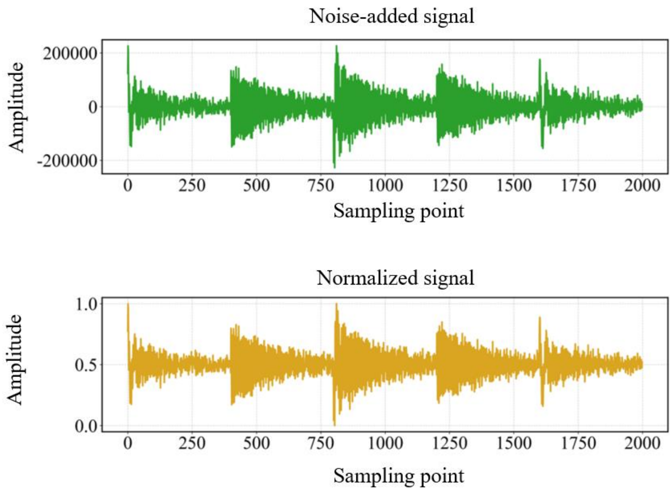

Figure 16 Normalization of data.

When the number of sampling points for acceleration signals is insufficient, overfitting tended to occur. This meant the model performed well on the training dataset but poorly on the test dataset. In other words, the selected sample data is inadequate to represent the predefined classification rules. As a commonly used regularization tool in deep learning, data augmentation could increase the number of training samples by leveraging existing data. This helped the model learn more generalizable features, reduce the risk of overfitting, and thereby enhance the model's robustness to handle different input data. Based on the improved noise reduction method, the acquired acceleration signals are normalized by three single denoising methods and combined with wavelet improved threshold denoising methods, respectively. Then the length of the window size is specified as 200, and smoothing cropping is performed with a step size of 7 to expand the samples, and 581 samples are obtained from 6000 acquisition points. Each working condition is divided into a training set and a test set at a ratio of 7:3. The total number of samples in the training set is 3248 and that in the test set is 1400, as shown in Table 4. Each sample is stored in a 200 × 7 matrix, so the input shape of the CNN is 200 × 7. The output of the CNN is the corresponding category label of 8, which corresponded to 8 different working conditions.

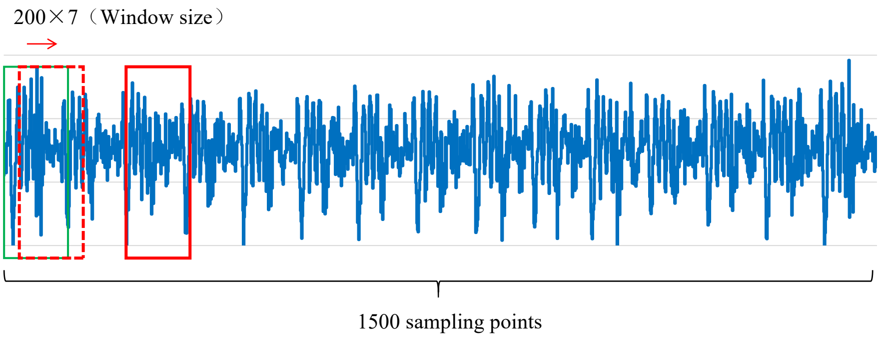

Figure 17 Sliding window.

With this data augmentation approach, it is possible to improve the generalization ability of the CNN model, making it easier to capture common features when confronted with new samples and thus make accurate predictions.

4.3 Results of CNN damage detection based on steel bridge modeling

The training curve and loss curve of a CNN serve as the most intuitive dynamic visualizations of the model training process. Together, they reveal the model's learning trajectory as it progressively approximates the underlying data distribution from an initial random state, while providing critical evidence for hyperparameter tuning, model diagnostics, and performance evaluation. The training curve fundamentally reflects a dynamic equilibrium between the model's fitting capacity and generalization capability. Under ideal conditions, both training accuracy and validation accuracy should increase synchronously before eventually plateauing, indicating that the model has effectively captured data features without underfitting or overfitting. The loss curve delineates the iterative error-correction process during optimization. The descending trend of the loss value directly demonstrates the efficacy of the gradient descent algorithm: an initial rapid decline corresponds to swift learning of dominant features; a moderated mid-phase decline signifies minor feature adjustments and weight fine-tuning; and final convergence confirms that the model has reached the optimal solution under the current parameter settings. The iterative process of training is shown in Figure 18. The blue curve in the figure represented the training accuracy of the CNN for each iteration, while the red curve represented the loss curve. The horizontal axis of the coordinate system represented the number of iterations. The red vertical axis on the left side represented the value of the loss function, while the vertical axis on the right side represented the accuracy of the training set. This is used to present the performance changes of the model on both the training and validation sets. Ideally, as the number of iterations continued to increase from 0, the training curve converged to 100 % and eventually converged, and the value of the loss curve continued to decrease and converged to zero.

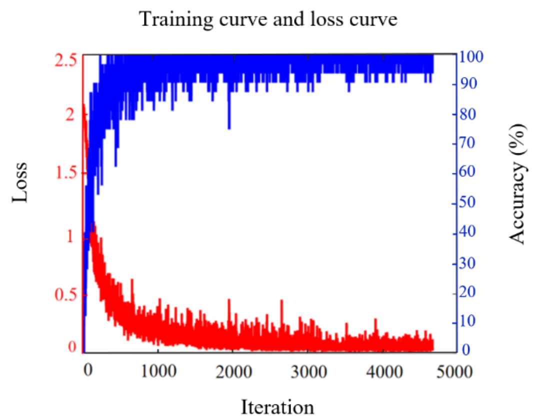

Figure 18 Training curves and loss curves of CNN.

In this section, the acceleration signals acquired from various working conditions of the steel bridge model are denoised using EMD, EEMD, CEEMDAN and a combined improved method (wavelet improved thresholding method) respectively. These denoised signals are then trained based on the constructed CNN model, and the obtained training curves and validation curves are shown in Figures19 and 20, the confusion matrix graph and test set accuracy are shown in Figure 21, and the CNN damage recognition accuracy is shown in Table 4.

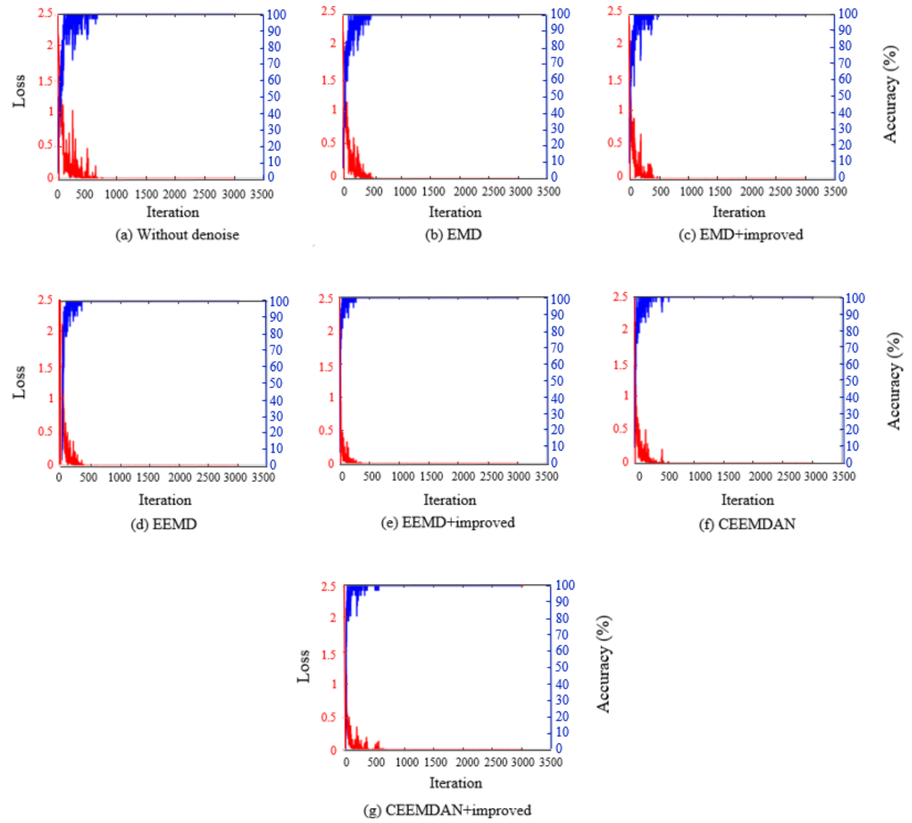

Figure 19 Training curves under different denoising methods (vibration experiments of steel frame bridge).

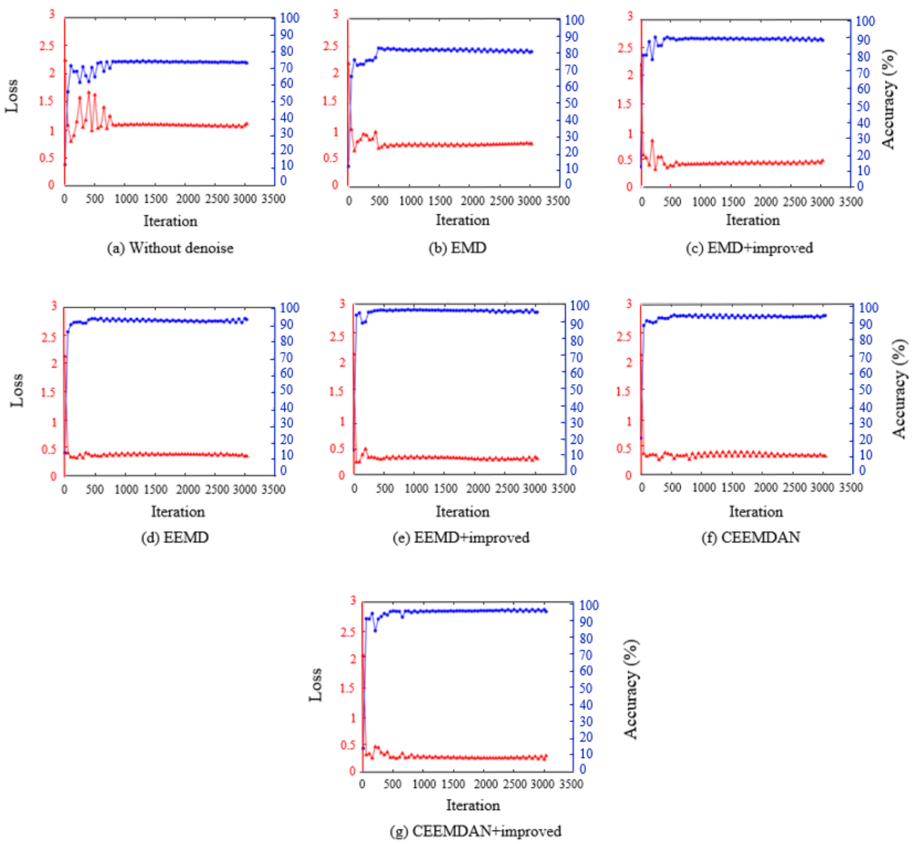

Figure 20 Validation curves using different denoising methods (vibration experiment of steel frame bridge).

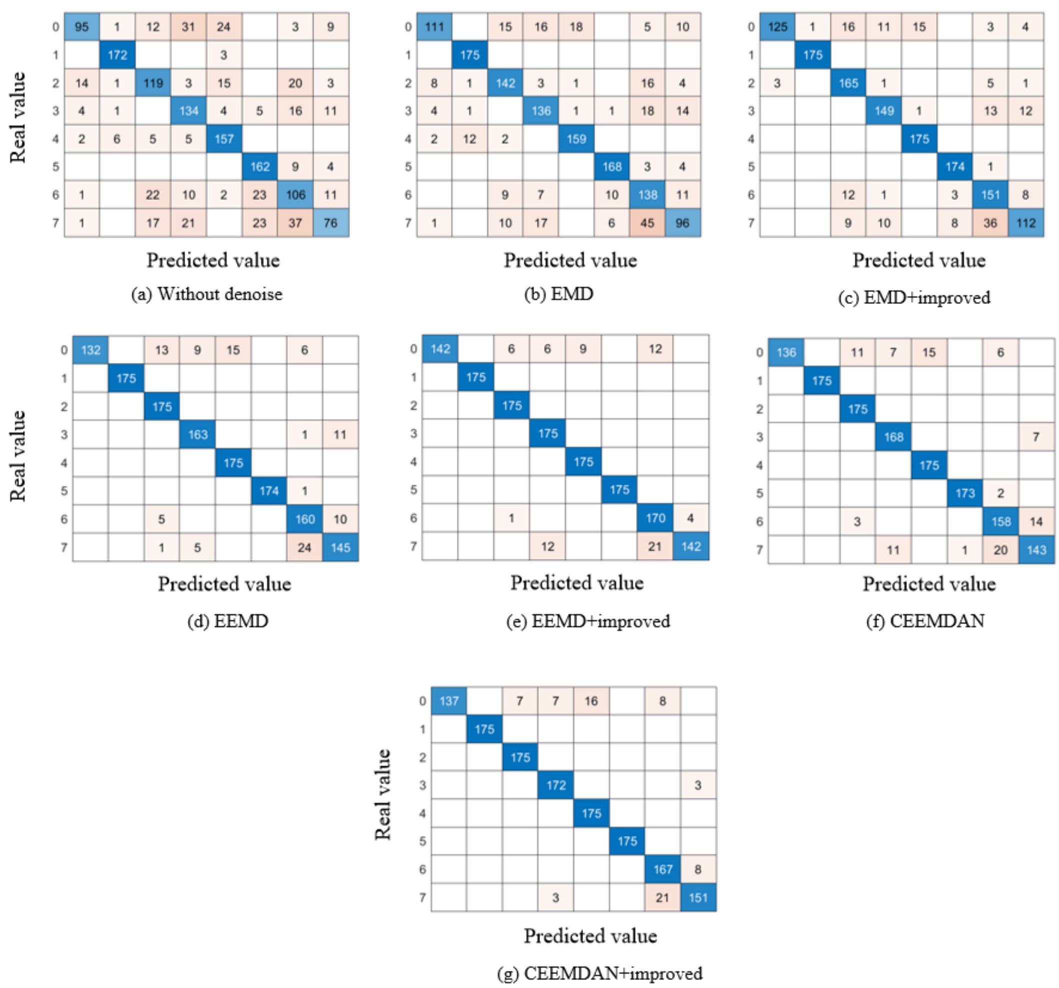

Figure 21 Confusion matrix validation results (vibration experiment of steel frame bridge).

Table 4 Accuracy of damage detection under various working conditions.

Vibration experiment of steel frame bridge							
	Without denoise	EMD	EMD+ improved	EEMD	EEMD+ improved	CEEMDAN	CEEMDAN+ improved
Accuracy	74.07%	79.14%	87.14%	92.86%	94.93%	93.07%	95.21%
Loss	1.102	0.774	0.481	0.344	0.318	0.323	0.283

The results showed that all the CNN training models had reached the convergence state, and the damage recognition accuracy of the CNNs is gradually improved by using EMD, EEMD, CEEMDAN and combined wavelet improved thresholding for noise reduction of the acceleration signals, respectively. Among them, the accuracy of combined wavelet improved threshold denoising method is higher than that of the corresponding single denoising method. The accuracy of damage recognition after EMD + improved denoising method is 8% higher than that using single EMD denoising method. After EEMD + improved denoising method, the accuracy of damage recognition of CNN is improved by 2.07% compared with single EEMD denoising method. After CEEMDAN + improved denoising method, the accuracy of damage recognition of CNN is improved the most: compared with single CEEMDAN denoising method, the accuracy is improved by 2.14 %; compared with the un-noised working condition, the accuracy is improved by 21.14 %. This result further verified that after denoising preprocessing (signal decomposition and reconstruction) is applied to acceleration signals, environmental noise interference could be effectively eliminated. This enabled the CNN to extract damage features more accurately, thereby improving the accuracy of damage detection. Additionally, the improved denoising method based on CEEMDAN combined with the wavelet-improved thresholding method exhibited a better denoising effect.

Signals denoised by single EMD, EEMD and CEEMDAN methods achieve better damage recognition performance than the original unprocessed signals. The denoising performance is further improved by introducing secondary denoising with the improved wavelet threshold algorithm. Among them, the model trained on CEEMDAN-denoised signals obtains the optimal effect, followed by EEMD, whereas EMD delivers relatively poor performance.

5. Conclusions

Signal acquisition is a critical procedure before implementing CNN-based structural damage recognition. This procedure is frequently disturbed by noise originating from environmental and human factors, which obscures the true characteristic features of signals. If noise and irrelevant features cannot be effectively removed, the CNN model will suffer from mislearning, further degrading its diagnostic accuracy. To address the above issues, this paper proposes an improved denoising method to suppress environmental noise interference and enhance the accuracy and efficiency of CNN-based damage recognition. The denoising performance is assessed via simulated signals generated from numerical experiments and validated through vibration tests of a steel frame bridge. The main conclusions are listed as follows:

(1) This paper optimizes the correlation coefficient screening strategy of EMD based on CEEMDAN and wavelet threshold denoising theories, dividing decomposed IMFs into valid and noisy components. Combined with the Heursure criterion, a modified wavelet threshold function with adjustable threshold factors is proposed on the basis of hard and soft thresholds and coded with Python loops. It calculates performance metrics under gradient thresholds and adaptively selects the optimal threshold for diverse signals. Modal decomposition and wavelet threshold denoising are combined for hybrid processing. The noisy IMFs eliminated by correlation coefficients undergo secondary improved wavelet threshold denoising to retain latent valid features. The final signal is reconstructed by superimposing denoised noisy IMFs and reserved valid IMFs.

(2) Cross-experiments are conducted to verify the denoising performance of simulated noisy signals. Various decomposition-based denoising algorithms are combined pairwise to compare the processing performance of single denoising methods and hybrid denoising methods. The results reveal that EEMD and CEEMDAN can address the end effect and mode aliasing issues existing in EMD, and suppress noise interference more effectively. The denoising performance of each of the three empirical mode decomposition algorithms combined with wavelet threshold denoising surpasses that of the corresponding algorithm used alone. Among all hybrid schemes, the combination of CEEMDAN and the improved wavelet threshold method achieves the optimal denoising performance. This method can filter out signal noise more thoroughly, yielding the highest signal-to-noise ratio and minimal signal distortion after denoising.

(3) In the vibration test of the steel frame bridge, the damage identification accuracy of the Convolutional Neural Network (CNN) increases by 2.07% when using the hybrid EEMD denoising method, compared with the single EEMD denoising scheme. The hybrid CEEMDAN

denoising method achieves the most remarkable improvement in identification accuracy: the accuracy rises by 2.14% relative to single CEEMDAN denoising, and there is a substantial increase of 21.14% compared with the original unprocessed signals. The above results further verify that denoising preprocessing of acceleration signals can effectively eliminate interference from environmental noise. This enables the CNN to extract damage features more accurately and thereby improves the overall damage identification accuracy. Among all tested schemes, the composite denoising method proposed in this paper, which combines CEEMDAN with improved wavelet thresholding, delivers significantly better denoising performance than all single denoising algorithms.

Acknowledgments
This research is partially supported by the Guangdong Province Science and Technology Department under the International Collaboration Program (Project No. 2023A0505050094).

Data Availability Statement: Some or all data, models, or code generated or used during this study are available from the corresponding author by request.

Conflict of Interest Statement: The authors declare there are no conflicts of interest associated with the present study.

Reference

[1] Wu D J. Current status and development trend of bridge engineering surveying techniques. Surveying and Mapping Bulletin, 2016, (1): 1-5.
[2] Magalhaes F, Cunha A, Caetano E. Dynamic monitoring of a long span arch bridge. Engineering Structures, 2008, 30(11): 3034-3044.
[3] Cha Y J and Buyukozturk O. Structural damage detection using modal strain energy and hybrid multi-objective optimization. Computer-Aided Civil and Infrastructure Engineering, 2015, 30(5): 347-358.
[4] Teng S, Chen G, Gong P, et al. Structural damage detection using convolutional neural networks combining strain energy and dynamic response. Meccanica, 2020, 55(4): 945-959.
[5] Lu Q, Ren G, Zhao Y. Multiple damage location with flexibility curvature and relative frequency change for beam structures. Journal of Sound and Vibration, 2002, 253(2): 1101-1114.
[6] Ni F T, Zhang J, Noori M. Deep learning for data anomaly detection and data compression of a long-span suspension bridge. Computer-aided Civil and Infrastructure Engineering, 2020, 35(7):685-700.
[7] Li M, Wu Z, Jia D, et al. Structural damage identification using strain mode differences by the iFEM based on the convolutional neural network (CNN). Mechanical Systems and Signal Processing, 2022, 165:1-10.
[8] Sun H Y and Wen F. Structural damage identification method based on displacement data. Applied Mechanics & Materials, 2014, 610:241-245.
[9] Lu H and Zhang Q C. Applications of deep convolutional neural network in computer vision. Journal of Data Acquisition and Processing, 2016, 31(1):1-17.
[10] Zhan Y L, Lu S J, Xiang T Y, et al. Application of convolutional neural network in random structural damage identification. Structures, 2021, 29:570-576.
[11] Jamshidi M and El-Badry M. Structural damage severity classification from time-frequency acceleration data using convolutional neural networks. Structures, 2023, 54:236-253.
[12] Teng S, Liu Z, Chen G, et al. Concrete crack detection based on well-known feature extractor model and the YOLO_v2 network. Applied Sciences, 2021, 11(2):813.
[13] Yang J X, Zhang L K, Li R, et al. Research on bridge structural damage detection based on convolutional and long short-term memory neural networks. Journal of Railway Science and Engineering, 2020, 17(8):1894-1901.
[14] Huang N E, Shen Z, Long S R, et al. The empirical mode decomposition and the Hilbert spectrum for nonlinear and non-stationary time series analysis. Proceedings of the Royal Society of London Series A, 1998, 454:903-995.
[15] Pines D and Salvino L. Structural health monitoring using empirical mode decomposition and the Hilbert phase. Journal of Sound & Vibration, 2006, 294(1-2):97-124.
[16] Yan P. Study on EMD wavelet correlation de-noising of bridge health monitoring sampling signals. Noise and Vibration Control, 2019, 39(3):204-209.
[17] Deering R and Kaiser J F. The use of a masking signal to improve empirical mode decomposition. IEEE

International Conference on Acoustics, Speech, and Signal Processing, Philadelphia, USA, 2005, IV:485-488.
[18] Wu Z and Huang N E. Ensemble empirical mode decomposition: a noise-assisted data analysis method. Advances in Adaptive Data Analysis, 2009, 1(1):1-41.
[19] Yeh J R, Shieh J S, Huang N E. Complementary ensemble empirical mode decomposition: a novel noise enhanced data analysis method. Advances in Adaptive Data Analysis, 2010(2):135-156.
[20] Zheng J D, Su M X, Ying W M, et al. Improved uniform phase empirical mode decomposition and its application in machinery fault diagnosis. Measurement, 2021, 179(2):109425.
[21] Torres, Marcelo A, et al. A complete ensemble empirical mode decomposition with adaptive noise. IEEE, 2011, 56(1):4144-4147.
[22] Dai T, Zhang Y, Zhang K, et al. The research progress of empirical mode decomposition and mode mixing elimination. Journal of Electronic Engineering, Yunnan University, 2019(3):1-6.
[23] He D W, Wang B X, Gao X, et al. An adaptive filtering method for bridge vibration signals based on improved CEEMDAN and multi-scale permutation Entropy. Environmental & Earth Sciences Research Journal, 2021, 8(4):163-168.
[24] Liu F, Zhang L F, Pang B H, et al. Denoising method of discharge guide wall vibration signal based on CEEMDAN and MPE and its application. Journal of Zhengzhou University (Engineering Science), 2022, 43(05):91-97.
[25] Colominas A M, Schlotthauer G, Torres E M. Improved complete ensemble EMD: A suitable tool for biomedical signal processing. Biomedical Signal Processing & Control, 2014, 14:19-29.
[26] Zhou H L, Li L M, Luo S X, et al. A method of improved threshold function denoising based on wavelet analysis. Geophysical and Geochemical Exploration Calculation Technology, 2006, 028(002):173-177.
[27] Sha L. A new wavelet threshold algorithm for deformation monitoring data denoising. Journal of Geodesy and Geodynamics, 2023, 43(8):847-850.
[28] Li H K, Wu P Z, Huang W, et al. Joint noise reduction method of hydraulic structure vibration signals based on CEEMDAN and improved wavelet threshold. Journal of Nanchang University, 2022, 44(1):1-8.
[29] Tao K and Zhu J J. A hybrid indicator for determining the best decomposition scale of wavelet denoising. Acta Geodaetica et Cartographica Sinica, 2012, 41(5):749-755.
[30] Xie X Y, Liu X G, et al. Gait acceleration signal preprocessing with wavelet denoising. Geomatics and Information Science of Wuhan University, 2022, 47(11):1956-1962.
[31] Zhu J and Tao K. A reliable evaluation index for wavelet denoising quality. Geomatics and Information Science of Wuhan University, 38(4), 501- 505.
[32] Gan R, Chen T W, Zheng X D, et al. Research on the denoising of deformation monitoring data with improved wavelet threshold function. Journal of Geodesy and Geodynamics, 43(3), 412-417.
[33] Ayenu-Prah A and Attoh-Okine N. A criterion for selecting relevant intrinsic mode functions in empirical mode decomposition. Advances in Adaptive Data Analysis, 2010, 02(01):1-24.
[34] Li G, Lin J H, et al. Wavelet Denoising method with threshold optimization based on signal to noise ratio evaluation. Journal of Tsinghua University, 54(2), 259-264.
[35] Valencia D, Orejuela D, Salazar J, et al. Comparison analysis between rigrsure, sqtwolog, heursure and minimaxi techniques using hard and soft thresholding methods. IEEE Program of Electronics Engineering, 2016, 1(16):01-05.

Improved Physics-Informed Radial Basis Network with Boundary-Extended Centers and Curriculum Learning for High-Frequency and Time-Dependent Partial Differential Equations

***Xi Zhao[1], Yan Li[2] and †Zhiqiang Feng[3]**

[1] School of Mechanics and Aerospace Engineering Southwest Jiaotong Universiy, Chengdu 610031, China
[2] Advanced Structural Materials Mechanical Behavior and Serice Safety Key Laboratory of Sichuan Province, Chengdu 610031, China
[3] LMEE Univ-Evry, Université Paris-Saclay, Evry, France

*Presenting author: 1917909480@qq.com
†Corresponding author: feng@iup.univ-evry.fr

Abstract

Physics-informed neural networks (PINNs) provide a promising mesh-free paradigm for solving partial differential equations (PDEs). However, when applied to high-frequency vibration and long-time evolution problems, they often suffer from spectral bias, insufficient boundary fitting, and training imbalance among multiple loss terms. Building upon the physics-informed radial basis network (PIRBN) framework, this paper introduces a boundary-extended center initialization strategy that places auxiliary basis function centers outside the spatial boundaries to enhance local support near the domain boundaries, together with a gradient-magnitude-based adaptive weighting mechanism to mitigate training imbalance across different loss terms. For time-dependent problems such as two-dimensional membrane vibration, a curriculum learning strategy is further incorporated, whereby the full time interval is partitioned into progressively longer sub-intervals to alleviate error accumulation in long-time evolution. Two benchmark examples, a one-dimensional linear elastic rod under high-order vibrationand a two-dimensional membrane vibration equation in (x, y, t) spatiotemporal input form, are employed to validate the method in terms of high-frequency representation, boundary fitting, and time-dependent dynamics prediction, respectively. Numerical results demonstrate that the improved PIRBN can accurately capture high-frequency oscillatory structures and maintain stable spatiotemporal prediction capability for the membrane vibration problem, offering a viable improvement for applying PIRBN to high-frequency vibration and coupled spatiotemporal PDEs in solid mechanics.

Keywords: physics-informed radial basis network; curriculum learning; boundary-extended centers; spatiotemporal partial differential equations; high-frequency problems

Introduction

Flutter in thin-walled structures of high-speed aircraft, high-frequency response of films under periodic loading, and seismic analysis of building structures: these engineering scenarios all point to the same class of mathematical problems, i.e., the accurate solution of PDEs under high-frequency excitation. In solid mechanics, structural vibration, elastic deformation, wave propagation, and membrane dynamics can all be described by governing equations, boundary conditions, and initial conditions. Traditional numerical methods such as finite difference, finite element, and boundary element methods, while theoretically rigorous and industrially reliable, generally depend on mesh generation. When problems involve complex geometries, high-dimensional variables, parametric solving, or multi-physics coupling, mesh generation and computational cost can become limiting factors. The rise of scientific machine learning (SciML) has opened a new path for PDE solving by leveraging the universal function approximation capability of neural networks as an alternative to traditional discretization schemes, offering the potential for efficient mesh-free computation.

Among SciML approaches, PINNs are among the most representative [1]-[3]. PINNs embed PDE residuals, boundary conditions, and initial conditions directly into the loss function, enabling the network to satisfy fundamental physical laws even in the absence of large amounts of labeled data. This property makes PINNs particularly suitable for inverse problems, data-sparse scenarios, and parametric studies, compensating for the strong dependence of traditional numerical methods on labeled data and mesh quality. However, when addressing high-frequency vibration and long-time evolution problems, PINNs exhibit several critical deficiencies. First, conventional fully connected networks suffer from spectral bias, preferentially learning low-frequency components while their approximation capability for high-order modal oscillations degrades sharply as frequency increases. Second, the multiple loss terms have inconsistent gradient scales and convergence rates during training. From a neural tangent kernel (NTK) perspective, the spectral properties of the kernels corresponding to different physical constraints differ [4][5], potentially causing certain constraints to be weakened during optimization. Third, in long-time evolution problems, errors accumulate as time progresses, making it difficult to maintain prediction accuracy at later times. These issues severely limit the application of conventional PINNs to high-frequency vibration, wave propagation, and other critical scenarios in solid mechanics.

To overcome the spectral bias of fully connected networks, PIRBNs offer an alternative [6]. Radial basis function (RBF) networks use local response functions as elementary units, approximating the target solution through the superposition of multiple localized basis functions. In contrast to the global nonlinear mapping of fully connected networks, RBF networks possess an inherent local approximation property, giving them a distinct advantage in representing high-frequency oscillations, local gradient variations, and boundary-adjacent features. The PIRBN framework, which combines RBF networks with physics-informed loss functions, has demonstrated superior accuracy and convergence compared to conventional PINNs in several low-dimensional steady-state problems.

Nevertheless, PIRBNs still face three main challenges in practical applications to high-frequency vibration and time-dependent dynamics problems. First, the distribution of RBF centers has a decisive influence on the network's representational capacity: if centers are placed only within the computational domain, the basis function coverage near boundaries becomes one-sided, leading to increased boundary fitting errors; this deficiency is particularly pronounced for high-frequency modes. Second, for time-dependent problems, training directly over the full time interval requires the network to simultaneously satisfy PDE residuals, boundary conditions, and initial conditions across the entire temporal domain, sharply increasing the optimization difficulty and making the later time segments prone to error accumulation. Third, existing PIRBN benchmarks are mostly confined to low-dimensional steady-state problems, with insufficient validation on two-dimensional time-dependent problems in (x, y, t) spatiotemporal coupled input form.

To address these issues, this paper extends the existing PIRBN framework along three directions: center initialization strategy, curriculum training strategy, and spatiotemporal benchmark implementation. It should be emphasized that this work does not propose a fundamentally new network architecture; rather, it builds upon the established PIRBN concept with targeted improvements. The main contributions are as follows:
First, a boundary-extended center initialization strategy is adopted, whereby primary centers

are uniformly distributed within the computational domain while auxiliary centers are placed outside the spatial boundaries. This enhances the local support near boundaries and improves fitting accuracy for high-frequency problems with strong boundary constraints.

Second, a curriculum learning strategy is introduced into the training of time-dependent dynamics problems with PIRBN. For the two-dimensional membrane vibration equation, where training over long time intervals is difficult and prone to late-time error accumulation, the full time interval is partitioned into several progressively longer sub-intervals, allowing the model to first learn the short-time dynamic response and then gradually extend to long-time evolution, thereby reducing the optimization difficulty in the early training stages.

Third, the PIRBN is implemented for solving the two-dimensional membrane vibration equation in (x, y, t) spatiotemporal input form. The two spatial variables and the time variable are jointly taken as network inputs, and automatic differentiation is used to compute the second-order time and spatial derivatives, constructing the spatiotemporal residual for time-dependent dynamics problems.

Fourth, two representative benchmarks, a one-dimensional linear elastic rod under high-order vibration and a two-dimensional membrane vibration equation, are employed to validate the improved PIRBN in terms of high-frequency representation capability, boundary fitting performance, and spatiotemporal dynamics prediction, respectively.

The remainder of this paper is organized as follows. Section 2 reviews the fundamentals of PINNs and presents the improved PIRBN methodology in detail, including the boundary-extended center initialization strategy, (x, y, t) spatiotemporal input formulation, the gradient-magnitude-based adaptive weighting mechanism, and the curriculum learning training strategy. Section 3 validates the proposed method through two numerical examples, a one-dimensional linear elastic rod under high-order vibration and a two-dimensional membrane vibration equation, examining high-frequency representation capability, boundary fitting performance, and long-time dynamics prediction, respectively. Section 4 concludes the paper with a summary of the work and a brief outlook on future research directions.

1. Fundamentals of PINN and Improved PIRBN Methodology

1.1 Fundamentals of PINN

For a general partial differential equation problem, the mathematical formulation can be written as:

$$\mathcal{N}[\hat{u}](\mathbf{x},t) = f(\mathbf{x},t), \quad (\mathbf{x},t) \in \Omega \times [0,T] \tag{1}$$

where $\mathcal{N}[\bullet]$ denotes the differential operator, u represents the physical field variable to be solved, Ω denotes the spatial computational domain, [0, T] denotes the time interval, and f is the known source term or external loading. In the context of solid mechanics, u can represent displacement, velocity, stress, or other state variables, while the differential operator $\mathcal{N}[\bullet]$ is determined jointly by the equilibrium equations, equations of motion, constitutive relations, and geometric compatibility conditions.

The core idea of PINN is to construct a neural network $\hat{u}(\mathrm{x},\ t;\ \theta)$ with trainable parameters θ to approximate the true solution $u(\mathrm{x},\ t)$. Through automatic differentiation, the derivatives of the network output with respect to the input variables can be computed and substituted into the governing equation to obtain the PDE residual [7]:

$$r(\mathbf{x},t;\theta) = \mathcal{L}[\hat{u}](\mathbf{x},t) - f(\mathbf{x},t) \tag{2}$$

During training, PINNs typically minimize the PDE residual loss, boundary condition loss, and initial condition loss simultaneously:

$$\mathcal{L} = \lambda_r \mathcal{L}_r + \lambda_b \mathcal{L}_b + \lambda_i \mathcal{L}_i \tag{3}$$

where L_{PDE} , L_{BC} , and L_{IC} denote the PDE residual loss, boundary loss, and initial loss, respectively, and λ_{PDE} , λ_{BC} , and λ_{IC} are the corresponding weight coefficients.

The residual loss is generally defined as:

$$\mathcal{L}_r = \frac{1}{N_r} \sum_{j=1}^{N_r} \left| r(\mathbf{x}_j, t_j; \theta) \right|^2 \tag{4}$$

The boundary loss is defined as:

$$\mathcal{L}_b = \frac{1}{N_b} \sum_{j=1}^{N_b} \left| \hat{u}(\mathbf{x}_j^b, t_j^b; \theta) - u_b(\mathbf{x}_j^b, t_j^b) \right|^2 \tag{5}$$

The initial condition loss is defined as:

$$\mathcal{L}_i = \frac{1}{N_i} \sum_{j=1}^{N_i} \left| \hat{u}(\mathbf{x}_j, 0; \theta) - u_0(\mathbf{x}_j) \right|^2 \tag{6}$$

If the problem also includes an initial velocity condition, the following can be further incorporated:

$$\frac{1}{N_i} \sum_{j=1}^{N_i} \left| \frac{\partial \hat{u}}{\partial t}(\mathbf{x}_j, 0; \theta) - v_0(\mathbf{x}_j) \right|^2 \tag{7}$$

The advantage of PINNs lies in their independence from traditional mesh generation; collocation points can be sampled within the computational domain using random or quasi-random sampling strategies [8]. Moreover, the network output is a continuously differentiable function, facilitating derivative computation and subsequent physical analysis. Nevertheless, PINNs also suffer from training difficulties, loss term imbalance, and insufficient high-frequency representation, necessitating problem-specific improvements in network architecture and training strategies.

1.2 Physics-Informed Radial Basis Network

Radial basis function networks are a class of neural networks constructed from local response functions [9]. For an input variable x, the basic form of an RBF network can be expressed as:

$$\hat{u}(\mathbf{s}) = \sum_{j=1}^{N} w_j \phi_j(\mathbf{s}) + b \tag{8}$$

where N is the number of radial basis neurons, ω_j are the output layer weights, b is the bias term, and ϕ_j is the j-th radial basis function. The commonly used Gaussian radial basis function is:

$$\phi_j(\mathbf{s}) = \exp\left(-\frac{\| \mathbf{s} - \mathbf{c}_j \|^2}{2\sigma_j^2}\right) \tag{9}$$

where c_j is the center and σ_j is the width parameter. The center determines the location of the basis function's response region, while the width parameter controls its local influence range. Unlike the global nonlinear mapping of fully connected networks, RBF networks approximate the target function primarily through the superposition of local basis functions, making them well-suited for describing solutions with pronounced local variations or strong high-frequency oscillations [10].

Combining an RBF network with a physics-informed loss function yields the physics-informed radial basis network. For steady-state problems, the input variable is $x = (x_1, \ldots, x_d)$; for time-dependent problems, the input can be extended to (x, t). The network output û is used to compute derivatives via automatic differentiation, which are then substituted into the PDE residual, and the network is trained by minimizing the total loss function [11].

The advantages of PIRBN are mainly reflected in the following aspects. First, the local response characteristics of RBF networks facilitate the capture of local oscillations in high-frequency solutions. Second, the spatial distribution of RBF centers can be designed according to the problem characteristics, thereby enhancing the model's representational capacity in critical regions. Third, owing to the relatively simple network form, PIRBN offers favorable interpretability and implementation convenience in certain problems.

1.3 Boundary-Extended Center Initialization Strategy

The representational capacity of an RBF network is closely related to the distribution of its centers. For PDE problems defined on a bounded domain, if all RBF centers are located strictly within the computational domain, the physical points near the boundaries receive influence from centers on only one side, leading to potentially imbalanced basis function coverage near the boundaries. In high-frequency vibration or strong-boundary-constraint problems, this asymmetric coverage can readily cause increased boundary errors and may even affect the phase and amplitude of the overall solution.

To address this issue, this paper adopts a "uniform interior and boundary exterior extension" center initialization strategy. Let the spatial computational domain be:

$$\Omega = [a_1, b_1] \times [a_2, b_2] \times \cdots \times [a_d, b_d] \tag{10}$$

where d is the spatial dimensionality. First, a set of primary centers is generated within the computational domain using a regular grid or uniform sampling:

$$C_{\text{in}} = \{\mathbf{c}_j \,|\, \mathbf{c}_j \in \Omega,\ j = 1, 2, \ldots, N_{\text{in}}\} \tag{11}$$

Then, an extended set of centers is generated by extending a distance outward along the normal direction from the domain boundaries:

$$C_{\text{out}} = \{\mathbf{c}_j \,|\, \mathbf{c}_j \in \Omega_\delta \setminus \Omega,\ j = 1, 2, \ldots, N_{\text{out}}\} \tag{12}$$

where Ω denotes the auxiliary region formed by extending beyond the original computational domain. The final center set is:

$$C = C_{\text{in}} \cup C_{\text{out}} \tag{13}$$

It is important to emphasize that the boundary-exterior centers serve only as support points for the RBF basis functions and do not imply any expansion of the physical solution domain. The PDE residuals are still computed solely within the original computational domain Ω, and the boundary conditions are still enforced only on $\partial\Omega$.

For a one-dimensional interval, the exterior centers can be placed outside the left and right endpoints; for a two-dimensional rectangular domain, they can be placed outside all four edges. For the (x, y, t) spatiotemporal input problems in this paper, the spatial domain is two-dimensional with time as an additional input variable; therefore, the exterior extension is applied primarily to the spatial boundaries, while no physical exterior extension is applied along the time direction.

The extension distance δ can be selected based on the interior center spacing h:

$$\delta = \alpha h \tag{14}$$

Where α is the extension ratio coefficient. If α is too small, the exterior centers provide limited boundary support; if α is too large, the influence of exterior centers on the interior domain weakens, potentially reducing parameter efficiency. In practice, an appropriate extension distance can be chosen based on the center density and problem dimensionality.

1.4 PIRBN Formulation under (x, y, t) Spatiotemporal Input

For two-dimensional time-dependent problems, the physical field depends not only on the spatial coordinates (x, y) but also evolves with time t. Accordingly, the network input is defined as:

$$\mathbf{s} = (x, y, t) \tag{15}$$

The network output is:

$$\hat{u} = \hat{u}(x, y, t; \theta) \tag{16}$$

It should be noted that the "three-dimensional input" in this paper does not refer to three-dimensional spatial coordinates (x, y, z), but rather to the spatiotemporal coordinates jointly formed by two spatial variables and one time variable (x, y, t). Thus, while the underlying physical problem is two-dimensional and time-dependent, from the neural network modeling perspective the input is three-dimensional.

Under the (x, y, t) input formulation, the RBF hidden layer can be written as:

$$\phi_j(x, y, t) = \exp\left(-\frac{(x - c_{jx})^2 + (y - c_{jy})^2 + (t - c_{jt})^2}{2\sigma_j^2} \right) \tag{17}$$

where c_j is the center of the j-th radial basis function. The network output is:

$$\hat{u}(x, y, t) = \sum_{j=1}^{M} w_j \phi_j(x, y, t) + b \tag{18}$$

For the spatiotemporal computational domain:

$$\Omega_t = \Omega \times [0, T]$$

Primary center points are first uniformly distributed within $\Omega\times[0,T]$, and auxiliary center points are then placed outside the spatial boundaries. For example, when $\alpha > 0$, the spatial exterior positions can be taken as:

$$x = -\delta, \quad x = 1+\delta$$

$$y = -\delta, \quad y = 1+\delta$$

For each exterior spatial position, center points along the time direction are still placed within [0, T]. The resulting exterior center set can be expressed as:

$$C_{\text{out}} = \{(x_c, y_c, t_c) | (x_c, y_c) \in \Omega_\delta \setminus \Omega, t_c \in [0,T]\} \tag{19}$$

This treatment enhances the basis function coverage near the spatial boundaries while keeping the physical definition domain of the original PDE unchanged.

1.5 Gradient-Magnitude-Based Adaptive Weighting Mechanism

In both PINN and PIRBN, the total loss function typically comprises multiple components. Different loss terms may exhibit significant discrepancies in numerical scale, gradient magnitude, and convergence rate. If fixed weights are employed, a particular loss term may dominate the parameter updates during training, while other terms receive insufficient optimization. For dynamics problems in solid mechanics, the PDE residual, boundary conditions, and initial conditions jointly determine the accuracy of the final solution; maintaining a relative balance among the different loss terms is therefore of critical importance.

To mitigate this issue, this paper employs a dynamic weight update strategy based on gradient magnitudes. The core idea is as follows: if a given loss term has a relatively small gradient with respect to the network parameters, indicating that it provides a weaker driving force for parameter updates in the current training stage, its weight is appropriately increased; conversely, if a loss term has an excessively large gradient, its weight is reduced to prevent it from dominating the training process. Similar ideas have been validated in adaptive loss balancing methods [12].

Let the PDE residual loss, boundary loss, and initial loss be denoted respectively as:

$$\mathcal{L}_r, \quad \mathcal{L}_b, \quad \mathcal{L}_i$$

Their gradients with respect to the trainable network parameters θ are first computed:

$$\nabla_\theta \mathcal{L}_r, \quad \nabla_\theta \mathcal{L}_b, \quad \nabla_\theta \mathcal{L}_i$$

The mean squared gradient of the q-th loss term is further defined as:

$$G_q = \frac{1}{P} \sum_{p=1}^{P} \left(\frac{\partial \mathcal{L}_q}{\partial \theta_p} \right)^2 \tag{20}$$

where P is the total number of trainable network parameters and θ_p is the p-th parameter.

Using the maximum value among the current mean squared gradients as the normalization reference:

$$G_{\max} = \max(G_r, G_b, G_i)$$

the adaptive weights can be constructed as:

$$\lambda_q = \frac{G_{\max}}{G_q + \varepsilon}$$

where ε is a small positive constant to prevent division by zero. From this formulation, loss terms with smaller gradient magnitudes receive larger weights, while those with larger gradient magnitudes receive relatively reduced weights. In this manner, the physical constraint terms that are insufficiently trained are automatically reinforced in the total loss, promoting coordinated convergence among all loss terms.

Considering that updating the weights at every iteration may cause training oscillations, this paper adopts an interval-based update strategy. Specifically, the mean squared gradients of all loss terms are recomputed and the weights are updated every fixed number of iterations; between two adjacent update points, the weights remain unchanged. This strategy preserves the adaptive adjustment capability while avoiding the optimization instability that may arise from high-frequency weight variations.

1.6 Curriculum Learning Training Strategy

For time-dependent PDEs, if training is performed directly over the full time interval [0,T], the network must simultaneously satisfy the initial conditions, boundary conditions, and PDE residuals across the entire temporal domain. When T is large or the solution exhibits pronounced oscillatory characteristics, the optimization process is prone to slow residual decay, increased errors at later times, and training instability.

To improve the training process for long-time evolution problems, this paper introduces a curriculum learning strategy. The fundamental idea of curriculum learning is to organize training tasks in an easy-to-hard progression [13]. For time-dependent PDEs, the full time interval can be partitioned into several progressively longer sub-intervals:

$$[0,T_1] \subset [0,T_2] \subset \cdots \subset [0,T_K] = [0,T]$$

where:

$$0 < T_1 < T_2 < \cdots < T_K$$

In the k-th training stage, the model is trained only on spatiotemporal collocation points sampled within:

$$\Omega \times [0,T_k]$$

After completing the current stage, the trained network parameters are inherited and the time interval is extended to T_k. In this way, the model first learns the fundamental dynamic response over short time durations and then gradually adapts to more complex evolution processes over longer time ranges.

The loss function for the k-th training stage is:

$$\mathcal{L}^{(k)} = \lambda_r^{(k)}\mathcal{L}_r^{(k)} + \lambda_b^{(k)}\mathcal{L}_b^{(k)} + \lambda_i^{(k)}\mathcal{L}_i^{(k)} \tag{21}$$

The curriculum learning training procedure is as follows:
1. Initialize the RBF centers, width parameters, output layer weights, and bias;
2. Define the time curriculum sequence $\{T_1,\ T_2,\ldots,\ T_K\}$;

3. In the k-th stage, sample collocation points within $\Omega\times[0,\ T_k]$;
4. Construct the PDE residual loss, boundary loss, and initial loss;
5. Train using the Adam optimizer, periodically updating the adaptive weights;
6. Upon completion of the current stage, inherit the network parameters and proceed to the next time interval;
7. Continue until training over the full time interval [0, T] is completed.

This strategy reduces the optimization difficulty in the early stages of training and helps mitigate the error accumulation problem in long-time prediction.

2. Numerical Examples and Results Analysis

To validate the effectiveness and stability of the proposed improved PIRBN in solving high-frequency PDEs, this section selects three representative benchmark problems for numerical analysis: a one-dimensional linear elastic rod vibration problem, a two-dimensional high-frequency Poisson equation, and a two-dimensional membrane vibration problem. These three examples correspond to a one-dimensional dynamics problem, a two-dimensional static high-frequency field problem, and a two-dimensional long-time dynamics problem, respectively, and together provide a comprehensive assessment of the proposed method in terms of local high-frequency structure representation, boundary constraint satisfaction, long-time evolution stability, and coordinated convergence of multiple loss terms.

2.1 One-Dimensional Linear Elastic Rod Vibration Equation

We first consider the longitudinal free vibration problem of a one-dimensional linear elastic rod. Let the rod length be L, the material be homogeneous, and the linear elastic assumption hold. The spatial modes satisfy the following second-order ordinary differential equation:

$$\frac{d^2u(x)}{dx^2}+\omega^2u(x)=0, \qquad x\in[0,L] \tag{22}$$

where u(x) denotes the modal displacement function of the rod at spatial position x, and λ is the eigenvalue parameter of the corresponding mode.

Considering fixed-end boundary conditions at both ends:

$$u(0)=0, \qquad u(L)=0$$

Under these conditions, the equation admits a set of discrete modal solutions, with the n-th mode shape expressible as:

$$u(x)=\sin(\frac{n\pi x}{L}) \tag{23}$$

Accordingly, the following boundary value problem is adopted in the numerical implementation as the one-dimensional benchmark, taking the 8th-order mode:

$$\begin{cases} u_{xx}(x)=-\omega^2\sin\left(\dfrac{8\pi x}{L}\right) \\ u(0)=0, \qquad u(L)=0 \end{cases} \tag{24}$$

The 8th-order mode of this benchmark is characterized by high-frequency features, placing stringent demands on the local feature capturing capability of numerical methods. It thus serves as an ideal test case for verifying whether PIRBN can overcome the high-frequency information decay deficiency of conventional PINNs.

PINN Training Results

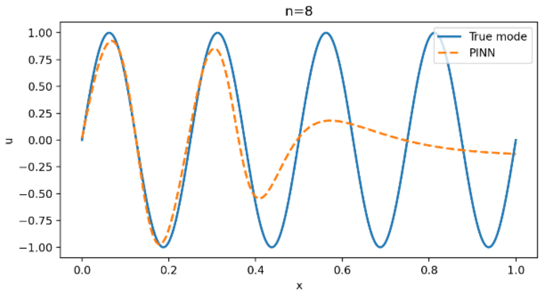

a. n=8

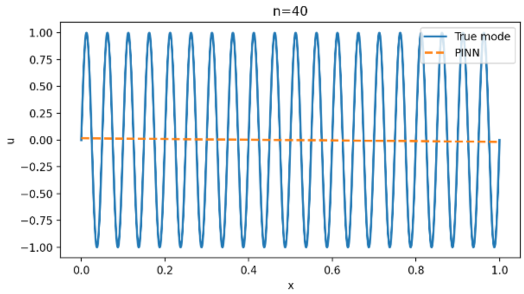

b. n=40

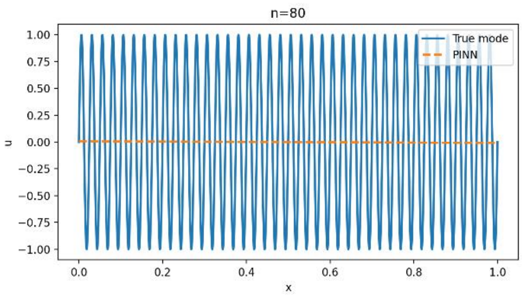

c. n=80

Fig. 1. PINN predictions for the 1D linear elastic rod vibration equation

To verify the limitations of conventional PINNs in high-frequency problems, the predicted solutions of PINNs under different high-order modes are compared with the analytical solutions. As n increases, the PINN solution progressively loses the original oscillatory structure. As shown in Fig. 1(a), at n = 8, the PINN solution can roughly follow the true solution within a small region near the left endpoint, but begins to deviate markedly as x increases; the amplitude decreases significantly at later positions, the phase gradually shifts, and the periodic structure can hardly be maintained in the latter half of the domain. At n = 40 and n = 80, the PINN solution almost completely fails to recover the oscillatory pattern, exhibiting a smooth, near-zero profile over the entire interval. These observations reveal the typical spectral bias exhibited by PINNs during training [15]: the network tends to learn low-frequency components preferentially, and its ability to fit high-frequency content degrades significantly with increasing frequency. This deficiency severely restricts the applicability of conventional PINNs to high-frequency vibration and wave propagation problems.

PIRBN Training Results

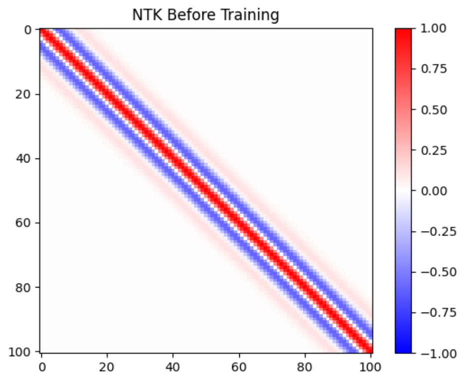

a. NTK matrix during model initialization

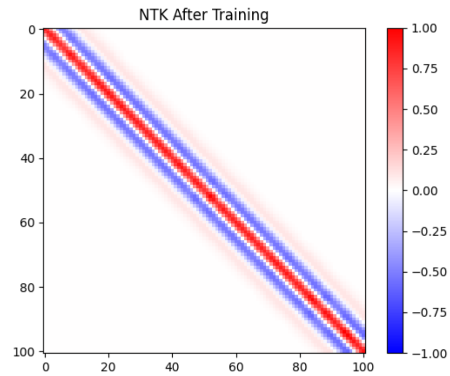

b. Trained NTK matrix

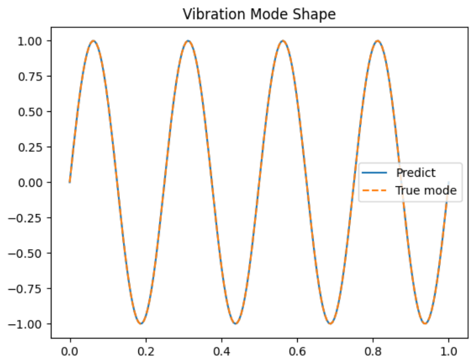

c. Predictions and Analytical Solutions

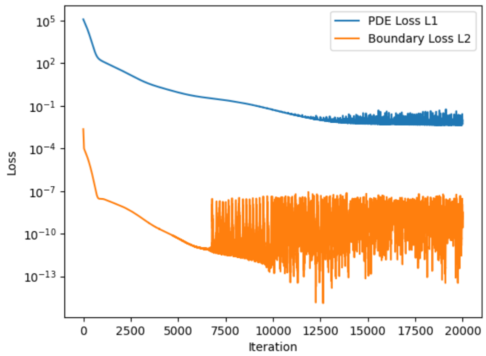

d. Loss curve after 20,000 iterations

Fig. 2. PIRBN predictions for the 1D linear elastic rod vibration equation

After 20,000 training iterations, the PIRBN numerical results exhibit excellent accuracy and stability: the PDE residual stabilizes at 4.74×10^{-3}, indicating that the network output satisfies the physical constraints of the one-dimensional wave equation with high precision; the boundary condition error is as low as 8.20×10^{-5}, achieving accurate boundary fitting; and the global maximum prediction error is 8.20×10^{-5}, representing an improvement of more than one order of magnitude compared to the maximum absolute error of approximately 3.62×10^{-3} for conventional PINNs on the same class of problems.

Regarding the visualized results: Fig. 2(a) shows the NTK matrix before training, which exhibits a pronounced diagonal banded structure consistent with the locality property of RBF networks: kernel values of neighboring points are strongly correlated, while those of distant points are weakly correlated. The slight gradation around the diagonal indicates that the local influence range under the initial parameters is limited, which is key to the RBF architecture's ability to preserve local approximation capacity. Fig. 2(b) shows the NTK matrix after training; its structure remains nearly identical to that before training, demonstrating that the locality structure of the NTK is stably maintained throughout the training process. The kernel values are very close to those of the initial matrix, confirming that PIRBN can sustain stable training kernel properties in high-frequency wave problems, thereby preserving high accuracy and convergence rate. Fig. 2(c) presents the comparison between the predicted and analytical solutions; the two curves almost completely coincide, indicating high prediction accuracy over the entire domain and demonstrating that PIRBN successfully fits the mode shape distribution, with its local structure effectively preventing the accumulation of high-frequency or boundary errors. Fig. 2(d) shows the loss curves over 20,000 iterations; the PDE residual and boundary loss achieve good balance during training, with the boundary condition converging more rapidly. The adaptive NTK-based weighting markedly enhances the coordinated convergence of the multiple loss terms.

2.2 Two-Dimensional Membrane Vibration Equation

Two-dimensional membrane vibration is a classical dynamics problem in solid mechanics and engineering mechanics, with wide applications in membrane structures, drumheads, micro-electromechanical systems (MEMS), and acoustic devices. Its physical essence is as follows: under the small-deformation assumption, the transverse displacement of a uniform membrane under tension evolves in space and time according to the two-dimensional wave equation.

Let u(x, y, t) denote the transverse displacement of the two-dimensional membrane at spatial position (x, y) and time t, and let c be the wave speed in the membrane. The motion satisfies the two-dimensional wave equation:

$$\frac{\partial^2 u(x,y,t)}{\partial t^2} = c^2\left[\frac{\partial^2 u(x,y,t)}{\partial x^2} + \frac{\partial^2 u(x,y,t)}{\partial y^2}\right], \quad for(x,y,t)\in\Omega\times\left[0,T\right] \tag{25}$$

The computational domain is taken as the unit square region $\Omega=\left[0,1\right]\times\left[0,1\right]$, and the time domain is $t\in\left[0,T\right]$.

For simplicity, a dimensionless formulation is adopted with c = 1, yielding the standard two-dimensional membrane vibration governing equation:

$$u_{tt} = u_{xx} + u_{yy} \tag{26}$$

Considering that the membrane is fixed on all four edges, the corresponding Dirichlet boundary conditions are:

$$u(x,y,t)=0, \ for(x,y)\in\partial\Omega, \ \ t\in\left[0,T\right] \tag{27}$$

To facilitate quantitative verification of the numerical results, the following initial displacement and initial velocity are prescribed:

$$\begin{cases} u(x,y,0)=\phi(x,y) \\ u_t(x,y,0)=\psi(x,y) \end{cases} \tag{28}$$

The high-order mode of the two-dimensional membrane is selected as the initial perturbation:

$$\phi(x,y)=sin\left(4\pi x\right)sin\left(4\pi y\right), \psi(x,y)=0 \tag{29}$$

Under the above boundary and initial conditions, the two-dimensional membrane vibration equation can be solved analytically via separation of variables:

$$u(x,y,t)=sin\left(4\pi x\right)sin\left(4\pi y\right)\cos(\omega t) \tag{30}$$

where the natural frequency is $\omega_{mn} = \pi\sqrt{m^2 + n^2}$. This analytical solution serves as the reference true solution for subsequent error evaluation and model accuracy verification.

To verify the capability of the PIRBN method for solving the two-dimensional membrane vibration equation, numerical solutions are obtained and compared with the analytical solution to assess model accuracy. The analytical solution exhibits a $sin(m\pi x)sin(n\pi y)$ modal distribution in the spatial domain Ω and oscillates at relatively high frequency over time, placing demanding requirements on the spatiotemporal approximation capability of the network.

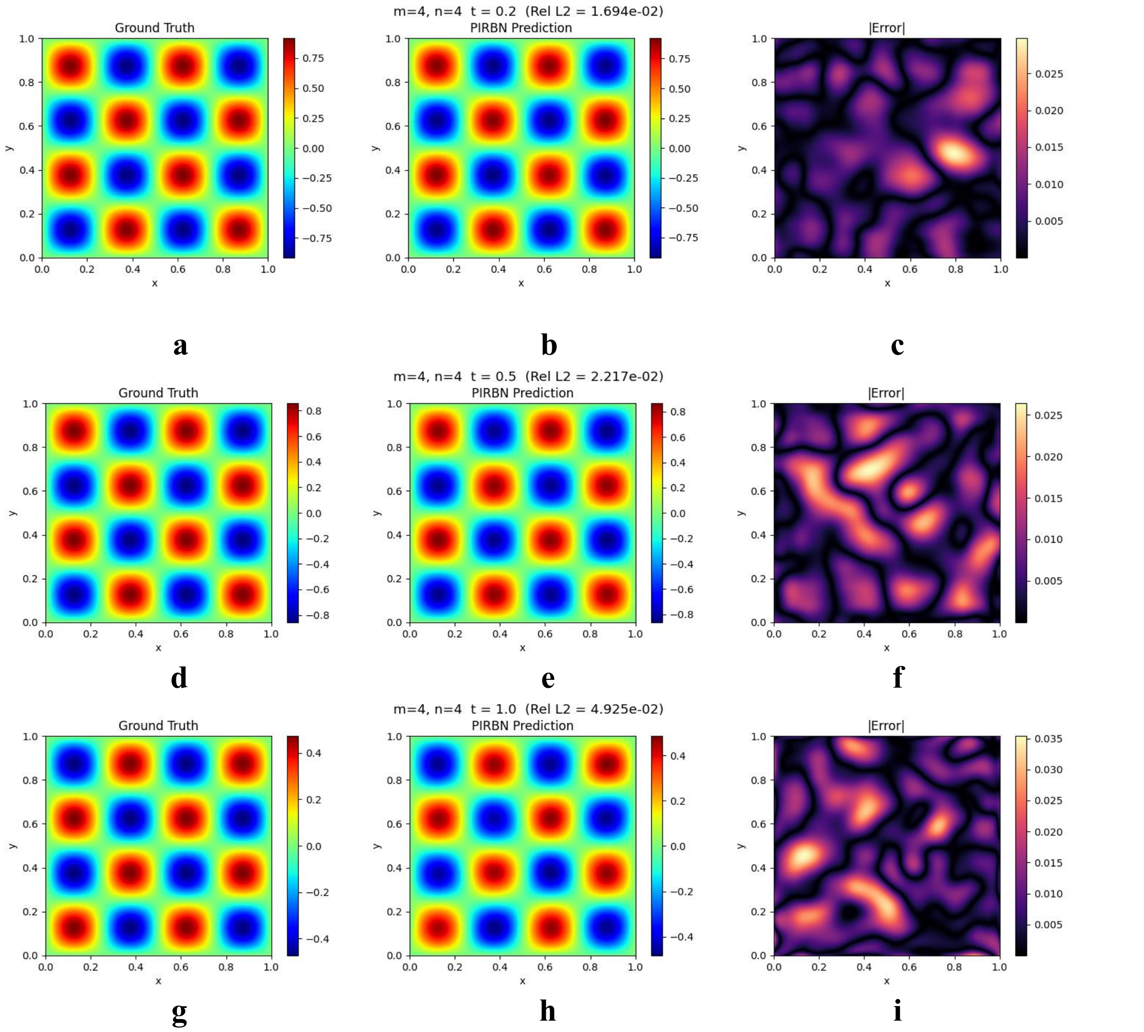

Fig. 4. Comparison of predicted and analytical solutions at different training stages. Fig. a, b and c show the analytical solution, predicted solution and prediction error for T=0.2, Fig. d, e and f for T=0.5, Fig. g, h and i for T=1.0

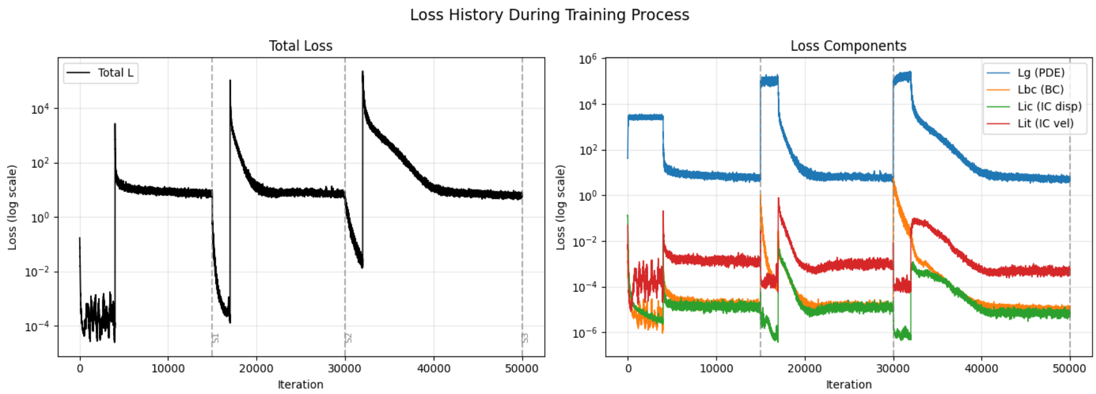

Fig. 5. Loss curves during training

Regarding the network architecture, a three-dimensional Gaussian RBF network is employed with 31 center points in each spatial direction and 21 in the time direction, totaling 31×31×21 = 20,181 hidden neurons. The width parameter is initialized at $b_0 = 12.0$ and is optimized as a learnable parameter during training. The output layer is linear, forming a single-hidden-layer RBF network with favorable local approximation characteristics.

Regarding the training strategy, the time domain $[0,T]$ is progressively extended over three stages: the first stage trains to $T = 0.2$ with 15,000 iterations at a learning rate of 10^{-3}, where the first 4,000 steps serve as a warm-up phase optimizing only the boundary and initial condition losses; the second stage extends to $T = 0.5$ with 15,000 iterations at a reduced learning rate of 8×10^{-4}; the third stage extends to $T = 1.0$ with 20,000 iterations at a further reduced learning rate of 5×10^{-4}, for a total of 50,000 iterations across all three stages. For the NTK-based adaptive weighting mechanism in this problem, the weight coefficients λ are dynamically updated every 500 iterations based on the ratios of the gradient norms of the respective loss terms, mitigating the scale imbalance among the multiple optimization objectives and ensuring balanced optimization of the PDE residual, boundary conditions, and initial conditions during training.

Fig. 1 presents the comparison between the predicted and analytical solutions at $T = 0.2$, $T = 0.5$, and $T = 1.0$. In terms of spatial distribution, the PIRBN predictions accurately reproduce the $\sin(4\pi x)\sin(4\pi y)$ modal vibration pattern at all three time instants, with the alternating positive-negative spatial structure in close agreement with the analytical solution and near-identical color distributions. In terms of error distribution, the absolute errors are mainly concentrated near the nodal lines and in certain boundary regions, while the errors at the wave peaks and troughs are relatively small, which is consistent with the local approximation characteristics of RBF networks. The relative L_2 errors at the three time instants are 1.694×10^{-2}, 2.217×10^{-2} and 4.925×10^{-2}, and the maximum pointwise errors are 2.980×10^{-2}, 2.638×10^{-2}, and 3.500×10^{-2}, respectively. The errors exhibit a certain degree of cumulative growth with increasing time, which is consistent with the inherent nature of temporal extrapolation problems and reflects the gradually increasing difficulty of PDE residual optimization as the time domain is extended.

Fig. 5 shows the loss curves for the complete training process. From the total loss curve, a brief jump in the loss is observed at the beginning of each training stage, caused by the sharp increase in the PDE residual term L_{PDE} due to the newly introduced collocation points after time domain extension; the loss subsequently decreases rapidly and stabilizes, indicating that the network can quickly adapt within the new temporal range. From the individual loss components, the boundary condition loss L_{BC} and the initial displacement loss L_{IC}_disp remain below the 10^{-5} level throughout the training process, while the initial velocity loss L_{IC}_vel remains at the 10^{-4} level, demonstrating that the network satisfies the boundary and initial conditions to a high degree. The PDE residual loss L_{PDE} converges to approximately the 10^{-2} level by the end of each stage. The overall training process is stable, validating the effectiveness of the PIRBN method under the synergistic action of the curriculum training strategy and the NTK-based adaptive weighting mechanism for solving high-frequency time-domain wave problems.

Conclusions

This paper has addressed the issues of spectral bias, insufficient boundary fitting, and long-time training instability that conventional PINNs commonly encounter in high-frequency vibration and time-dependent dynamics problems. Building upon the existing PIRBN framework, an improved methodology incorporating a boundary-extended center initialization strategy and a curriculum learning training strategy has been developed and validated through multiple representative numerical examples. The following conclusions are drawn:

1. Radial basis function networks possess strong local approximation capabilities that are well-suited for representing high-frequency oscillatory solutions. As demonstrated by the one-dimensional linear elastic rod high-order vibration example, PIRBN can accurately capture high-frequency oscillatory structures.

2. The boundary-extended center initialization strategy, i.e., uniform interior distribution combined with auxiliary centers outside the spatial boundaries, effectively improves the basis function coverage near the domain boundaries. In the two-dimensional membrane vibration equation, this strategy contributes to enhanced boundary condition fitting and reduced numerical errors near boundaries.

3. For time-dependent problems such as the two-dimensional membrane vibration equation, the curriculum learning strategy, whereby the time interval is progressively extended from short to long durations during training, enables the network to first learn the short-time dynamic response and then gradually adapt to the periodic evolution over longer time ranges, thereby improving the stability of the training process.

4. This paper implements PIRBN for solving the two-dimensional membrane vibration equation under (x, y, t) spatiotemporal input. This example demonstrates that PIRBN is applicable not only to low-dimensional steady-state problems, but also to spatiotemporally coupled PDEs involving the time variable, providing a reference for further applications of PIRBN in solid mechanics dynamics problems.

In summary, the primary contribution of this work is the integration of curriculum learning, boundary-extended center initialization, and the (x, y, t) spatiotemporal input formulation into the PIRBN framework, offering a viable numerical approach for solving high-frequency vibration and time-dependent PDEs. Future work may extend to complex geometries and nonlinear material constitutive models, high-dimensional and multi-physics coupled problems, theoretical analysis of training efficiency and convergence, and the fusion of experimental data with uncertainty quantification, thereby advancing the method from theoretical investigation toward engineering practice. This study is limited to regular computational domains and linear elastic materials. Practical engineering structures often feature complex geometries and nonlinear constitutive relations. In future work, PIRBN can be combined with domain decomposition techniques or immersed boundary methods to extend its application to irregular geometric domains, and nonlinear stress-strain relations can be introduced to verify its capability in solving nonlinear PDEs.

References

[1] Lagaris I E, Likas A, Fotiadis D I. Artificial neural networks for solving ordinary and partial differential equations[J]. IEEE transactions on neural networks, 1998, 9(5): 987-1000.
[2] M. Raissi, P. Perdikaris, G.E. Karniadakis, Physics-informed neural networks: A deep learning framework for solving forward and inverse problems involving nonlinear partial differential equations, Journal of Computational Physics, Volume 378, 2019, Pages 686-707, ISSN 0021-9991.
[3] Lu L, Meng X, Mao Z, et al. DeepXDE: A deep learning library for solving differential equations[J]. SIAM review, 2021, 63(1): 208-228.
[4] Jacot A, Gabriel F, Hongler C. Neural tangent kernel: Convergence and generalization in neural networks[J]. Advances in neural information processing systems, 2018, 31.
[5] Wang S, Yu X, Perdikaris P. When and why PINNs fail to train: A neural tangent kernel perspective[J]. Journal of Computational Physics, 2022, 449: 110768.
[6] Gorbachenko, V.I., Stenkin, D.A. Physics-Informed Radial Basis-Function Networks. Tech. Phys. 68, 151–157 (2023). https://doi.org/10.1134/S1063784223050018
[7] Baydin A G, Pearlmutter B A, Radul A A, et al. Automatic differentiation in machine learning: a survey[J]. Journal of machine learning research, 2018, 18(153): 1-43.
[8] McKay M D, Beckman R J, Conover W J. A comparison of three methods for selecting values of input variables in the analysis of output from a computer code[J]. Technometrics, 2000, 42(1): 55-61.
[9] Broomhead D S, Lowe D. Radial basis functions, multi-variable functional interpolation and adaptive networks[R]. 1988.
[10] Fasshauer G E. Meshfree approximation methods with Matlab (With Cd-rom)[M]. World Scientific Publishing Company, 2007.
[11] Goodfellow I, Bengio Y, Courville A. Deep Learning[M].Cambridge: MIT Press, 2016.
[12] Bai J, Liu G R, Alzubaidi L, et al. Physics-informed radial basis network (PIRBN) for solving nonlinear partial differential equations[C], The 14th International Conference of Computational Methods (ICCM2023). 2023.
[13] Bengio Y, Louradour J, Collobert R, et al. Curriculum learning[C], Proceedings of the 26th annual international conference on machine learning. 2009: 41-48.

Research on a CAD system for large-scale simulations using generative AI

***Yuze Li[1], †Ryuji Shioya[1]**

[1]Graduate School of Information Sciences and Arts, Toyo University, Japan.

*Presenting author: greatgodcong@gmail.com
†Corresponding author: shioya@toyo.jp

Abstract

Large-scale numerical simulations are widely used to reproduce and predict complex physical phenomena in aerospace engineering, climate science, disaster mitigation, and other fields. However, preparing CAD models and analysis-ready meshes requires considerable time and human effort. This study develops an AI-assisted CAD system to reduce the workload involved in geometric modeling and mesh preparation for large-scale simulations. In recent years, generative AI has been adopted in many fields for reasons such as increased efficiency and cost reduction, and CAD software equipped with AI capabilities has also been developed. While AI-powered CAD software is expected to support human work and reduce working time, However, current AI-powered CAD systems still face challenges related to generation accuracy and the creation of complex geometries. This study develops an AI-assisted CAD system intended to reduce the workload involved in preparing geometric models and analysis-ready meshes. In the proposed system, a user describes the target geometry and dimensional constraints using text or images. Generative AI then produces Python code for FreeCAD or, for printed circuit board applications, a KiCad-compatible design file. The generated model is inspected and, when necessary, corrected in FreeCAD or KiCad. Mechanical models are exported in STL format, converted into MSH mesh files using Gmsh and Python, and analyzed with the ADVENTURE system, a large-scale CAE system developed at the University of Tokyo. Simulation results are converted to VTK format and examined in ParaView. In a preliminary experiment, three AI models each generated 48 CAD models. Claude Sonnet 5 achieved the highest overall accuracy. For simple geometries, the AI-assisted workflow reduced modeling time from several tens of minutes to less than 10 minutes. These results demonstrate the feasibility of connecting generative AI, open-source CAD tools, mesh generation, and large-scale CAE in a unified workflow, while also identifying the reliability improvements required for practical use.

Keywords: Generative AI, CAD, Simulation, System Construction, open-source software

Introduction

Large-scale numerical simulation uses supercomputers to reproduce and predict complex physical phenomena with high fidelity. Such simulations support research and engineering in aerospace, climate science, disaster mitigation, and other fields in which thermal, structural, fluid, or coupled behavior must be resolved [1]. A typical simulation workflow includes CAD model preparation, mesh generation, boundary-condition definition, numerical analysis, and evaluation of the computed results. Among these stages, CAD model preparation can demand considerable time and human effort, particularly when many geometric variations must be evaluated [2].

Recent advances in generative artificial intelligence have led to methods that assist in CAD model creation [3]-[6]. These methods have the potential to shorten design time and reduce cost. Nevertheless, important challenges remain, including the reliable generation of complex geometries, geometric and dimensional accuracy, integration with computer-aided engineering (CAE) tools, and the high licensing costs associated with some commercial systems [7]. Furthermore, a practical workflow for large-scale simulations requires capabilities that go beyond merely generating shapes that look plausible. Specifically, it must be able to output editable shapes, support mesh generation, and integrate seamlessly with downstream solvers and visualization environments. However, few studies have investigated an integrated workflow that connects generative AI-based CAD modeling with mesh generation, large-scale simulations, and scientific visualization.

This study proposes an AI-assisted CAD system for large-scale simulations. The system combines generative AI with FreeCAD, KiCad, Gmsh, Python, the ADVENTURE system, and ParaView. The objective is to reduce the time required to create CAD models and to improve the efficiency of simulation preparation without removing the user from model verification and correction.

Research Objective

The objective of this study is to develop an AI-assisted CAD system for large-scale simulations. For simple geometries, the proposed workflow reduced modeling time compared with manual modeling. Furthermore, the entire system is built exclusively using open-source software.

This study also investigates whether AI-generated models can be transferred to a large-scale CAE system with minimal manual intervention: inspecting and modifying models in FreeCAD or KiCad prior to analysis, exporting the mechanical models in STL format, generating meshes using Gmsh and Python, and finally importing them into the ADVENTURE system.

Proposed Methodology

The user first provides a textual or image-based description of the target object, including its shape and dimensional constraints. The AI system interprets this input and generates Python code suitable for execution in FreeCAD. After the code has been executed, the resulting CAD model is visually and geometrically inspected. If the model satisfies the specified requirements, it is exported as an STL file. The STL model is subsequently converted into an MSH-format mesh using Gmsh and Python. The mesh is then prepared for analysis in the ADVENTURE system. Finally, the computed results are converted into VTK format using Python and visualized in ParaView.

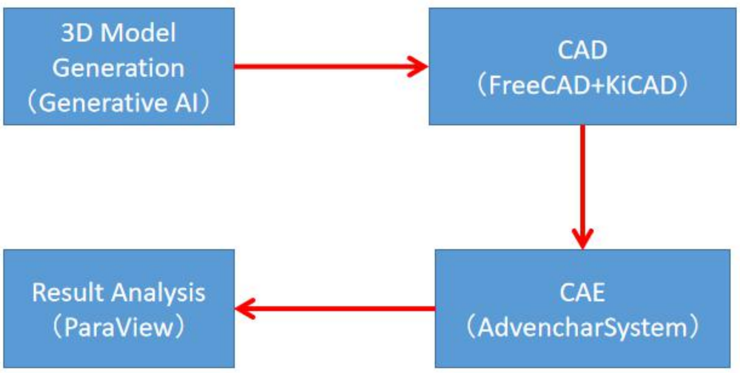

Figure 1. Research workflow

AI-Based CAD Model Generation

This study evaluated Claude Sonnet 5, ChatGPT 5.5 Instant, and Gemini 3.1 Pro. Each AI model generated CAD model files or Python code. Generation time and CAD generation accuracy were compared to assess performance.

For mechanical parts, a user enters a textual specification containing dimensions, and the AI outputs Python code for FreeCAD. For electronic circuit boards, a user provides a circuit diagram and component model numbers, and the AI generates a PCB file for KiCad. KiCad was included to examine the applicability of the proposed system to electronic circuit board models, which may be used in thermal or electromagnetic simulations.

Figure 2. AI interaction for electronic circuit board generation

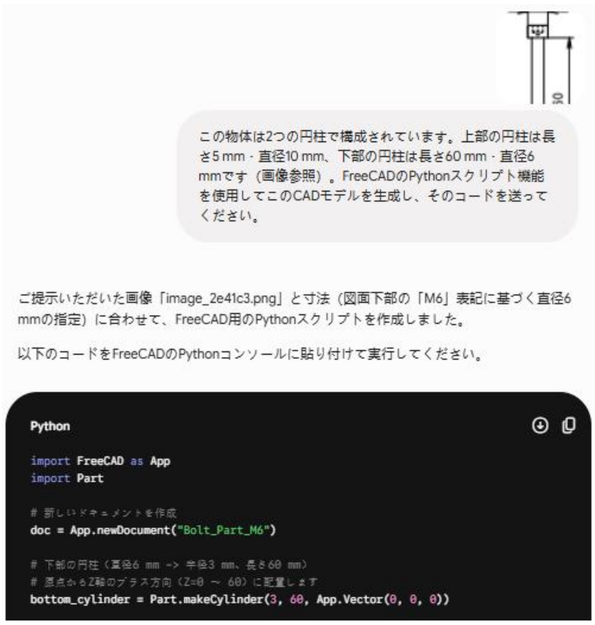

Figure 3. AI interaction for mechanical part generation

CAD Model Verification and Correction

FreeCAD and KiCad are used as open-source environments for inspecting and, where necessary, modifying AI-generated models. For mechanical parts, the generated Python code is executed in FreeCAD and the resulting solid is assessed against the user's dimensional and geometric requirements. For electronic projects, the PCB file is opened in KiCad and checked for component models, part numbers, placement information, and other relevant design details. Manual adjustments are made when the generated output is incomplete or inaccurate.

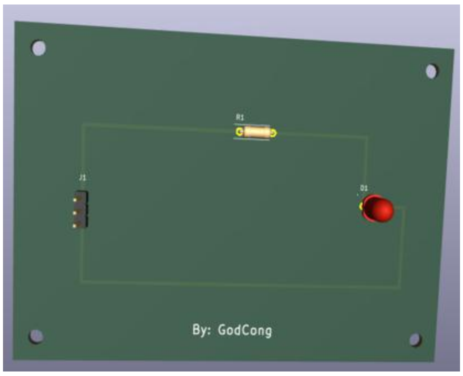

Figure 4. Verification of an AI-generated CAD model

Mesh Generation

After verification, a mechanical CAD model is exported as an STL file. Gmsh is then used with Python scripts to convert the STL geometry into an MSH mesh file. Mesh conversion also serves as a practical test of whether the generated geometry is sufficiently consistent for CAE use.

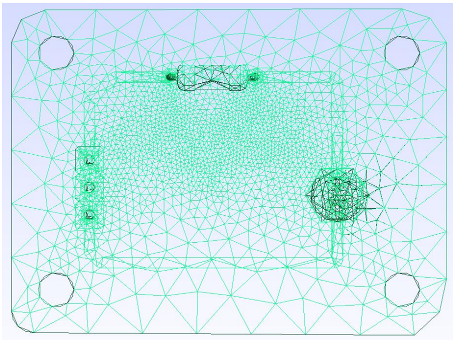

Figure 5. Generated mesh model

Simulation

The generated mesh is analyzed using the ADVENTURE system, a CAE system for large-scale simulations developed at the University of Tokyo. The analysis stage evaluates whether an AI-assisted CAD model can be passed successfully into an established simulation workflow. Boundary conditions and other analysis settings are defined for the selected model before execution.

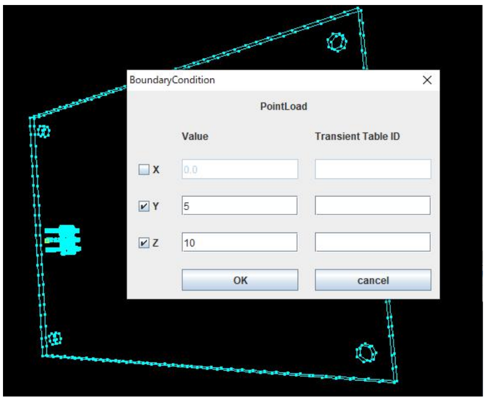

Figure 6. Boundary-condition definition for simulation

Visualization of Simulation Results

After the simulation, Python is used to convert the ADVENTURE system output into VTK format. ParaView is then used for the visualization of large-scale scientific datasets. The visualized fields allow the user to inspect the numerical results and determine whether the generated CAD model and mesh function as intended in the simulation environment.

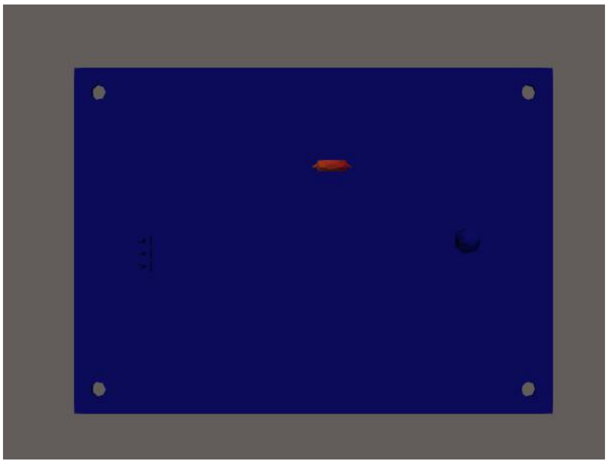

Figure 7. Visualization of simulation results

Preliminary Results

This study proposes an AI-assisted CAD system for large-scale simulations to improve CAD workflow efficiency and reduce user workload.

In a preliminary experiment, three AI models each generated 48 models, which were subsequently converted into mesh data. The results are summarized in Table 1. The detailed performance of each AI model is presented in Tables 2–4.

Table 1. Comparison of AI-based automatic CAD generation performance

AI model	Simple success /18	Moderate success /11	Complex success /19	Total success /48	Mean generation time
Claude Sonnet 5	17	5	4	26	1.5 min
ChatGPT 5.5 Instant	15	5	4	24	< 1 min
Gemini 3.1 Pro	13	2	1	16	< 1 min

Table 2. CAD generation results for Claude Sonnet 5

Geometry category	Successful	Revision required	Failed
Simple geometry (18)	17	1	0
Moderately complex geometry (11)	5	5	1
Complex geometry (19)	4	4	11

Table 3. CAD generation results for Gemini 3.1 Pro

Geometry category	Successful	Revision required	Failed
Simple geometry (18)	13	5	0
Moderately complex geometry (11)	2	3	6
Complex geometry (19)	1	5	11

Table 4. CAD generation results for ChatGPT 5.5 Instant

Geometry category	Successful	Revision required	Failed
Simple geometry (18)	15	3	0
Moderately complex geometry (11)	5	2	4
Complex geometry (19)	4	5	10

The evaluation by difficulty level showed that Claude Sonnet 5 achieved the highest overall CAD generation accuracy. For simple geometries, the AI-assisted workflow reduced tasks that had previously required several tens of minutes to less than 10 minutes. In addition, for moderately complex geometries generated by Claude Sonnet 5, 5 models were generated successfully and 5 additional models became usable after minor manual corrections, resulting in a post-revision success rate of 90.9%. In contrast, generation failures occurred for complex curved surfaces and when dimensional specifications were insufficient. These findings demonstrate that simple and moderately complex models can be generated efficiently.

All 26 models successfully generated by Claude Sonnet 5 were displayed correctly in FreeCAD, exported as STL files, and converted into mesh files using Gmsh. Among the generated models, three were selected for trial analysis using the ADVENTURE system. Two simulations were completed successfully, while one failed due to an error in the Python-based mesh conversion process. This indicates that the connection between CAD generation, mesh conversion, and CAE analysis is feasible, but the robustness of the conversion process must be improved.

Future work will evaluate a larger number of models and improve the Python code to establish a system that can reliably analyze generated mesh data using the ADVENTURE system.

References

[1] Tsubokura, M. (2016) Applied aerodynamics simulation for the next generation based on massively parallel CFD: From the K computer to the post-K computer, Journal of the Japan Society of Fluid Mechanics 35(2), 77–85.

[2] Aoki, T., Shen, D. and Watanabe, S. (2025) Effectiveness study of a driftwood trap device attached to a closed dam using a large-scale flow simulation with 1,000 pieces of driftwood on a GPU supercomputer, Proceedings of the Conference on Computational Engineering and Science 30, 658–663.

[3] Kanagawa Institute of Industrial Science and Technology, Information and Production Technology Department, Systems Technology Group (2025) Proposal for 3D CAD model generation using generative AI, KISTEC Research Report, 77–85.

[4] Mizuno, Y., Inoue, N., Aoyama, N., Bando, Y. and Otani, H. (2020) Automatic construction technology for three-dimensional models using two-dimensional CAD data, Civil Engineering Journal 62(11), 36–39 (in Japanese).

[5] Yoo, S., Lee, S., Im, S., Hwang, K. H., Park, J. H. and Kang, N. (2021) Integrating deep learning into CAD/CAE system: Generative design and evaluation of a 3D conceptual wheel, Structural and Multidisciplinary Optimization 64(4), 2725–2747.

[6] Schüpbach, A., San Miguel, R., Ferchow, J. and Meboldt, M. (2025) From text to design: A framework to leverage LLM agents for automated CAD generation, Proceedings of the Design Society 5, 1893–1902.

[7] Autodesk, Autodesk AutoCAD: Pricing and product information, available at: https://www.autodesk.com/jp/products/autocad/overview (accessed 18 June 2026).

Analysis of anisotropic thick plates using finite strip-elements

†*J. Petrolito and D. Ionescu
Department of Engineering, La Trobe University, Australia.
*Presenting author: j.petrolito@latrobe.edu.au
†Corresponding author: j.petrolito@latrobe.edu.au

Abstract

In this paper, we discuss the use of the finite strip-element method for the static and vibration analysis of multi-span, thick and thin plate structures with anisotropic properties. The method uses a combination of polynomial and trigonometric shape functions, and all boundary conditions are correctly treated. The global equations are derived using standard finite element procedures and in closed form for numerical efficiency. Accurate solutions are obtained with the generation and solution of few equations.

Keywords: Thick plates, anisotropic properties, numerical analysis, finite strip-elements.

Introduction

Finite strip methods have been successfully used for the analysis of engineering structures for many years [1, 2]. For problems that are amenable to analysis, finite strips have several advantages over finite elements. Originally, the method was developed for analysing thin rectangular plates with two opposite edges simply supported and using trigonometric approximation functions in one direction. In this case, the global equations uncouple into a number of smaller systems of equations owing to orthogonality relationships resulting from the chosen displacement functions. This gives better computational efficiency when compared with finite elements.

However, the global equations do not generally uncouple for other boundary conditions, and this reduces the computational efficiency of the method. In addition, the shape functions used in the traditional finite strip method do not correctly satisfy free edge boundary conditions, and this leads to potential errors in such cases [3].

The finite strip method has been extended and refined since its introduction, and the method has been successfully used for linear and nonlinear problems, including dynamic effects [2]. Research in this area is continuing in relation to the fundamental theory of the method and a diverse range of applications [4–10].

The finite strip-element method is an alternative finite strip method, and it was developed to overcome the deficiencies of the original finite strip method, while maintaining its basic efficiency [3, 11, 12]. Finite strip-elements combine the shape functions of finite elements and finite strips. In this method, all boundary conditions are correctly treated in the usual manner of finite element methods. In this paper, we extend our previous work and consider the use of finite strip-elements for the analysis of anisotropic thick and thin multi-span plate structures, such floor slabs in buildings and bridge decks. Several examples are considered in the paper that demonstrate the efficiency and accuracy of the method.

Governing Equations

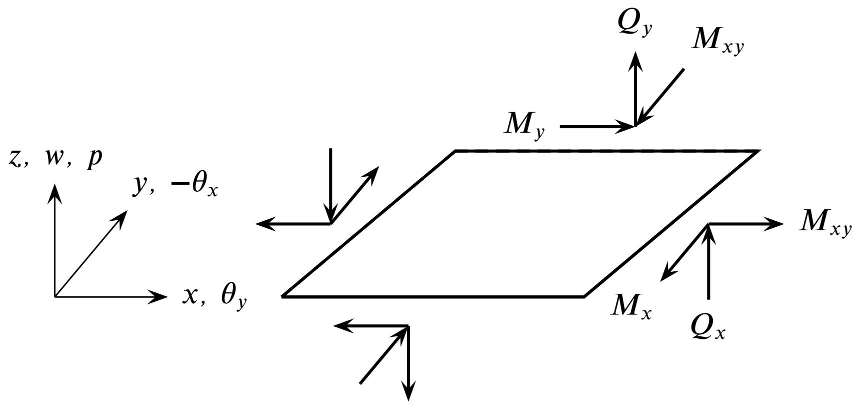

Figure 1. Sign convention.

Mindlin's theory incorporates independent assumptions for the transverse displacement w and normal rotations θ_x and θ_y (see Fig. 1). Both bending and transverse shear strains are possible in this theory, and these are given by

$$\boldsymbol{\epsilon}_b = \begin{bmatrix} \partial/\partial x & 0 \\ 0 & \partial/\partial y \\ \partial/\partial y & \partial/\partial x \end{bmatrix} \begin{Bmatrix} \theta_x \\ \theta_y \end{Bmatrix} = \mathbf{L}_1 \boldsymbol{\theta} \tag{1a}$$

$$\boldsymbol{\epsilon}_s = \begin{Bmatrix} \partial/\partial x \\ \partial/\partial y \end{Bmatrix} w - \boldsymbol{\theta} = \mathbf{L}_2 w - \boldsymbol{\theta} \tag{1b}$$

where $\boldsymbol{\epsilon}_b$ is the bending strain vector and $\boldsymbol{\epsilon}_s$ is the shear strain vector, which is zero in the thin plate limit.

For an anisotropic material, the bending moments, **M**, and shears, **Q**, shown in Fig. 1 are given in terms of the strains by

$$\mathbf{M} = \begin{Bmatrix} M_x \\ M_y \\ M_{xy} \end{Bmatrix} = \begin{bmatrix} D_{11} & D_{12} & D_{13} \\ D_{12} & D_{22} & D_{23} \\ D_{13} & D_{23} & D_{33} \end{bmatrix} \boldsymbol{\epsilon}_b = \mathbf{D}\boldsymbol{\epsilon}_b \tag{2a}$$

$$\mathbf{Q} = \begin{Bmatrix} Q_x \\ Q_y \end{Bmatrix} = \begin{bmatrix} G_{11} & G_{12} \\ G_{12} & G_{22} \end{bmatrix} \boldsymbol{\epsilon}_s = \mathbf{G}\boldsymbol{\epsilon}_s \tag{2b}$$

where **D** is the matrix of bending rigidities and **G** is the matrix of shear rigidities.

For a material that is uniform in the z direction, the terms in **D** and **G** are given in terms of the fundamental material properties by

$$D_{ij} = \frac{h^3 E^b_{ij}}{12}, \quad G_{ij} = khE^s_{ij} \tag{3}$$

where the E^b_{ij} and E^s_{ij} are in-plane and transverse material moduli, respectively, h is the plate thickness and k is the shear correction factor, which is usually taken as $5/6$ or $\pi^2/12$. Analogous expressions can be obtained for layered plates [13].

Eq. (3) simplifies for orthotropic and isotropic materials. For an orthotropic material, $D_{13} = D_{23} = G_{12} = 0$, and

$$D_{11} = \frac{E_x h^3}{12(1 - \nu_{xy}\nu_{yx})} \tag{4a}$$

$$D_{22} = \frac{E_y h^3}{12(1 - \nu_{xy}\nu_{yx})} \tag{4b}$$

$$D_{12} = \frac{\nu_{xy} E_y h^3}{12(1 - \nu_{xy}\nu_{yx})} \tag{4c}$$

$$D_{33} = \frac{G_{xy} h^3}{12} \tag{4d}$$

$$G_{11} = khG_{xz} \tag{4e}$$

$$G_{22} = khG_{yz} \tag{4f}$$

where E_x and E_y are Young's moduli, ν_{xy} and $\nu_{yx} = \nu_{xy}E_y/E_x$ are Poisson's ratios, G_{xy} is the in-plane shear modulus and G_{xz} and G_{yz} are the transverse shear moduli. For an isotropic material, $D_{11} = D_{22} = D = Eh^3/[12(1-\nu^2)]$, $D_{12} = \nu D$, $D_{33} = D(1-\nu)/2$ and $G_{11} = G_{22} = E/[2(1+\nu)]$.

The static equilibrium equations are

$$\mathbf{L}_3\boldsymbol{\sigma} + \mathbf{p} = \mathbf{0} \tag{5}$$

where

$$\boldsymbol{\sigma} = \begin{Bmatrix} \mathbf{M} \\ \mathbf{Q} \end{Bmatrix}, \quad \mathbf{p} = \begin{Bmatrix} \mathbf{0} \\ p \end{Bmatrix}, \quad \mathbf{L}_3 = \begin{bmatrix} \mathbf{L}_1^T & \mathbf{I} \\ \mathbf{0} & \mathbf{L}_2^T \end{bmatrix} \tag{6}$$

In Eq. (6), p is the applied transverse load, $\mathbf{0}$ represents a zero matrix and $\mathbf{I}$ represents an identity matrix.

Analytical solutions of the governing equations are generally not possible, particularly in the anisotropic case, except for very simple cases. Hence, practical problems require a numerical solution and various methods are available, with the finite element method being the predominant one [2].

Strip-element interpolation

In this paper, we develop various rectangular strip-elements. The extension of the method to curved structures is also possible using the techniques described previously [11].

Fig. 2 shows a typical plate structure that can be analysed using the proposed method. The only requirement for the method to be applicable is that the structure can be divided into rectangular sections as shown. Different boundary conditions can be applied on any line or node.

Fig. 3 shows a typical rectangular strip-element j, where the dashed lines are internal nodal lines. The strip-element variables are associated with nodal lines parallel to the x axis. The number of internal nodal lines depends on the interpolation order used in the y direction. There are L nodal lines for the strip-element, with $L = 2$ giving the lowest order strip-element possible, and there are no internal nodal lines for this strip-element.

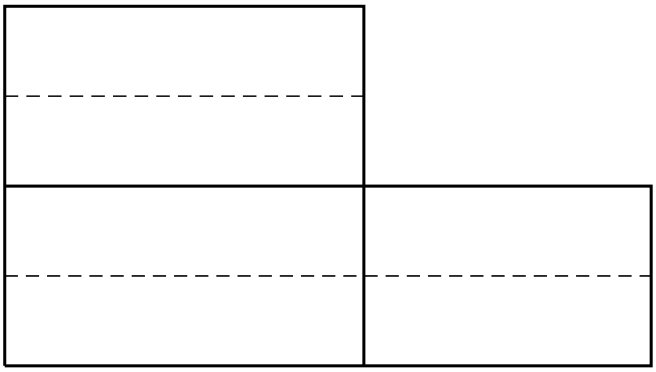

Figure 2. Typical structure suitable for analysis.

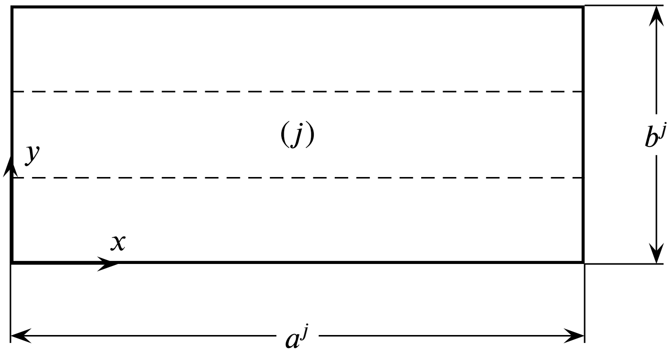

Figure 3. Geometry of finite strip-element (L = 4).

To enforce continuity on nodal line i, which is the lth nodal line of the jth strip-element, the displacements and rotations are taken as

$$w^i(\xi) \equiv w^{j,l}(\xi), \quad \theta^i_x(\xi) \equiv \theta^{j,l}_x(\xi), \quad \theta^i_y(\xi) \equiv \theta^{j,l}_y(\xi) \tag{7}$$

where $\xi = x/a^j$ and a^j is the strip-element length.

Within strip-element j, the displacement and rotations are approximated by

$$w^j(x,y) = \sum_{l=1}^{L} w^{j,l}(\xi) f^L_l(\eta), \quad \theta^j_x(x,y) = \sum_{l=1}^{L} \theta^{j,l}_x(\xi) f^L_l(\eta), \quad \theta^j_y(x,y) = \sum_{l=1}^{L} \theta^{j,l}_y(\xi) f^L_l(\eta) \tag{8}$$

where $\eta = y/b^j$, and the functions $f^L_l(\eta)$ are Lagrange polynomials [2], with $L = 2$ corresponding to a linear variation in the y direction. Any order of approximation can be used in the y direction by increasing L with a corresponding increase in the number of internal nodal lines. However, the range $2 \leq L \leq 4$ is generally sufficient for practical problems.

Along a nodal line, the displacements and rotations are approximated by the sum of polynomial and trigonometric terms. Accordingly, the displacement and rotations along nodal line i are approximated by

$$w^i(\xi) = \sum_{m=1}^{M} W^{j,l}_m \sin\alpha_m\xi + \widetilde{W}^{j,l}_1 f^3_1(\xi) + \widetilde{W}^{j,l}_2 f^3_2(\xi) + \widetilde{W}^{j,l}_3 f^3_3(\xi) \tag{9a}$$

$$\theta^i_x(\xi) = \sum_{m=1}^{M} \Theta^{j,l}_{xm} \left\{\cos\alpha_m\xi - f^3_1(\xi) - (-1)^m f^3_3(\xi)\right\} + \widetilde{\Theta}^{j,l}_{x1} f^3_1(\xi) + \widetilde{\Theta}^{j,l}_{x2} f^3_2(\xi) + \widetilde{\Theta}^{j,l}_{x3} f^3_3(\xi) \tag{9b}$$

$$\theta_y^i(\xi) = \sum_{m=1}^{M} \Theta_{ym}^{j,l} \sin \alpha_m \xi + \widetilde{\Theta}_{y1}^{j,l} f_1^3(\xi) + \widetilde{\Theta}_{y2}^{j,l} f_2^3(\xi) + \widetilde{\Theta}_{y3}^{j,l} f_3^3(\xi) \tag{9c}$$

where $\alpha_m = m\pi$ and M is the total number of trigonometric terms. The coefficients $W_m^{j,l}$, $\widetilde{W}_1^{j,l}$, $\widetilde{W}_2^{j,l}, \ldots, \widetilde{\Theta}_{y3}^{j,l}$ are the basic variables for the problem.

Equations (7) to (9) can be written concisely in matrix form as

$$w^j(x, y) = \mathbf{N}_w^j(x, y)\mathbf{W}^j, \quad \boldsymbol{\theta}^j(x, y) = \mathbf{N}_\theta^j(x, y)\boldsymbol{\Theta}^j \tag{10}$$

where $\mathbf{N}_w$ and $\mathbf{N}_\theta$ are shape function matrices and $\mathbf{W}^j$ and $\boldsymbol{\Theta}^j$ are vectors of the strip-element coefficients.

Formulation of strip-element matrices

Using Eqs. (1) and (10), the strains within the strip-element are

$$\boldsymbol{\epsilon}_b^j = \mathbf{L}_1\mathbf{N}_\theta^j\boldsymbol{\Theta}^j = \mathbf{B}_b^j\boldsymbol{\Theta}^j, \quad \boldsymbol{\epsilon}_s^j = \mathbf{L}_2\mathbf{N}_w\mathbf{W}^j - \mathbf{N}_\theta^j\boldsymbol{\Theta}^j = \mathbf{B}_s^j\mathbf{W}^j - \mathbf{N}_\theta^j\boldsymbol{\Theta}^j \tag{11}$$

The strip-element stiffness matrix $\mathbf{k}^j$ is obtained from its strain energy, giving

$$\mathbf{k}^j = \int_0^{b^j}\int_0^{a^j} \left\{ \begin{bmatrix} \mathbf{0} & \mathbf{B}_b^j \\ \mathbf{B}_s^j & \mathbf{0} \end{bmatrix}^T \begin{bmatrix} \mathbf{D} & \mathbf{0} \\ \mathbf{0} & \mathbf{G} \end{bmatrix} \begin{bmatrix} \mathbf{0} & \mathbf{B}_b^j \\ \mathbf{B}_s^j & \mathbf{0} \end{bmatrix} \right\} dx\, dy \tag{12}$$

A reduced integration technique [2] is used for the integrals in Eq. (12) to avoid locking in the thin plate limit ($h = 0$). The integrals in Eq. (12) associated with the bending strain energy are performed analytically. In contrast, for the integrals associated with the shear strain energy, integration in the x direction is performed analytically, whereas integration in the y direction is performed using Gauss quadrature with $G = L - 1$ Gauss points. This number is one less than that required to integrate the terms associated with the shear energy exactly in the y direction.

The strip-element load vector $\mathbf{r}^j$ is given by

$$\mathbf{r}^j = \int_0^{b^j}\int_0^{a^j} p\mathbf{N}_w^{jT}\, dx\, dy \tag{13}$$

The integrals in Eq. (13) are performed analytically.

The formulation can also be used for dynamics problems by developing a strip-element mass matrix, $\mathbf{m}^j$, which is calculated from its kinetic energy, giving

$$\mathbf{m}^j = \rho h \int_0^{b^j}\int_0^{a^j} \left\{ [\,\mathbf{N}_w^T \quad \mathbf{N}_\theta^T\,] \begin{bmatrix} \mathbf{I} & \mathbf{0} \\ \mathbf{0} & \frac{h^2}{12}\mathbf{I} \end{bmatrix} \begin{bmatrix} \mathbf{N}_w \\ \mathbf{N}_\theta \end{bmatrix} \right\} dx\, dy \tag{14}$$

where ρ is the density of the material. The integrals in Eq. (14) are performed analytically. The terms in Eq. (14) that are associated with the rotations are frequently neglected [13].

Global equations

The assembly of the global equations from the strip-element matrices follows standard finite element procedures [2]. The global equations for static problems can be written as

$$\mathbf{K}\boldsymbol{\phi} = \mathbf{R} \tag{15}$$

where $\mathbf{K}$ is the global stiffness matrix, which is symmetric, $\mathbf{R}$ is the global load vector and $\boldsymbol{\phi}$ is the global variables vector. Boundary conditions are enforced by assigning appropriate values to $\boldsymbol{\phi}$. The resulting equations are solved for the unknown variables $\boldsymbol{\phi}$, and the structural response is found by back-substitution, as in the normal manner of the finite element method.

The calculation of the natural frequencies of vibration leads the global equations

$$\mathbf{K}\boldsymbol{\phi} = \Omega^2\mathbf{M}\boldsymbol{\phi} \tag{16}$$

where Ω is the natural frequency of the structure and $\mathbf{M}$ is the global mass matrix for the structure. The eigenvalue problem can be efficiently solved using the subspace iteration technique [14].

Examples

We now consider several examples to illustrate the behaviour and accuracy of the finite strip-element method. The examples that we have chosen are deliberately small plate structures. However, they illustrate all the issues we have discussed in the theoretical parts of this paper, and hence serve our purposes. Of course, the method can be used for more general plate structures that can be subdivided into rectangular sections if required.

The material is assumed to be orthotropic with $E_x = 10E_y$, $\nu_{xy} = 0.25$, $G_{xy} = 0.5E_y$, $G_{xz} = 0.5E_y$ and $G_{yz} = 0.2E_y$ [13]. Anisotropic properties were generated from the orthotropic properties by assuming that the material's orthotropic x axis is rotated by an angle α anticlockwise from the strip-element's x axis. A value of $\alpha = 30°$ was used in all cases. This value of α produces significant anisotropic coupling of the material properties, and hence it provides a good test of the method to analyse plate structures with anisotropic properties.

Shear deformation was included in all examples. A shear correction factor of $k = 5/6$ was used for the static problems and $k = \pi^2/12$ was used the natural frequency calculations. Shear deformation can be ignored by using an artificially high value of k.

The boundary conditions are described as follows:

1. Hard simple support (S): $w = \theta_t = M_{nn} = 0$
2. Clamped support (C): $w = \theta_t = \theta_n = 0$
3. Free edge (F): $M_{nn} = M_{nt} = Q_n = 0$

where n and t are the normal and tangential directions, respectively, at the boundary. Mindlin's theory also allows the use of a soft simply support, with only the condition $w = 0$ being enforced [2]. However, this condition is not used as it precludes the derivation of exact solutions for some of the examples.

Simply-supported plate

Fig. 4 shows a square plate size $a \times a$ and thickness h that is subjected to a uniform load p. Each side of the plate is either simply supported or clamped.

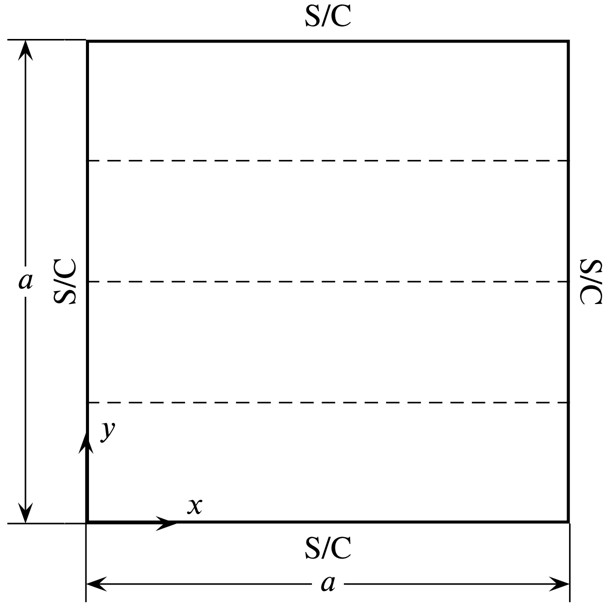

Figure 4. Square plate of size a × a with typical subdivision (N = 5).

As a first example, we consider a simply-supported plate. The analysis used 13 and 25 nodal lines, N, to compare the different strip-elements. A value of $a/h = 10$ was used to simulate a thick plate, while a value of $a/h = 100$ was used to simulate a thin plate. The results for the central displacement are given in Tables 1 and 2, and they are compared to the exact results from [13].

Table 1. Central displacement, w, for simply-supported orthotropic plate subjected to uniform load (a/h = 10; exact value = 1.679; multiplier = $10^{-2}pa^4/E_y/h^3$).

	N = 13			N = 25		
M	$L = 2$	$L = 3$	$L = 4$	$L = 2$	$L = 3$	$L = 4$
1	1.692	1.682	1.682	1.684	1.682	1.682
5	1.689	1.679	1.679	1.681	1.679	1.679
10	1.689	1.679	1.679	1.681	1.679	1.679
15	1.689	1.679	1.679	1.681	1.679	1.679

In general, both N and M need to be increased for convergence. Convergence is rapid for all strip-elements and engineering accuracy with errors of around 2% - 5% is obtained with the solution of few equations. The quadratic and cubic strip-elements are slightly more accurate than the linear strip-elements. The results also demonstrate that the method can deal with both thick and thin plates without locking problems.

The results for the central bending moment, M_x, are given in Tables 3 and 4, and they are also compared to the exact results from [13]. The convergence is also rapid, and the trends for the different strip-elements are similar to the displacement trends.

Table 2. Central displacement, w, for simply-supported orthotropic plate subjected to uniform load (a/h = 100; exact value = 1.415; multiplier = $10^{-2}pa^4/E_y/h^3$).

	$N=13$			$N=25$		
M	$L=2$	$L=3$	$L=4$	$L=2$	$L=3$	$L=4$
1	1.425	1.418	1.418	1.420	1.418	1.418
5	1.423	1.415	1.415	1.417	1.415	1.415
10	1.423	1.415	1.415	1.417	1.415	1.415
15	1.423	1.415	1.415	1.417	1.415	1.415

Table 3. Central bending moment, M_x, for simply-supported orthotropic plate subjected to uniform load (a/h = 10; exact value = 1.135; multiplier = $10^{-1}pa^2$).

	$N=13$			$N=25$		
M	$L=2$	$L=3$	$L=4$	$L=2$	$L=3$	$L=4$
1	1.164	1.159	1.157	1.160	1.158	1.158
5	1.143	1.138	1.136	1.138	1.137	1.137
10	1.142	1.137	1.135	1.137	1.136	1.135
15	1.142	1.136	1.135	1.137	1.135	1.135

Table 4. Central bending moment, M_x, for simply-supported orthotropic plate subjected to uniform load (a/h = 100; exact value = 1.155; multiplier = $10^{-1}pa^2$).

	$N=13$			$N=25$		
M	$L=2$	$L=3$	$L=4$	$L=2$	$L=3$	$L=4$
1	1.185	1.178	1.177	1.179	1.178	1.178
5	1.164	1.157	1.156	1.158	1.157	1.157
10	1.163	1.155	1.155	1.157	1.155	1.155
15	1.162	1.155	1.154	1.157	1.155	1.155

We now consider the anisotropic case, and the results for this case are given in Tables 5 to 8. An exact solution is not available for this case, and a finite element solution [15] is used as the reference for comparisons.

Table 5. Central displacement, w, for simply-supported anisotropic thick plate subjected to uniform load (a/h = 10 reference value = 1.615; multiplier = $10^{-2}pa^4/E_y/h^3$).

	$N=13$			$N=25$		
M	$L=2$	$L=3$	$L=4$	$L=2$	$L=3$	$L=4$
1	1.347	1.345	1.345	1.346	1.345	1.345
5	1.589	1.593	1.595	1.597	1.599	1.600
10	1.595	1.599	1.602	1.604	1.607	1.608
15	1.596	1.600	1.603	1.605	1.608	1.609

Table 6. Central displacement, w, for simply-supported anisotropic plate subjected to uniform load (a/h = 100; reference value = 1.343; multiplier = $10^{-2}pa^4/E_y/h^3$).

	$N = 13$			$N = 25$		
M	$L = 2$	$L = 3$	$L = 4$	$L = 2$	$L = 3$	$L = 4$
1	0.976	0.975	0.975	0.975	0.975	0.975
5	1.279	1.282	1.283	1.283	1.284	1.284
10	1.308	1.313	1.315	1.316	1.318	1.319
15	1.314	1.319	1.322	1.323	1.326	1.327

Table 7. Central bending moment, M_x, for simply-supported anisotropic plate subjected to uniform load (a/h = 10; reference value = 7.209; multiplier = $10^{-1}pa^2$).

	$N = 13$			$N = 25$		
M	$L = 2$	$L = 3$	$L = 4$	$L = 2$	$L = 3$	$L = 4$
1	6.062	6.679	6.675	6.051	6.679	6.680
5	6.735	7.092	7.131	6.749	7.125	7.134
10	6.917	7.114	7.156	6.948	7.148	7.158
15	6.976	7.134	7.150	7.021	7.178	7.189

Table 8. Central bending moment, M_x, for simply-supported anisotropic plate subjected to uniform load (a/h = 100; reference value = 7.080; multiplier = $10^{-1}pa^2$).

	$N = 13$			$N = 25$		
M	$L = 2$	$L = 3$	$L = 4$	$L = 2$	$L = 3$	$L = 4$
1	6.062	6.043	6.033	6.051	6.046	6.046
5	6.735	6.743	6.749	6.749	6.749	6.755
10	6.917	6.929	6.953	6.948	6.951	6.960
15	6.976	6.972	6.978	7.021	7.024	7.032

Clamped anisotropic plate

We now consider a clamped anisotropic plate under a uniform load. The results for the central displacement for a thick plate ($a/h = 10$) and a thin plate ($a/h = 100$) are given in Tables 9 and 10, and they are compared to the results from [15]. The convergence is again rapid, and the trends for the different strip-elements are similar to the simply-supported case.

Table 9. Central displacement, w, for clamped anisotropic plate subjected to uniform load (a/h = 10; reference value = 7.037; multiplier = $10^{-3}pa^4/E_y/h^3$).

	$N = 13$			$N = 25$		
M	$L = 2$	$L = 3$	$L = 4$	$L = 2$	$L = 3$	$L = 4$
1	6.434	6.392	6.389	6.400	6.390	6.390
5	7.075	7.029	7.024	7.038	7.026	7.026
10	7.083	7.038	7.033	7.046	7.035	7.034
15	7.085	7.039	7.034	7.048	7.036	7.036

Table 10. Central displacement, w, for clamped anisotropic plate subjected to uniform load (a/h = 100; reference value = 4.080; multiplier = $10^{-3}pa^4/E_y/h^3$).

	$N = 13$			$N = 25$		
M	$L = 2$	$L = 3$	$L = 4$	$L = 2$	$L = 3$	$L = 4$
1	3.512	3.492	3.490	3.496	3.491	3.491
5	3.868	3.840	3.836	3.844	3.837	3.837
10	4.036	4.010	4.006	4.014	4.007	4.007
15	4.070	4.045	4.040	4.048	4.041	4.041

Two-span anisotropic plate

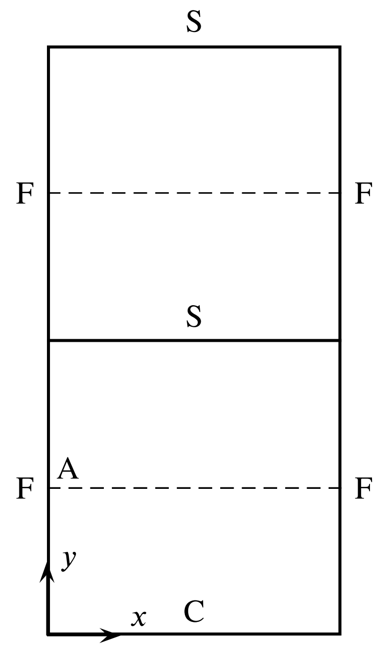

Figure 5. Two-span plate of size $a \times 2a$ with typical subdivision (N = 5).

We now consider the analysis of the two-span anisotropic plate shown in Fig. 5. Both spans are subjected to a uniform load p. The results for the displacement at point A, which is at the centre of the left-hand edge of the lower span, for a thick plate (a/h = 10) and a thin plate (a/h = 100) are given in Tables 11 and 12, and they are compared to the results from [15].

Table 11. Central displacement, w, at point A for two-span anisotropic plate subjected to uniform load (a/h = 10; reference value = 1.772; multiplier = $10^{-2}pa^4/E_y/h^3$).

	$N = 13$			$N = 25$		
M	$L = 2$	$L = 3$	$L = 4$	$L = 2$	$L = 3$	$L = 4$
1	1.341	1.590	1.645	1.567	1.643	1.645
5	1.448	1.712	1.763	1.678	1.757	1.758
10	1.452	1.718	1.770	1.682	1.761	1.761
15	1.453	1.718	1.770	1.681	1.760	1.761

Table 12. Displacement, w, at point A for two-span anisotropic plate subjected to uniform load (a/h = 100; reference value = 1.143; multiplier = $10^{-2}pa^4/E_y/h^3$).

	$N = 13$			$N = 25$		
M	$L = 2$	$L = 3$	$L = 4$	$L = 2$	$L = 3$	$L = 4$
1	0.699	0.926	0.965	0.898	0.965	0.966
5	0.812	1.054	1.088	1.029	1.101	1.102
10	0.829	1.076	1.112	1.051	1.123	1.124
15	0.835	1.083	1.120	1.057	1.130	1.131

The convergence is again rapid, and the trends for the different strip-elements are similar to the previous examples. The results also confirm that the method correctly treats the free edge condition.

Natural frequencies of two-span anisotropic plate

We now calculate the first natural frequency of the two-span plate. The results are given in terms of a frequency parameter

$$\lambda = \frac{a^2\Omega}{t}\sqrt{\frac{\rho}{E_y}} \tag{17}$$

Tables 13 and 14 give the results for both thick and thin plates, and the results are compared with the reference values from [15]. Once again, convergence is rapid for all strip-elements.

Table 13. First natural frequency parameter, $10\lambda_1$, for two-span anisotropic plate (a/h = 10; reference value = 3.523).

	$N = 13$			$N = 25$		
M	$L = 2$	$L = 3$	$L = 4$	$L = 2$	$L = 3$	$L = 4$
1	3.748	3.595	3.583	3.621	3.582	3.581
5	3.701	3.546	3.533	3.572	3.531	3.530
10	3.696	3.541	3.528	3.567	3.526	3.525
15	3.696	3.541	3.528	3.566	3.526	3.525

Table 14. First natural frequency parameter, $100\lambda_1$, for two-span anisotropic plate (a/h = 100; reference value = 3.737).

	$N = 13$			$N = 25$		
M	$L = 2$	$L = 3$	$L = 4$	$L = 2$	$L = 3$	$L = 4$
1	4.025	3.852	3.839	3.883	3.838	3.837
5	3.970	3.794	3.780	3.824	3.779	3.777
10	3.948	3.772	3.757	3.801	3.755	3.753
15	3.942	3.765	3.751	3.794	3.748	3.746

Natural frequencies of L-shaped anisotropic plate

Fig. 6 shows an L-shaped plate made from three parts of size $a \times a$ with each part having thickness h. The lower and left-hand edges are clamped while the other edges are free. As a final example, we calculate the first two natural frequencies of the plate. The analysis used 20 and 38 nodal lines to compare the different strip-elements for this example.

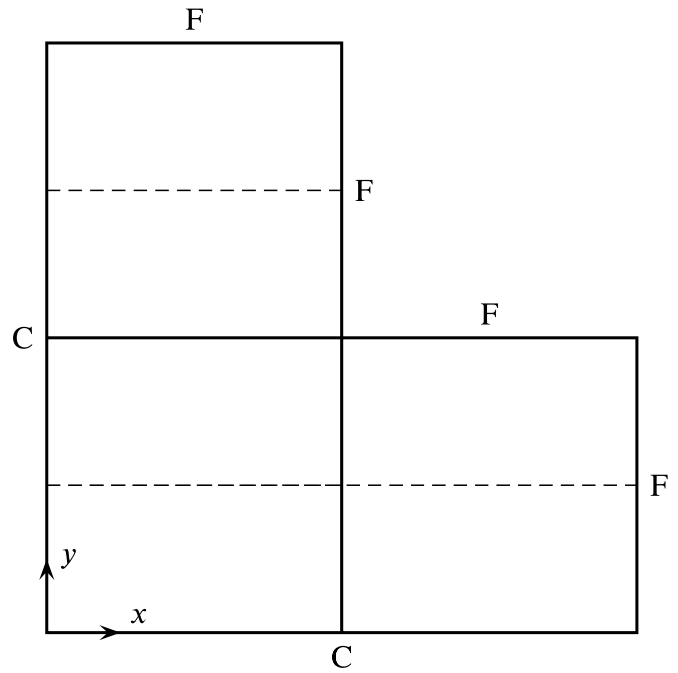

Figure 6. L-shaped plate with three parts of size $a \times a$ and typical subdivision (N = 8).

Tables 15 to 18 give the results for both thick and thin plates, and the results are compared with the reference values from [15]. All strip-elements provide accurate results for both frequencies with few variables. The linear strip-element is less accurate than the quadratic and cubic strip-elements, particularly for the second frequency.

Table 15. First natural frequency parameter, $10\lambda_1$, for L-shaped anisotropic plate (a/h = 10; reference value = 2.032).

	$N = 20$			$N = 38$		
M	$L = 2$	$L = 3$	$L = 4$	$L = 2$	$L = 3$	$L = 4$
1	2.095	2.082	2.081	2.084	2.081	2.081
5	2.048	2.036	2.035	2.038	2.035	2.035
10	2.046	2.034	2.033	2.036	2.033	2.033
15	2.046	2.034	2.033	2.036	2.032	2.032

Table 16. First natural frequency parameter, $100\lambda_1$, for L-shaped anisotropic plate (a/h = 100; reference value = 2.123).

	$N = 20$			$N = 38$		
M	$L = 2$	$L = 3$	$L = 4$	$L = 2$	$L = 3$	$L = 4$
1	2.279	2.263	2.261	2.264	2.260	2.260
5	2.164	2.151	2.149	2.152	2.148	2.148
10	2.147	2.134	2.133	2.135	2.132	2.131
15	2.144	2.131	2.130	2.132	2.128	2.128

Table 17. Second natural frequency parameter, $10\lambda_2$, for L-shaped anisotropic plate (a/h = 10; reference value = 3.148).

	$N = 20$			$N = 38$		
M	$L = 2$	$L = 3$	$L = 4$	$L = 2$	$L = 3$	$L = 4$
1	3.788	3.763	3.761	3.767	3.761	3.761
5	3.189	3.168	3.167	3.172	3.166	3.166
10	3.174	3.153	3.151	3.156	3.151	3.150
15	3.173	3.152	3.150	3.155	3.149	3.149

Table 18. Second natural frequency parameter, $100\lambda_2$, for L-shaped anisotropic plate (a/h = 100; reference value = 3.364).

	$N = 20$			$N = 38$		
M	$L = 2$	$L = 3$	$L = 4$	$L = 2$	$L = 3$	$L = 4$
1	5.081	5.028	5.024	5.036	5.022	5.022
5	3.599	3.571	3.569	3.573	3.565	3.565
10	3.461	3.434	3.432	3.436	3.429	3.429
15	3.431	3.405	3.402	3.407	3.399	3.399

Fig. 7 shows the first two mode shapes for the plate. The lack of symmetry and anti-symmetry of the mode shapes relative to the diagonal of the plate is due to the anisotropic properties. The plots provide a visual confirmation that the second mode is associated with a more oscillatory mode shape than the first mode shape. This confirms the decreasing accuracy of the calculated frequencies with the second mode, which is typical of finite element methods [2].

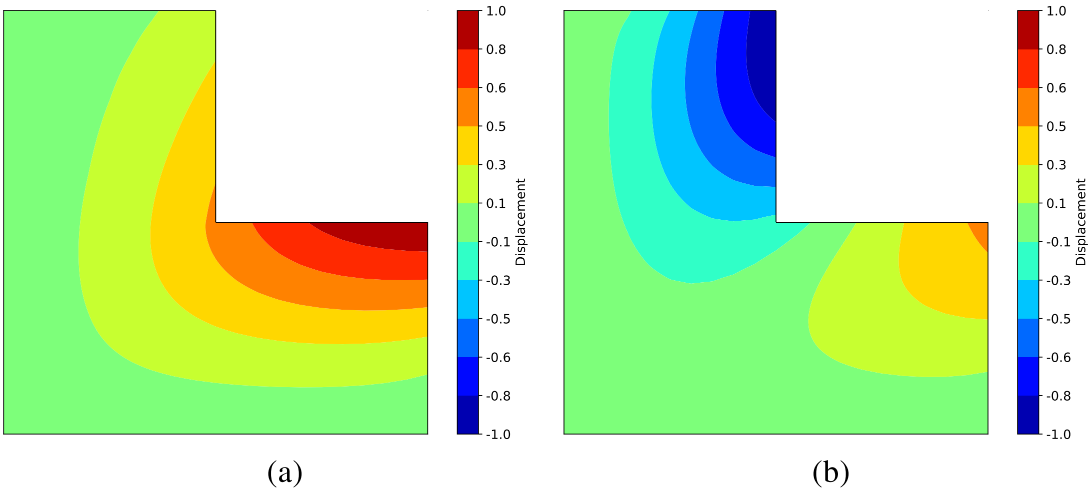

Figure 7. Displacement mode shapes for L-shaped plate, (a) first mode, (b) second mode (a/h = 10; L = 4, M = 15).

Conclusions

This paper has presented a finite strip-element method for the static and vibration analysis of anisotropic, multi-span, thick and thin plate structures. A combination of polynomial and trigonometric functions is used for the strip-element interpolation. The method ensures that all boundary conditions are correctly treated in the usual manner of the finite element method. A reduced integration technique is used to avoid shear locking in the thin plate limit. The formulation of the strip-element equations follows standard finite element procedures and all terms in the element matrices are evaluated analytically. Engineering accuracy is obtained with the generation and solution of few equations.

References

[1] Cheung, Y. and Tham, L. (1998) *Finite Strip Method*, CRC Press, Boca Raton.
[2] Zienkiewicz, O., Taylor, R. and Fox, D. (2014) *The Finite Element Method for Solid and Structural Mechanics*, vol. 2, seventh edn., Butterworth-Heinemann, Oxford.
[3] Petrolito, J. and Golley, B. (2007) Buckling of curved thick plates using finite strip-elements, in *Proceedings, 5th International Conference on Advances in Steel Structures*, vol. 3, pages 511–516, Singapore.
[4] Ovesy, H., Totounferoush, A. and Ghannadpour, S. (2015) Dynamic buckling analysis of delaminated composite plates using semi-analytical finite strip method, *Journal of Sound and Vibration*, **343**, 131–143.
[5] Amoushahi, H. and Goodarzian, F. (2018) Dynamic and buckling analysis of composite laminated plates with and without strip delamination under hygrothermal effects using finite strip method, *Thin-Walled Structures*, **131**, 88–101.
[6] He, B., Liu, D., Long, J., Ma, L. and Ma, P. (2019) A high order finite strip transfer matrix method for buckling analysis of single-branched cross-section thin-walled members, *Thin-Walled Structures*, **135**, 1–11.
[7] Naderian, H., Cheung, M., Mohammadian, M. and Dragomirescu, E. (2019) Integrated finite strip flutter analysis of bridges, *Computers and Structures*, **212**, 145–161.
[8] Daraei, M. and Hamzehei-Javaran, S. (2022) Finite strip method based on Carrera unified formulation for the free vibration analysis of variable stiffness composite laminates, *International Journal for Numerical Methods in Engineering*, **123**.
[9] Mojtabaei, S., Becque, J., Hajirasouliha, I. and Khandan, R. (2023) Predicting the buckling behaviour of thin-walled structural elements using machine learning methods, *Thin-Walled Structures*, **184**.
[10] Gao, W., Chen, L., Ziemian, R. and Liu, S. (2025) Improved shell-finite strip method for inelastic buckling analysis of thin-walled steel members with residual stresses, *Thin-Walled Structures*, **211**.
[11] Petrolito, J. and Golley, B. (2002) Vibration of curved thick plates using finite strip-elements, in *Proceedings,*

2nd International Conference on Structural Stability and Dynamics, pages 266–271, Singapore.

[12] Petrolito, J. and Golley, B. (2006) Buckling of thick plates using finite strip-elements, in *Proceedings, 19th Australasian Conference on the Mechanics of Structures and Materials*, pages 209–214, Christchurch.

[13] Reddy, J. (2007) *Theory and Analysis of Elastic Plates and Shells*, second edn., Taylor and Francis, Philadelphia.

[14] Zienkiewicz, O. and Taylor, R. (2005) *The Finite Element Method for Solid and Structural Mechanics*, vol. 2, sixth edn., Butterworth-Heinemann, Oxford.

[15] Taylor, R. (2026) *FEAP - A Finite Element Analysis Program*, University of California at Berkeley, Berkeley.

Shape Optimization for Minimizing Integrated Dynamic Compliance of Structures with Local Kelvin–Voigt Viscoelastic Dampers under Broadband Excitation

†*Zhiqiang Wu[1], Yuto Isobe[1] and Yuta Nakagawa[1]

[1]Department of Mechanical Systems Engineering, The University of Shiga Prefecture, Japan.

*Presenting author: wu.z@mech.usp.ac.jp
†Corresponding author: wu.z@mech.usp.ac.jp

Abstract

Local viscoelastic dampers provide both stiffness and energy-dissipation effects and are effective for vibration reduction. However, shape optimization of structures containing such dampers under broadband excitation requires repeated frequency-response and sensitivity analyses over many sampling frequencies, resulting in a high computational cost. This study presents a non-parametric shape optimization method for minimizing the integrated dynamic compliance of structures with local Kelvin–Voigt viscoelastic dampers. The dampers are modeled as linear springs and viscous dashpots connected in parallel. To efficiently evaluate the frequency response, a modal superposition approach is employed where real eigenmodes are first obtained for the main structure without the damper contributions. The stiffness and damping effects of the local dampers are then incorporated through small-scale complex equations associated only with the degrees of freedom coupled to the dampers. The objective function is defined as the integral of the dynamic compliance over a prescribed frequency range. Based on this response formulation, the shape gradient function of the objective function is derived using the adjoint variable method. The derived shape gradient function is applied as a distributed boundary load in the H^1 gradient method, which allows for smooth shape updates without explicit shape parameterization. A numerical example of shape optimization is presented for minimizing the integrated dynamic compliance over a prescribed frequency range under a volume constraint.

Keywords: Modal analysis, shape optimization, viscoelastic damper, H^1 gradient method, vibration suppression

Introduction

Vibration reduction is an important requirement in the design of many mechanical and structural systems subjected to dynamic excitation. In addition to modifying the stiffness and mass distributions of the host structure, passive damping devices and viscoelastic damping treatments are widely used to suppress vibration. Structural optimization based directly on frequency-response characteristics has therefore attracted sustained attention. Early studies demonstrated that topology and boundary shape can be optimized with respect to frequency-response characteristics [1]–[3].

For structures containing damping materials or supplemental dampers, the damping treatment itself strongly influences the vibration response and its optimal design. Various studies have considered the optimal distribution of damping materials and constrained-layer damping treatments under harmonic excitation [4]–[7]. In particular, Kang et al. [4] formulated topology optimization for shell structures with damping layers and pointed out that the resulting damping matrix is generally non-proportional. They employed eigenmodes of the undamped system for system reduction and subsequently used complex-mode superposition in state space to evaluate the steady-state response. Zhang and Kang [5] further considered integrated optimization of the host structure and damping layers. Fang and Zheng [6] considered resonant response of plates with constrained-layer damping under harmonic excitation. Takezawa et al. [7] introduced complex dynamic compliance as an objective for topology optimization of damping material in order to reduce resonance response. Integrated frequency-response measures have also been employed in damper-placement problems; Kawamoto et al. [8] employed an integrated transfer-function measure over a prescribed frequency range to determine robust damper locations.

Frequency-response quantities provide a direct measure of vibration under prescribed excitation. When a broadband frequency range is considered, however, the frequency response must be evaluated at many sampling frequencies in every optimization iteration, and the associated sensitivity analyses further increase the computational cost. Model-reduction techniques are therefore particularly attractive for dynamic optimization. Yoon [3] investigated several reduction schemes, including mode superposition and Ritz-vector-based approaches, for frequency-response topology optimization. For proportionally damped structures, real modal coordinates can be used effectively. In earlier work on non-parametric shape optimization of continua with proportional viscous damping, Wu et al. [2] formulated the minimization of frequency-response quantities, including strain energy, kinetic energy, and the absolute value of mean compliance, and evaluated the adjoint variables using modal parameters. However, localized viscous or viscoelastic dampers generally introduce non-proportional damping, for which the conventional complete decoupling based on real modes is not directly available [4].

In the present study, a non-parametric shape optimization method is considered for a structure equipped with local Kelvin–Voigt viscoelastic dampers under broadband harmonic excitation. The objective function is defined as the dynamic compliance integrated over a prescribed frequency range. To retain the computational advantage of a real modal basis while accounting for localized stiffness and damping effects, real eigenmodes are first obtained for the main structure without the damper contributions, and the effects of the local dampers are incorporated through small-scale complex equations associated only with the damper-coupled degrees of freedom. Based on this response formulation, the shape gradient is derived using the adjoint variable method and applied to the H^1 gradient method to obtain smooth non-parametric shape variations under a volume constraint. A numerical example is presented to demonstrate the applicability of the proposed formulation.

Frequency response problems with viscoelastic dampers

Consider a linear elastic structure equipped with *N* local Kelvin-Voigt viscoelastic dampers. Each damper is modeled as a linear spring and a viscous dashpot connected in parallel. The i-th damper consists of a viscous damper with coefficient c_{d_i} and a spring with stiffness k_{d_i}. One end of each damper is connected to the structural degree of freedom d_i, while the other end is fixed to the foundation. Therefore, the deformation of the i-th damper is directly given by the displacement at the structural degree of freedom d_i. The equation of motion of the structure is written as

$$\mathbf{M}\ddot{\boldsymbol{u}}(t) + \mathbf{C}\dot{\boldsymbol{u}}(t) + \mathbf{K}\boldsymbol{u}(t) = \boldsymbol{p}(t), \tag{1}$$

where the stiffness and damping matrices are decomposed as

$$\mathbf{K} = \mathbf{K}_0 + \mathbf{K}_1, \qquad \mathbf{C} = \mathbf{C}_L + \mathbf{C}_D, \tag{2}$$

with

$$\mathbf{C}_L = \alpha\mathbf{M} + \beta\mathbf{K}_0. \tag{3}$$

Here, $\mathbf{K}_0$ is the stiffness matrix of the structure excluding the springs of the Voigt dampers, $\mathbf{K}_1$ is the additional stiffness matrix produced by the damper springs, $\mathbf{C}_L$ is the Rayleigh damping matrix of the structure, and $\mathbf{C}_D$ is the damping matrix produced by the viscous dampers. α, β are the coefficients of Rayleigh damping. For the present configuration, $\mathbf{K}_1$ and $\mathbf{C}_D$ have nonzero components only at the damper-related degrees of freedom $d_1, \dots, d_N$; their corresponding diagonal components are k_{d_i} and c_{d_i}, respectively.

For a harmonic excitation, the force and displacement are expressed as

$$\boldsymbol{p}(t) = \boldsymbol{P}e^{\mathrm{j}\omega t}, \qquad \boldsymbol{u}(t) = \tilde{\boldsymbol{u}}e^{\mathrm{j}\omega t}. \tag{4}$$

Substitution into Eq. (1) gives the frequency-domain equation

$$(-\omega^2\mathbf{M} + \mathrm{j}\omega\mathbf{C} + \mathbf{K})\tilde{\boldsymbol{u}} = \boldsymbol{P}. \tag{5}$$

In the present method, the stiffness and damping contributions of the Voigt dampers are not included in the eigenvalue analysis. The real eigenmodes are obtained using $\mathbf{M}$ and $\mathbf{K}_0$ $as\ follows.$

$$(\mathbf{K}_0 - \lambda^r\mathbf{M})\boldsymbol{\phi}^r = 0, \tag{6}$$

where $\boldsymbol{\phi}^r$ and λ^r are the r-th real eigenmode and eigenvalue, respectively, and n is the number of retained modes. The eigenmodes are mass-normalized so that the generalized mass of each mode is unity.

The displacement amplitude is then expressed by modal superposition as

$$\tilde{\boldsymbol{u}} = \sum_{r=1}^{n} \xi^r\, \boldsymbol{\phi}^r = \boldsymbol{\Phi}\boldsymbol{\xi}, \tag{7}$$

Because $\mathbf{C}_D$ and $\mathbf{K}_1$ are localized at the damper-related degrees of freedom, their contributions are separated from the diagonalized modal terms. For the r-th mode, the modal coordinate is written as

$$\xi^r = \frac{(\boldsymbol{\phi}^r)^T\boldsymbol{P} - \sum_{i=1}^{N}\left(\mathrm{j}\omega c_{d_i} + k_{d_i}\right)\phi^r_{d_i}\tilde{u}_{d_i}}{-\omega^2 + j\alpha\omega + (1 + j\omega\beta)\lambda^r}, \quad r = 1, \dots, n. \tag{8}$$

Here, $\tilde{u}_{d_i}$ denotes the displacement amplitude at the structural degree of freedom to which the i-th damper is attached. Equation (8) shows that, once the N damper-related displacements $\tilde{u}_{d_i}$ are known, all modal coordinates can be calculated directly.

The displacement at a damper-related degree of freedom d_j is obtained from the modal superposition as

$$\tilde{u}_{d_j} = \sum_{r=1}^{n} \xi^r\, \phi^r_{d_j}, \quad j = 1, \dots, N. \tag{9}$$

Substituting Eq. (8) into Eq. (9) and rearranging gives N simultaneous complex equations for the damper-related displacements:

$$\sum_{i=1}^{N}\left(\delta_{ji} + A_{ji}\right)\tilde{u}_{d_i} = B_j, \quad j = 1, \dots, N, \tag{10}$$

where

$$A_{ji} = \sum_{r=1}^{n} \frac{\phi_{d_j}^r \phi_{d_i}^r \left(\mathrm{j}\omega c_{d_i} + k_{d_i}\right)}{-\omega^2 + \mathrm{j}\alpha\omega + (1 + \mathrm{j}\omega\beta)\lambda^r}, \tag{11}$$

and

$$B_j = \sum_{r=1}^{n} \frac{(\boldsymbol{\phi}^r)^T \boldsymbol{P}\, \phi_{d_j}^r}{-\omega^2 + \mathrm{j}\alpha\omega + (1 + \mathrm{j}\omega\beta)\lambda^r}. \tag{12}$$

Here, δ_{ji} is the Kronecker delta. In matrix form, Eq. (10) can be written as

$$(\mathbf{I} + \mathbf{A})\tilde{\boldsymbol{u}}_d = \mathbf{B}, \tag{13}$$

where

$$\tilde{\boldsymbol{u}}_d = [\tilde{u}_{d_1} \quad \tilde{u}_{d_2} \quad \cdots \quad \tilde{u}_{d_N}]^T. \tag{14}$$

For each excitation frequency, Eq. (13) is solved first. The size of this complex system is N, i.e., it is determined by the number of dampers rather than by the total number of structural degrees of freedom. After obtaining $\tilde{\boldsymbol{u}}_d$, the modal coordinates ξ^r are calculated from Eq. (8), and the full displacement amplitude $\tilde{\boldsymbol{u}}$ is reconstructed from Eq. (7). Thus, the response calculation proceeds as

$$\tilde{\boldsymbol{u}}_d \;\rightarrow\; \boldsymbol{\xi} \;\rightarrow\; \tilde{\boldsymbol{u}}. \tag{15}$$

Since the number of dampers is generally much smaller than the total number of degrees of freedom, only a small complex system needs to be solved at each excitation frequency.

Shape Optimization Formulation

The shape gradient used in this study is derived in a continuous setting. The finite element matrix equations introduced in Section 2 are used only for the numerical evaluation of the state and adjoint fields. Let $\Omega \subset \mathbb{R}^d, d = 2{,}3$ denote the domain occupied by the main elastic structure. The boundary $\Gamma = \partial\Omega$ is divided into the fixed boundary Γ_1, the loaded boundary Γ_2, and the design boundary Γ_s.

Continuous frequency-response problem and objective function

The governing equation is expressed in the following variational form:

$$a(\tilde{\boldsymbol{u}}, \boldsymbol{v}) + j\omega c(\tilde{\boldsymbol{u}}, \boldsymbol{v}) - \omega^2 b(\tilde{\boldsymbol{u}}, \boldsymbol{v}) = l(\boldsymbol{P}, \boldsymbol{v}), \quad \forall \boldsymbol{v} \in U, \tag{16}$$

where $\boldsymbol{v}$ is an arbitrary variation in *U*. Bilinear forms of $a(\cdot\,,\ \cdot)$, $b(\cdot\,,\ \cdot)$, $c(\cdot\,,\ \cdot)$ and $l(\cdot\,,\ \cdot)$ are defined as Eqs. (17)-(20), and the admissible functional space *U* is defined as $U \equiv \{\boldsymbol{v} \in H^1(\Omega)\}$. Here $H^m(\Omega)$ denotes the Sobolev space of functions whose derivatives up to order *m* are square integrable.

$$\begin{aligned} a(\tilde{\boldsymbol{u}}, \boldsymbol{v}) &= a_0(\tilde{\boldsymbol{u}}, \boldsymbol{v}) + a_1(\tilde{\boldsymbol{u}}, \boldsymbol{v}) \\ &= \int_\Omega C_{ijkl} \tilde{u}_{k,l} v_{i,j} dx + \sum_{m=1}^{N} \int_\Omega k_{dm} \delta(x - x_{dm}) \tilde{u}_i v_i dx \end{aligned} \tag{17}$$

$$b(\tilde{\boldsymbol{u}}, \boldsymbol{v}) = \int_\Omega \rho \tilde{u}_i v_i dx \tag{18}$$

$$c(\tilde{\boldsymbol{u}}, \boldsymbol{v}) = \beta a_0(\tilde{\boldsymbol{u}}, \boldsymbol{v}) + \alpha b(\tilde{\boldsymbol{u}}, \boldsymbol{v}) + \sum_{m=1}^{N} \int_\Omega c_{dm} \delta(x - x_{dm}) \tilde{u}_i v_i dx \tag{19}$$

$$l(\boldsymbol{P},\boldsymbol{v}) = \int_{\Gamma_2} P_i v_i d\Gamma\,, \tag{20}$$

where C_{ijkl} represents the elastic stiffness tensor, N is the number of dampers, and $\delta(\cdot)$ denotes the Dirac's delta function. x_{dm} is the position of dm degree of freedom. The Einstein summation convention and partial differential notation $(\cdot)_{,i} \equiv \partial(\cdot)/\partial x_i$ are used for convenience.

In the following derivation, a conjugate equation of the governing equation (Eq. 16), which governs $\tilde{\boldsymbol{u}}^*$, the conjugate complex of $\tilde{\boldsymbol{u}}$, is also introduced.

$$a(\tilde{\boldsymbol{u}}^*,\boldsymbol{v}^*) - j\omega c(\tilde{\boldsymbol{u}}^*,\boldsymbol{v}^*) - \omega^2 b(\tilde{\boldsymbol{u}}^*,\boldsymbol{v}^*) = l(\boldsymbol{P},\boldsymbol{v}^*)\,,\ \ \forall \boldsymbol{v}^* \in U. \tag{21}$$

For a prescribed excitation frequency ω, the dynamic-compliance measure is defined by

$$F(\omega) = l(\boldsymbol{P},\tilde{\boldsymbol{u}})l(\boldsymbol{P},\tilde{\boldsymbol{u}}^*) \tag{22}$$

and the objective function for broadband excitation is

$$J = \int_{\omega_1}^{\omega_2} F\,(\omega)\,d\omega \tag{23}$$

The structural volume is constrained by

$$V(\Omega) = \int_{\Omega} d\,\Omega \leq \overline{V} \tag{24}$$

Thus, the optimization problem is to determine a domain variation that minimizes Eq. (23) while satisfying the frequency-response equations (Eq. 16, Eq. 21) and the prescribed volume constraint.

Lagrange functional and Adjoint equations

For convenience, define the residual forms

$$\mathcal{R}_\omega(\tilde{\boldsymbol{u}},\boldsymbol{v}) = a(\tilde{\boldsymbol{u}},\boldsymbol{v}) + j\omega c(\tilde{\boldsymbol{u}},\boldsymbol{v}) - \omega^2 b(\tilde{\boldsymbol{u}},\boldsymbol{v}) - l(\boldsymbol{P},\boldsymbol{v}), \tag{25}$$

$$\mathcal{R}^*_\omega(\tilde{\boldsymbol{u}}^*,\boldsymbol{v}^*) = a(\tilde{\boldsymbol{u}}^*,\boldsymbol{v}^*) - j\omega c(\tilde{\boldsymbol{u}}^*,\boldsymbol{v}^*) - \omega^2 b(\tilde{\boldsymbol{u}}^*,\boldsymbol{v}^*) - l(\boldsymbol{P},\boldsymbol{v}^*). \tag{26}$$

Treating the complex response and its conjugate as formally independent variables, the Lagrange functional is written as

$$L = \int_{\omega_1}^{\omega_2} [F(\omega) - \mathcal{R}_\omega(\tilde{\boldsymbol{u}},\boldsymbol{v}) - \mathcal{R}^*_\omega(\tilde{\boldsymbol{u}}^*,\boldsymbol{v}^*)]\,d\omega + \Lambda\big[V(\Omega) - \overline{V}\big], \tag{27}$$

where Λ is the Lagrange multiplier associated with the volume constraint, and $\boldsymbol{v}$ is regarded as the adjoint variable in the Lagrange functional. By imposing stationarity of L with respect to variations of $\tilde{\boldsymbol{u}}$ and $\tilde{\boldsymbol{u}}^*$, the adjoint equations are obtained as

$$a(\tilde{\boldsymbol{u}}',\boldsymbol{v}) + j\omega c(\tilde{\boldsymbol{u}}',\boldsymbol{v}) - \omega^2 b(\tilde{\boldsymbol{u}}',\boldsymbol{v}) = l(\boldsymbol{P},\tilde{\boldsymbol{u}}')l(\boldsymbol{P},\tilde{\boldsymbol{u}}^*), \quad \forall \tilde{\boldsymbol{u}}' \in U, \tag{28}$$

and

$$a(\tilde{\boldsymbol{u}}^{*\prime},\boldsymbol{v}^*) - j\omega c(\tilde{\boldsymbol{u}}^{*\prime},\boldsymbol{v}^*) - \omega^2 b(\tilde{\boldsymbol{u}}^{*\prime},\boldsymbol{v}^*) = l(\boldsymbol{P},\tilde{\boldsymbol{u}})\,l(\boldsymbol{P},\tilde{\boldsymbol{u}}^{*\prime}), \quad \forall \tilde{\boldsymbol{u}}^{*\prime} \in U. \tag{29}$$

The left-hand side of Eq. (28) has the same operator as the state equation (16). Therefore, after finite element discretization, the adjoint response can be evaluated using the same reduced modal formulation as that used for the displacement response in Section 2; only the right-hand side is changed.

Shape gradient function

The domain variation is represented by a sufficiently smooth velocity field $\boldsymbol{V}(\boldsymbol{x})$ [9]. The normal velocity of the design boundary is $V_n = \boldsymbol{V} \cdot \boldsymbol{n}$, where $\boldsymbol{n}$ is the outward unit normal vector. Applying the material derivative method [10] to Eq. (27), and using the state and adjoint equations to eliminate the material derivatives of the state and adjoint fields, the derivative of the Lagrange functional can be expressed in the boundary form

$$\dot{L} = \int_{\Gamma_s} G\ V_n\, d\Gamma. \tag{30}$$

Under the assumption that the shape variations of the damper attachment points and the load application region are not considered, the shape gradient function is written as

$$G = \int_{\omega_1}^{\omega_2} G_\omega\ d\omega + \Lambda, \tag{31}$$

with

$$G_\omega = -2\mathrm{Re}\big[(1 + j\omega\beta)C_{ijkl}\tilde{u}_{k,l}v_{i,j} - (\omega^2 - j\omega\alpha)\rho\tilde{u}_i v_i\big], \tag{32}$$

where Re[·] denotes the real part. Equation (32) is a continuous shape-gradient density defined on the design boundary. Although the local damper terms do not appear explicitly in Eq. (32), their effects are included through the state and adjoint fields.

Shape optimization system by using the H^1 gradient method

The derived shape gradient is used as a distributed boundary load in the H^1 gradient method [11][12].

Let $a_G(\boldsymbol{V}, \boldsymbol{W})$ denote a coercive bilinear form corresponding to a fictitious linear elastic problem for shape modification. The shape velocity field is obtained from

$$a_G(\boldsymbol{V}, \boldsymbol{W}) = -\int_{\Gamma_s} G\ \boldsymbol{W} \cdot \boldsymbol{n}\, d\Gamma, \quad \forall \boldsymbol{W} \in D, \tag{33}$$

where D denotes the admissible space for the shape variation. The design boundary is then updated in the direction of $\boldsymbol{V}$. Because the shape variation is obtained through an elastic smoothing problem, smooth boundary modifications can be generated without introducing explicit geometric shape parameters.

The shape optimization system integrates the H^1 gradient method, the FEM software HyperWorks, and an in-house developed program. In each optimization iteration, the state and adjoint responses are evaluated over the prescribed frequency range, the integrated shape gradient in Eq. (31) is calculated, and the shape is updated using Eq. (33). This procedure is repeated until the objective function converges while satisfying the volume constraint.

Numerical analysis

Numerical model

The material properties, dimensions, and frequencies are treated in a non-dimensional form. Figure 1 shows the analysis model, which is a three-dimensional beam-like structure with dimensions of 50 × 5 × 2. The left end is fully fixed, and at the center of the right end is supported by a Kelvin–Voigt viscoelastic damper. An excitation force is applied at the center of the right end in the direction perpendicular to the longitudinal axis. The Young's modulus, density, and Poisson's ratio are $E = 1.0 \times 10^8$, $\rho = 1.0$, and $\nu = 0.3$, respectively. The Rayleigh damping coefficients are $\alpha = 1.0$, $\beta = 1.0 \times 10^{-6}$. The viscous damping coefficient and spring stiffness of the Kelvin–Voigt damper are $c_d = 200$ and $k_d = 80000$, respectively. The first 40 modes are retained in the frequency-response analysis.

Analysis results

Dynamic-compliance minimization was performed over the frequency range from 0.0 to 5.0 with a sampling interval of 0.1. This frequency range is below the first natural frequency of the structure. Figure 2 shows the optimized shape. As shown in the A–A cross-section, the central region becomes thinner, whereas the upper and lower regions become thicker, resulting in an approximately I-shaped cross-section. This shape is effective in increasing the bending stiffness of the structure. Since the target frequency range is below the first natural frequency, the optimized shape shows a tendency similar to that obtained by static compliance minimization. On the other hand, the shape near the right end differs somewhat from a typical shape obtained by static compliance minimization. This difference is considered to reflect the influence of the Kelvin–Voigt damper attached to the right end. The objective function decreases gradually and converges while the structural volume remains nearly constant. The final objective function is reduced to approximately 3% of its initial value.

Figure 1. FE-model and Boundary conditions for frequency-response analysis

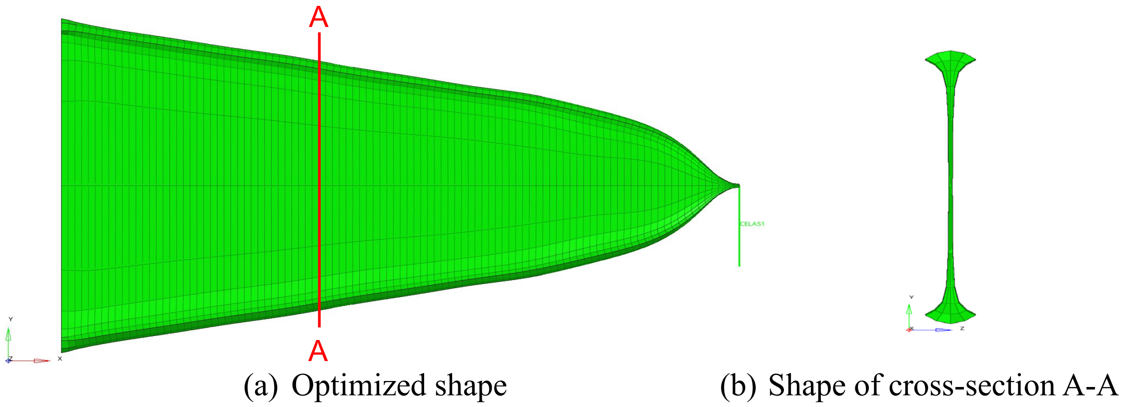

Figure 2. Optimized shape in the frequency range from 0.0 to 5.0

Conclusions

A non-parametric shape optimization method was presented for structures with local Kelvin–Voigt viscoelastic dampers under broadband harmonic excitation. In the frequency-response analysis, real eigenmodes of the main structure without the damper contributions were used, while the stiffness and damping effects of the local dampers were incorporated through small-scale complex equations associated with the damper-related degrees of freedom. The integrated dynamic compliance over a prescribed frequency range was adopted as the objective function, and its shape gradient was derived using the adjoint variable method.

The shape optimization system was established by integrating the H^1 gradient method, the FEM software HyperWorks, and an in-house developed program. In the numerical example, the proposed shape optimization method successfully reduced the integrated dynamic compliance while satisfying the prescribed volume constraint. The results demonstrate the applicability of the proposed method to broadband vibration-reduction design for structures with local viscoelastic dampers.

References

[1] Ma, Z. D., Kikuchi, N. and Hagiwara, I. (1993) Structural topology and shape optimization for a frequency response problem, *Computational Mechanics* **13**, 157–174, https://doi.org/10.1007/BF00370133.

[2] Wu, Z., Sogabe, Y. and Azegami, H. (1998) Domain Optimization Analysis in Frequency Response Problems Considering Proportional Viscous Damping. T*ransactions of the Japan Society of Mechanical Engineers, Series C* **64**, 623, 2618–2624, https://doi.org/10.1299/kikaic.64.2618.

[3] Yoon, G. H. (2010) Structural topology optimization for frequency response problem using model reduction schemes, *Computer Methods in Applied Mechanics and Engineering*, **199** (25–28), 1744–1763, https://doi.org/10.1016/j.cma.2010.02.002.

[4] Kang, Z., Zhang, X., Jiang, S. and Cheng, G. (2012) On topology optimization of damping layer in shell structures under harmonic excitations, *Structural and Multidisciplinary Optimization*, **46** (1), 51–67, https://doi.org/10.1007/s00158-011-0746-4.

[5] Zhang, X. and Kang, Z. (2016) Vibration suppression using integrated topology optimization of host structures and damping layers, *Journal of Vibration and Control*, **22** (1), 60–76, https://doi.org/10.1177/107754631452836.

[6] Fang, Z. and Zheng, L. (2015) Topology optimization for minimizing the resonant response of plates with constrained layer damping treatment, *Shock and Vibration*, **2015**, 1-11, https://doi.org/10.1155/2015/376854.

[7] Takezawa, A., Daifuku, M., Nakano, Y., Nakagawa, K., Yamamoto, T. and Kitamura, M. (2016) Topology optimization of damping material for reducing resonance response based on complex dynamic compliance, *Journal of Sound and Vibration*, **365**, 230–243, https://doi.org/10.1016/j.jsv.2015.11.045.

[8] Kawamoto, T., Fujita, K., Tsuji, K. and Takewaki, I. (2016) Robust optimal placement of dampers in structures with set-back and eccentricity using sensitivity analysis for integrated transfer function, *International Journal of Earthquake and Impact Engineering*, **1** (4), 377–394, https://doi.org/10.1504/IJEIE.2016.083252.

[9] Sokolowski, J., Zol´esio, J.P. (1995) Introduction to Shape Optimization: Shape Sensitivity Analysis, New York: SpringerVerlag

[10] Choi, K. K. and Kim, N. H. (2005) *Structural Sensitivity Analysis and Optimization 2*, (Springer, New York).

[11] Azegami, H. (1994) A Solution to Domain optimization problems, *Transactions of the Japan Society of Mechanical Engineers Series A* **60** (574), 1479-1486 (in Japanese), https://doi.org/10.1299/kikaia.60.1479.

[12] Azegami, H., Wu, Z. (1996) Domain optimization analysis in Linear Elastic Problems (Approach Using Traction Method), *Transactions of the Japan Society of Mechanical Engineers Series A*, *Mechanics and material engineering* **39** (2), 272-278, https://doi.org/10.1299/jsmea1993.39.2_272.

AUTHOR INDEX